Optimization and Demonstration of In Situ Chemical Sensors for Marine Waters

Dissertation

zur Erlangung des akademischen Grades eines

Doktors der Naturwissenschaften

- Dr. rer. nat. -

an der Mathematisch-Naturwissenschaftlichen

Fakultät der Christian-Albrechts-Universität

zu Kiel

vorgelegt von

Münevver Nehir

Kiel, 2022

Erstgutachter: Prof. Dr. Eric P. Achterberg
Zweitgutachter: Prof. Dr. Carsten Frank
Tag der mündlichen Prüfung: 28.06.2022

"We cannot solve problems by using the same kind of thinking we used when we created them."

Albert Einstein

Summary

The importance of autonomous in situ chemical sensors for ocean observations has increased drastically over the last decades. Yet, the huge potentials of sensor-based data collection remain underutilized by the scientific and regulatory communities, despite wider than ever usage of sensors. This thesis is part of a growing body of work to extend the usability of sensors and is embedded in the Ocean Best Practice approach, which could improve data quality in ocean observation in general.

The here presented work focuses on pH and nitrate, both essential ocean variables in the quest of the scientific community to understand the state of ocean acidification and disruptions in marine productivity, which threaten marine ecosystem health. Given the enormous dimensions of the oceans and the challenging conditions for field research, expanding the utilization of autonomous chemical sensors for monitoring those parameters brings structural advancements for the research community. Besides that, sensor-based output of well-resolved data overcomes the issue of undersampling by conventional methods, an issue which was highlighted in the first focus of this thesis. Specifically, it could be mentioned that undersampling is a particularly crucial issue in highly dynamic water systems. Yet, the highly capable LOC pH sensor (ClearWater Sensors, Southampton, UK) had not been tested in highly dynamic coastal and estuarine systems to date. In order to expand its operational limits, the sensor was deployed in such systems. The evaluation of the collected pH and auxiliary data shows the potentials of expanding LOC deployment into highly dynamic marine systems. Not only the usability in low salinity environments was illuminated, also a substantially more comprehensive coverage of rapid events could be achieved, compared to traditional benchtop approaches.

The second focus is the optimization of the data processing procedures and therefore the quality of nitrate data collection through the OPUS sensor (TriOS GmbH, Germany). Following a range of laboratory and field tests, a new algorithm was introduced, which took the specific properties of the OPUS into account.

Summary

It could be shown that through our improved algorithm for the OPUS sensor, the nitrate measurements had an accuracy of better than ca. 2 µM, yielding a significant advancement in line with the overarching goal of improved data quality.

In the third focus, unwanted distortions also referred to as errors of the measured spectrum due to the non-ideal behaviour of compact charge-coupled device (CCD) spectrometers were identified. Although the CCDs are optimal and highly sensitive tools, preferred in a variety of applications such as space, ocean, and telecommunications, they suffer from a range of internal error sources linked to dark currents, stray light, non-linearity etc. Therefore, characterization and correction of errors are essential when accurate spectral measurements are a need. In agreement with such a necessity, we characterized the non-linearity error of a Hamamatsu C10082CA mini-spectrometer experimentally and developed a universally applicable correction algorithm. Results pointed to a significant improvement in signal-to-noise ratio of spectral readings, after the new algorithm was applied. The non-linearity error of a compact spectrometer was reduced from several hundred counts to ca. 40 counts. This provides the attempt of improving output data quality by autonomous sensors in a general sense.

In summary, this Ph.D. thesis provides improvements in the area of autonomous spectrophotometric data collection of essential biogeochemical parameters. The achievements are associated with the acquisition of accurate and temporally well-resolved real-time data. A more reliable sensor-based data collection and improved deployability promotes a broader usage of autonomous sensors in general. Thus, a financially more sustainable ocean monitoring approach can be achieved, since a broader adaptation of autonomous sensors in research yields a higher cost efficiency.

It contributes to the increasing demand for high quality and in situ data of particular ocean areas of concern i.e., ocean acidification and eutrophication. Furthermore, it widens our understanding of crucial biogeochemical processes and physiological conditions of marine waters.

Zusammenfassung

Die Bedeutung autonomer chemischer In situ Sensoren für die Meeresbeobachtung hat in den letzten Jahrzehnten drastisch zugenommen. Dennoch wird das enorme Potenzial der sensorbasierten Datenerfassung von den wissenschaftlichen und behördlichen Gremien noch nicht ausreichend genutzt, obwohl die Sensoren häufiger denn je zum Einsatz kommen. Diese Arbeit ist Teil einer wachsenden Anzahl von Arbeiten zur Erweiterung der Nutzbarkeit von Sensoren und ist eingebettet in den Ocean Best Practice-Ansatz, der die Datenqualität in der Meeresbeobachtung im Allgemeinen verbessern könnte.

Die hier vorgestellte Arbeit konzentriert sich auf pH-Wert und Nitrat, beides wichtige Meeresvariablen, die die wissenschaftliche Gemeinschaft benötigt, um den Zustand der Ozeanversauerung und die Störungen der Meeresproduktivität zu verstehen, die die Gesundheit der marinen Ökosysteme bedrohen. Angesichts der enormen Ausmaße der Ozeane und der schwierigen Bedingungen für die Feldforschung bringt die Ausweitung des Einsatzes autonomer chemischer Sensoren zur Überwachung dieser Parameter strukturelle Fortschritte für die Forschungsgemeinschaft. Darüber hinaus überwindet die sensorgestützte Ausgabe von gut aufgelösten Daten das Problem der Untererfassung durch konventionelle Methoden, ein Problem, das im ersten Schwerpunkt dieser Arbeit hervorgehoben wurde. Insbesondere kann erwähnt werden, dass die Unterabtastung in hochdynamischen Wassersystemen ein besonders wichtiges Problem darstellt. Der hochleistungsfähige LOC-pH-Sensor (ClearWater Sensors, Southampton, UK) wurde jedoch bisher noch nicht in hochdynamischen Küsten- und Ästuarsystemen getestet. Um seine Einsatzgrenzen zu erweitern, wurde der Sensor in solchen Systemen eingesetzt. Die Auswertung der gesammelten pH- und Hilfsdaten zeigt das Potenzial eines erweiterten Einsatzes des LOC in hochdynamischen Meeressystemen. Nicht nur die Verwendbarkeit in Umgebungen mit niedrigem Salzgehalt wurde beleuchtet, sondern es konnte auch eine wesentlich umfassendere Erfassung von schnellen Ereignissen im Vergleich zu traditionellen Benchtop-Ansätzen erreicht werden.

Der zweite Schwerpunkt ist die Optimierung der Datenverarbeitungsverfahren und damit der Qualität der Nitratdatenerfassung durch den OPUS-Sensor (TriOS GmbH, Deutschland). Nach einer Reihe von Labor- und Feldtests wurde ein neuer Algorithmus eingeführt, der die spezifischen Eigenschaften des OPUS berücksichtigt.

Es konnte gezeigt werden, dass durch unseren verbesserten Algorithmus für den OPUS-Sensor die Nitratmessungen eine Genauigkeit von besser als ca. 2 µM aufwiesen, was einen bedeutenden Fortschritt im Einklang mit dem übergeordneten Ziel einer verbesserten Datenqualität darstellt.

Im dritten Schwerpunkt wurden unerwünschte Verzerrungen, auch als Fehler des gemessenen Spektrums bezeichnet, festgestellt, die auf das nicht-ideale Verhalten kompakter CCD-Spektrometer zurückzuführen sind. Obwohl die CCDs optimale und hochempfindliche Instrumente sind, die in einer Vielzahl von Anwendungen wie Raumfahrt, Ozean und Telekommunikation bevorzugt werden, leiden sie unter einer Reihe interner Fehlerquellen, die mit Dunkelströmen, Streulicht, Nichtlinearität usw. zusammenhängen. Daher sind die Charakterisierung und Korrektur von Fehlern unerlässlich, wenn genaue Spektralmessungen erforderlich sind. In Übereinstimmung mit dieser Notwendigkeit haben wir den Nichtlinearitätsfehler eines Hamamatsu C10082CA Mini-Spektrometers experimentell charakterisiert und einen universell anwendbaren Korrekturalgorithmus entwickelt. Die Ergebnisse zeigten eine deutliche Verbesserung des Signal-Rausch-Verhältnisses der Spektralmessungen, nachdem der neue Algorithmus angewendet wurde. Der Nichtlinearitätsfehler eines kompakten Spektrometers konnte von mehreren hundert Zählungen auf ca. 40 Zählungen reduziert werden. Damit wird der Versuch unternommen, die Qualität der Ausgabedaten von autonomen Sensoren im Allgemeinen zu verbessern.

Zusammenfassend lässt sich sagen, dass diese Dissertation Verbesserungen im Bereich der autonomen spektrophotometrischen Datenerfassung wesentlicher biogeochemischer Parameter liefert. Die Errungenschaften stehen im Zusammenhang mit der Erfassung von genauen und zeitlich gut aufgelösten Echtzeitdaten. Eine zuverlässigere sensorgestützte Datenerfassung und eine verbesserte Einsatzfähigkeit fördern eine breitere Nutzung autonomer Sensoren im Allgemeinen.

Auf diese Weise kann ein finanziell nachhaltigeres Meeresüberwachungskonzept erreicht werden, da eine breitere Anwendung autonomer Sensoren in der Forschung zu einer höheren Kosteneffizienz führt. Sie trägt dazu bei, die steigende Nachfrage nach qualitativ hochwertigen In situ Daten zu bestimmten Problembereichen der Ozeane, wie z.B. Ozeanversauerung und Eutrophierung, zu befriedigen. Darüber hinaus erweitert es unser Verständnis der entscheidenden biogeochemischen Prozesse und physiologischen Bedingungen der Meeresgewässer.

Acknowledgement

First and foremost, I want to express my sincere gratitude to my supervisor Prof. Dr. Eric P. Achterberg for his constant support, encouragement, and for giving me the opportunity to work on this exciting topic. I am deeply grateful for all of the opportunities you have given me as a member of your research group to develop both scientifically and personally. Many thanks for inspiring discussions, sending me to various national and international conferences, and for my participation in the M135, MOSES mCAN2018 and Sternfahrt expeditions, which gave me excellent field experiences in utilising various autonomous chemical sensors and sparked my interest for marine science. I am grateful to all the scientists I had the honour of meeting and working with, at the conferences, in the laboratory and on the expeditions.

I will be forever grateful to Prof. Dr. Carsten Frank for his generous support, fruitful discussions and wise advice that improved my thesis. No matter how busy he was, Carsten always found time to discuss my work, help me with whatever I needed. I greatly benefited from his expertise, guidance and feedback. My special thanks goes to Dr. Mario Esposito for his support, insightful comments to assist my work, and tireless commitment during sensor deployments. Thank you very much also for uncountable hours proof reading my texts. I am deeply grateful to Christian Begler for sharing his constant technical support in many phases of the work presented in Chapter 3. Christian's experience and assistance, sometimes during out-of-office hours, will always be appreciated. I would like to express my particular gratitude to Prof. Dr. Oliver Zielinski and Dr. Socratis Loucaides for giving professional advices and supporting part of the experimental tools used to conduct this work.

During this journey, I have made many intelligent, inspiring and amusing friends from all around the world without whom my Ph.D. experience would have been very dull. I would like to thank all members of the AG Achterberg at GEOMAR for their helpfulness and for creating such a collaborative and pleasant working atmosphere, namely Martha Gledhill, Mark Hopwood, Kechen Zhu, Felix Geissler, Evangelia Louropoulou, Pablo Lodeiro, Aaron Beck, Insa Rapp, Thomas Browning, Kathleen Gosnell, Te Liu, Ali Alhashem, Mahmoud Altahan, Andre

Mutzberg, Dominik Jasinski, Boie Bogner, and especially to Maria Martinez-Cabanas, Siao Jean Khoo, Lúcia Vieira, Stephan Krisch and Jan-Lukas Menzel-Barraquetta. I extend my gratitude to Andre Mutzberg for providing the analysis of discrete water samples for nutrients, and Birgit Reiner for all the technical and administrative support I needed during my Ph.D. To you all, I am very grateful.

Thanks also to the Integrated School of Ocean Sciences and the CAU Graduate Centre for additional training through graduate courses, and for providing financial support that made my participation at international conferences possible. Many thanks to GEOMAR Weather Station for supplying the weather dataset. I also acknowledge the GEOMAR scientists for the production of the ancillary data used in this research effort, and the engineers for providing technical support.

This work has been financially supported by the European Union's Horizon 2020 "AtlantOS" project. Additional funding was obtained from the "OCEANSensor" project, supported as part of the MarTERA Program of the German Federal Ministry of Economic Affairs and Energy.

Special thanks goes to my best friend, my husband, Benedikt Pellengahr. I could not have come this far without his kindness, patience, witty spirit and love. Thank you Benedikt, for always believing I could do whatever I set my mind to, even when I did not. Ich bin so glücklich, dass ich dich in meinem Leben habe. Ein ganz besonderes Dankeschön geht an meine Schwiegereltern, Nicole Lemke und Walter Pellengahr, und meinen Schwager Martin Pellengahr für all ihre Beiträge, für die ich ihnen sehr dankbar bin.

Finally, I would like to express my deepest gratitude to my parents, Ebru Nehir and Adnan Nehir, and my brother Anıl Nehir, for everything they added to my life. They always believed in me and stood right my side giving me all the support and encouragement I needed. I came this far because of their hard work, energy and faith in me. I dedicate this thesis to my family, the solid foundation that sustains my life. Canım anneciğim, babacığım ve kardeşim sizi çok seviyorum, iyi ki varsınız, desteğiniz ve her şey için çok teşekkür ederim.

Contents

List of figures

List of tables

1. Introduction

1.1. Background

1.1.1. Autonomous Ocean Observations

The ocean is home to a wide range of ecosystems, including small and large organisms, which provide a source of livelihood for humankind, and have a central role in shaping the world's economy and regulating climate. However, the health of the oceans is under constant threat by anthropogenic activities. Pressures related to climate change, including global warming, unsustainable use of marine resources, deoxygenation, acidification, pollution including eutrophication, and habitat loss are causing detrimental impacts on ocean ecosystem functioning (Doney et al., 2012).

Monitoring the state of the oceans is vital for identifying various environmental problems, including climate change, and using our ocean in a sustainable manner (Visbeck, 2018). Studies focusing on ocean observations help us get a clearer picture of the impact of anthropogenic stressors on the marine environment and project potential future scenarios. Monitoring the GOOS Essential Ocean Variables (EOVs, http://www.goosocean.org/eov), such as temperature, salinity, ocean color, oxygen, nutrients, inorganic and dissolved organic carbon, pH, particulate matter, phytoplankton biomass, and biodiversity, throughout the worlds' oceans have a high research priority. Although extensive and collective studies are essential for ocean monitoring research, the complexity and enormous dimensions of the oceans set a high bar. The exploration and data collection, especially in remote and hostile environments, is labour intensive, expensive and often limited in scope.

The ocean is a suitable environment for the deployment of various sensor and autonomous monitoring systems. **Figure 1.1** shows the dynamic evolution of autonomous ocean monitoring systems, which is ongoing. Each platform has specific purposes and areas of operation (Chai et al., 2020).

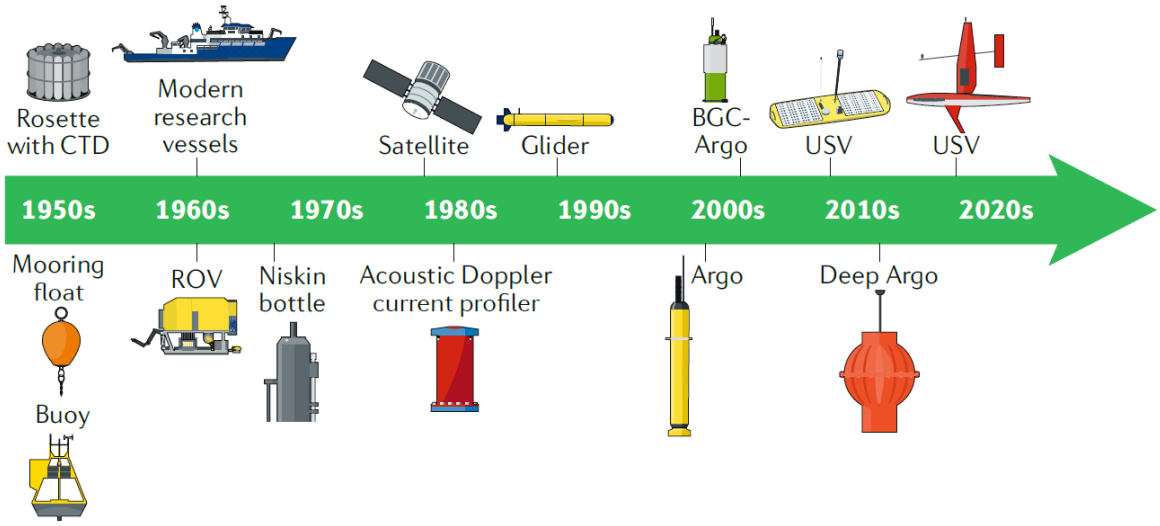

Figure 1.1: Timeline of oceanographic observation platforms used for monitoring marine biogeochemistry (Source: Chai et al., 2020).

A pioneering exercise in ocean observations is believed to be the *Challenger Expedition* between 1873 and 1876 (C. Wyville-Thomson and J. Murray, 1885). Since then, several tens of thousands of ship-based oceanographic studies have taken place, but our knowledge is still rather incomplete. Traditionally, discrete seawater samples for the analysis of specific parameters are collected on ships using Go-Flo or Niskin bottles, or underway water pump systems, and the samples are then preserved until land-based laboratory analysis following best practice guidelines. The conventional methods rely on decades-long applied experience, are broadly tested and precise, and therefore essential for validation of new methods. On the other hand, this traditional approach requires generally long sampling and analysis times, and involves a risk of sample contamination during sample transfer, and also may involve storage issues.

With conventional methods alone, our understanding of the intricate physical (wind-driven/convective/isopycnal-mixing, up-/down-welling, diapycnal diffusion, horizontal advection), chemical (air-sea CO_2 exchange, ocean acidification, deoxygenation), biological (primary production, phytoplankton growth/loss) processes, and biogeochemical cycles in marine waters would stay limited, despite the extensive efforts (Chai et al., 2020).

Recent efforts, such as the Global Ocean Ship-Based Hydrographic Survey (GO-SHIP, https://www.go-ship.org/) and the GEOTRACES Program (https://www.geotraces.org/), improved the global coverage of measurements. However, classical ship-based ocean observations are not sufficient for capturing many of the complex events in real-time, and samplings are limited to the expedition period, mostly in moderate weather, leading to a bias towards the summer season.

An alternative option is to use satellites. Satellites are great remote sensing tools for enabling predictions of long-term trends in ocean ecosystem change at the basin and global scales (Chai et al., 2020). For example, the ocean-color satellite observations in the late 1970s provided the first global view of phytoplankton distribution (Gordon et al., 1980). Unfortunately, satellite ocean-color time series often have data gaps during the winter season due to increased cloudiness. In addition, they only cover the surface ocean, not the entire water column (Gregg and Casey, 2007), and observations are available for a limited numbers of variables only. Therefore high-resolution and real-time biogeochemical data collection tools and methods are required to improve the efficiency and scope of our monitoring efforts beyond the ships and satellites. These requirements can be met with the latest advances in ocean technology and miniaturization (Whitt et al., 2020).

Over the last few years, ocean observing systems have evolved to make necessary observations possible through the development and implementation of gliders and wave gliders, Argo floats (including Biogeochemical (BGC-Argo), Deep), and unmanned surface vehicles (USVs) (Thurnherr et al., 2015; Braga et al., 2017; Jayne et al., 2017; Hall et al., 2019; Whitt et al., 2020). These platforms can be at sea for many months and a number of sensors can be placed on them to measure various ocean variables. For example, a wave glider, powered by wave energy, is used for underway surface carbon measurements in the open ocean and coastal waters with excellent durability in rough seas over eight months (Willcox et al., 2009). It acts like an airplane; the vertical motion of the submersed glider through the water column allows its wings to convert some of this upward motion to forward propulsion force (Hine et al., 2009). BCG-Argo floats can provide high-resolution and cost-effective measurements of the water column compared to ship-based surveys. Most Argo floats are parked at a depth of 1,000 meters, and they profile the ocean by going down to 2,000 meters, deep Argo floats down to 6,000 meters, and gradually moving up to the sea surface at 10-day cycles (Roemmich et al., 2019). They are equipped with multiple submersible autonomous sensors for measurements of

EOVs. The acquired data is sent to the satellite via iridium and processed in different laboratories and regions of the world. There are nearly 4,000 active floats in the ocean now, and data is accessible online (https://biogeochemical-argo.org/). The floats which can measure temperature and salinity have been extremely important in understanding the structure and the current systems in the oceans. AUVs, propeller-driven, are capable of doing large surveys of ocean variables like nitrate and oxygen in relatively short times (Johnson and Needoba, 2008). Very novel sail drone surface vehicles, equipped with multiple sensors, can acquire data at the air-sea interface up to 12 months by sailing on the ocean (Vazquez-Cuervo et al., 2019; Gentemann et al., 2020).For more than two decades, the number of sensors utilized on autonomous platforms has been increasing (Schofield et al., 2010; Tintoré et al., 2013; Whitt et al., 2020). To date, various submersible sensors exist for autonomous, real-time, and in situ monitoring of a range of EOVs (Wang et al., 2019). Each sensing technology has unique advantages, challenges, and maturity levels. NASA has classified the maturity of the sensors into nine levels, called technology readiness levels, from TRL 1 (least mature) to 9 (highest mature) (Olechowski et al., 2015; Héder, 2017). Sensor prototypes at TRL 7-8 level produce excellent data on many platforms, and those reaching TRL 9 are commercialized.

Some of today's most advanced sensors are for physical parameters like ocean conductivity-temperature-depth (CTD), which were developed in the 1960s (Brown, 1991). Over the past few decades, Sea-Bird Scientific's CTD units (https://www.seabird.com/) have been widely used on BCG-Argo floats and other autonomous platforms around the world (Wong et al., 2020). The next most advanced oceanographic sensor is the Aanderaa oxygen optode (Aanderaa Data Instruments AS), and still improvements are made to them (Bittig et al., 2018). While some biogeochemical sensors, such as dissolved inorganic carbon, total alkalinity, phosphate, and trace metal (like iron, manganese), are still at relatively lower TRLs, bulky and expensive, others like pH and nitrate sensors are at TRL 9, a range of commercial units are available from different manufacturers (Sastri et al., 2019; Wang et al., 2019; Daniel et al., 2020; Geißler et al., 2021). Small size, low power and reagent consumption, and low cost are main requirements for in situ biogeochemical sensors. Current state-of-the-art pH and nitrate sensors are detailed in Chapters 2 and 3.

A global network of biogeochemical sensors, such as the BCG-Argo Program (https://biogeochemical-argo.org/), OceanOPS (https://www.ocean-ops.org/board), and Global Ocean Data Analysis Project (GLODAP, https://www.glodap.info/), is an important step forward to meet the enormous geographical scales of the oceans better. Such networks have the potential to make the data available to broader communities, including non-academics. However, the volume of data obtained is drastically increasing in line with the increasing number of autonomous platforms and advanced ocean observation systems with sensors deployed to measure a range of EOVs (Tanhua et al., 2019). Handling large datasets with harmonized documentation is one of the main challenges in this context. Wilkinson et al. (2016) introduced the FAIR (Findable, Accessible, Interoperable, and Reusable) Data Principles to support data management with a modernized form of scientific communication. Later, Hörstmann et al. (2020) issued an "Intergovernmental Oceanographic Commission (IOC) Manual and Guide" for increased FAIRness particular to the operational oceanography community, which has become globally significant across data providers and users. Ocean Best Practices (OBP) system was founded with the goal "to have methods that are accepted and widely adopted across ocean exploration, operations and practices" as stated by them, and is an open-access repository of best practices (oceanbestpractices.org) documentation (Pearlman et al., 2019). The OBP perspective enables better coordination and interdisciplinary understanding of various methods and data (Hörstmann et al., 2021).

The broad background knowledge required to conduct automated, high-resolution, in situ monitoring strategies of essential biogeochemical parameters is a base for this research focusing on specific sensors. The questions for this Ph.D. thesis are: Which particular ocean observational areas are in most need of autonomous, high-resolution, in situ data? What is the maturity level of commercially available sensing technologies? What needs to be done to improve output data quality utilising an OBP approach?

1.1.2. The Marine Carbonate Chemistry: Significance and Monitoring Strategies of pH

Since the beginning of the Industrial Era (mid-18th century), carbon dioxide levels in the atmosphere have increased over 40% as a consequence of combustion of fossil fuels, cement production and land-use changes, and projections expect that this will continue to rise under the current circumstances. **Figure 1.2** shows the monthly mean of atmospheric CO_2 concentration at Mauna Loa Observatory from 1958 to 2021, and the current levels are about 413.93 ppm in October 2021 (Retrieved from https://gml.noaa.gov/ccgg/trends/).

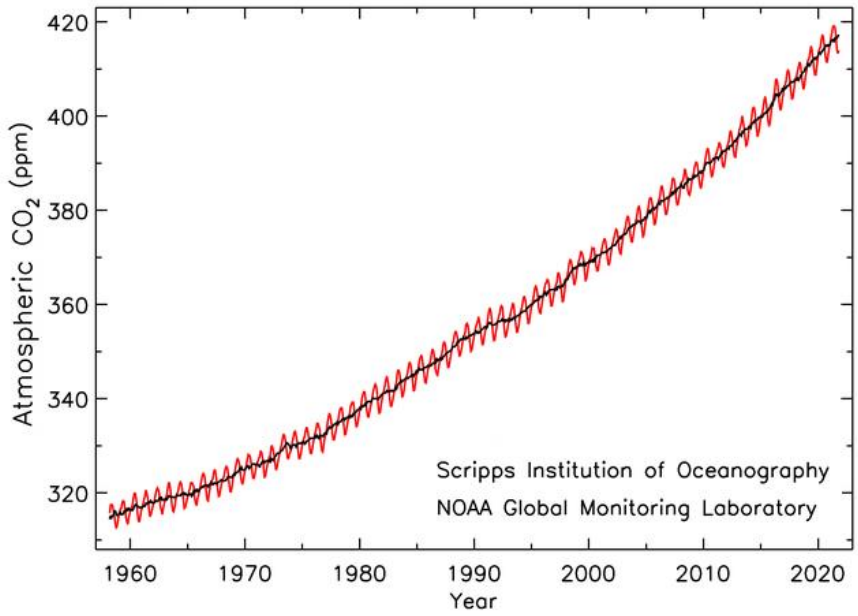

Figure 1.2: Time series of monthly average atmospheric CO_2 levels (ppm) between 1958 and 2021 at Mauna Loa Observatory in Hawaii maintained by NOAA Global Monitoring Laboratory and the Scripps Institute of Oceanography
(Source: https://gml.noaa.gov/ccgg/trends/).

The ocean is a significant component of the global carbon cycle as it plays an essential role in regulating atmospheric CO_2 levels. Over the past 200 years the oceans have absorbed about 30% of global anthropogenic CO_2 emissions (Le Quéré et al., 2010).

Ocean acidification (ongoing decrease in the pH value due to rising CO_2 levels in the ocean, (Doney et al., 2009)) has been a global phenomenon for decades, and it has received public attention in recent years.

The average surface ocean pH has dropped 0.1 units from 8.21 to 8.10 since the pre-industrial period (Royal Society, 2005), and projections report that pH will further drop about 0.1–0.4 by 2100 and about 0.3–0.7 by 2300 (Caldeira and Wickett, 2003, 2005; Doney et al., 2009).

Marine carbonate chemistry describes the processes of dissolution of CO_2 in the ocean and its consequences for the marine ecosystem. When CO_2 dissolves in surface seawater, it is converted into a carbonic acid [H_2CO_3], hydrogen [H^+], bicarbonate [HCO_3^-], and carbonate [CO_3^{2-}] ions (Byrne, 2014) as follows:

$$CO_{2\,(g)} \leftrightarrow CO_{2\,(aq)} + H_2O \leftrightarrow H_2CO_3 \leftrightarrow [HCO_3^-] + [H^+] \leftrightarrow [CO_3^{2-}] + [H^+]$$

Of the carbonate system variables shown above, only four can be analytically determined: pH, the partial pressure of carbon dioxide (pCO_2), dissolved inorganic carbon (DIC) and total alkalinity (A_T) (Millero, 2007). Measuring a pair of these four variables allows quantification of the rest with some uncertainty (Millero, 2007; Cullison Gray et al., 2011).

The mathematical expression of pH, a measure of the concentrations of [H^+] on a logarithmic scale, is as follows:

$$pH = -log[H^+]$$

pH is a "master variable" defining the chemical properties of aqueous solutions, controlling the speciation and solubility of numerous dissolved inorganic elements and trace metals (C, P, Fe, Al, As, Cu, Cd, Si, V, Zn) (Gundersen and Steinnes, 2003; Doney et al., 2009; Kroeker et al., 2013; Garg et al., 2018; Bagshaw et al., 2021). Therefore, it is essential to monitor the pH levels of marine waters globally. The pH measurements, for example, can be used to quantify the carbon cycle in the ocean (Zhang, 2000) and calculate surface pCO_2 levels (Williams et al., 2017).

The first measurement of seawater pH can be traced back to the early 20th century (Sørensen and Palitzsch, 1910). Until the late 1980s, glass electrodes were used to measure seawater pH with uncertainties of about 0.1 units. The development of spectrophotometric pH measurement methods in the 1990s (Byrne and Breland, 1989; Clayton and Byrne, 1993; Dickson, 1993) marked a milestone for detecting minor pH changes, such as those expected from ocean acidification.

Traditionally, the analysis of discretely collected seawater samples is done in the laboratory using a benchtop spectrophotometer. Yet, this method is labor and cost-inefficient and the device itself big, bulky and not submersible. In order to cope with the vastness, remoteness, and complexity of the ocean, there is a need to increase the spatial and temporal resolution of measurements (Wang et al., 2019).

Considering the advantages of in situ ocean monitoring discussed in section 1.1.1., submersible spectrophotometric pH sensors have been developed. Further developments in ocean acidification sensor technology are still ongoing today. Detailed reviews of in situ sensors for ocean acidification research, as well as needs and availabilities, can be found in the literature (Rérolle et al., 2012; Martz et al., 2015b; Bushinsky et al., 2019; Sastri et al., 2019; Tilbrook et al., 2019; Wang et al., 2019; Wright-Fairbanks et al., 2020).

Table 1.1 presents the list of some commercially available and custom-made sensors for marine carbonate system. To date, many pH sensors are available based on potentiometric, fluorescent, and spectrophotometric methods. Each sensor has unique potentials and limits (Moore et al., 2009; Rérolle et al., 2012; Sastri et al., 2019).

Briefly, the potentiometric pH sensors like Honeywell Durafet Ion-Sensitive Field Effect Transistor (ISFET) are based on the detection of the difference in voltage values between the reference electrode and the source electrode. The sensor voltage can be converted to pH values using the *Nernst equation* (Bresnahan et al., 2014). Potentiometric pH sensors are advantageous due to high-resolution measurements (6 s per measurement) with no chemical reagents. However, their application is limited to waters with a salinity of 20 to 40 (Sea-Bird Electronics, Inc.). They require preconditioning for about 5 to 10 days and frequent calibration to maintain the stability of the reference electrode and overcome potential drift, which is in the order of 0.03-0.05 pH units (Sabine et al., 2004; Martz et al., 2010; Bresnahan et al., 2014; Johnson et al., 2016; Mclaughlin et al., 2017; Miller et al., 2018).

Fluorescent-based pH optodes utilize pH-sensitive indicator dyes fixed in a matrix or polymer layer (termed sensor spot). The protonated and deprotonated forms of the indicator have different fluorescence (light emission) intensities at different wavelengths. Although these sensors are cost-effective and easily miniaturized, since they do not require reference electrodes and moving components, they have low maturity levels compared to potentiometric and

spectrophotometric pH sensors. The main drawbacks of the pH optodes are the high light sensitivity of the sensor spot, and ionic strength dependence of measurements (-0.01 pH units per salinity between 25 and 35) (Clarke et al., 2015). Moreover, biofouling is an issue for long-term deployments, and also measurements need to be corrected for drift over time (Staudinger et al., 2018).

The analytical principle of spectrophotometric pH measurement relies on the color change of a seawater sample after the addition of pH-sensitive chemical dye (a sulfonephthalein compound) (Dickson, 2010). The sample pH is related to the absorbance of protonated and deprotonated dye forms. Although the sensors consist of pumps, valves, and other microfluidic components for the injection of the sample, and dye, they are advantageous for being robust, stable, and calibration-free (Rérolle et al., 2012). The most reliable approach for determining seawater pH has shown to be the spectrophotometric method (Okazaki et al., 2017; Müller et al., 2018). Various studies reported successful deployments of spectrophotometric sensors in a wide variety of environments for fine-scale pH monitoring (in the order of 0.001 units) (Martz et al., 2003; Seidel et al., 2008; Aßmann et al., 2011; Darlington, 2017; Müller et al., 2018; Rérolle et al., 2018; Yin et al., 2021). The detailed theory of the spectrophotometric method, equations used to calculate pH, field applications and the accuracy levels of various pH sensors are described in Chapter 2.

Besides pH, pCO_2 and A_T can be monitored using submersible or underway autonomous sensors. As yet, while the number of reports on field deployments and in situ analysis of pCO2 and A_T are still scarce, pH sensors have the highest maturity levels among all (Wang et al., 2019). The pH data from the sensors listed in **Table 1.1** are in the total pH scale (pH_T), the most favourable in oceanography among other scales (NBS, free, and seawater) (Mosley et al., 2004; Dickson, 2010; Fassbender et al., 2020). Although the spectrophotometric pH sensors are well-established in the frame of ocean best practices, there is still a need to evaluate the performance of the particular sensor in a range of environments, such as coastal waters, surface and deep ocean waters.

In Chapter 2, we present a field deployment of the LOC pH sensor in highly dynamic estuarine and coastal waters of the Kiel Fjord. In addition, we briefly review the advantages and limitations of commercially existing technologies with current accuracy levels for monitoring pH.

Table 1.1: Some of the commercially available marine carbonate system sensors.

Parameter	**Method**	**Model, Manufacturer**	**Reference**
pH_T	Potentiometric	Durafet ISFET, Honeywell International Inc., USA	(Martz et al., 2010; Bresnahan et al., 2014; Johnson et al., 2016; Gonski et al., 2018)
		SeaFET, Sea-Bird Scientific, USA	(Miller et al., 2018)
pH_T	Fluorescent	pH Optode, Custom-made	(Clarke et al., 2015; Staudinger et al., 2018)
pH_T	Spectrophotometric	CONTROS HydroFIA pH, Kongsberg, Germany	(Aßmann et al., 2011; Müller et al., 2018)
		SAMI-pH, iSAMI, Sunburst Sensors, LLC, USA	(Seidel et al., 2008; Darlington, 2017)
		LOC pH, ClearWater Sensors Ltd, UK	(Rérolle et al., 2018; Yin et al., 2021)
pCO_2	Fluorescent	Aanderaa optode 4797, Aanderaa, Norway	(Atamanchuk et al., 2014)
pCO_2	NDIR	CONTROS HydroC CO_2, Kongsberg, Germany	(Marrec et al., 2014)
		CO_2-Pro, Pro-Oceanus, Canada	(Jiang et al., 2014)
pCO_2	Spectrophotometric	SAMI-CO_2, Sunburst Sensors, LLC, USA	(DeGrandpre et al., 1995)
A_T	Spectrophotometric	CONTROS HydroFIA TA, Kongsberg, Germany	(Seelmann et al., 2020)
		SAMI-Alk, Sunburst Sensors, LLC, USA	(Spaulding et al., 2014)

1.1.3. Macronutrients of the Ocean: Significance and Monitoring Strategies of Nitrate

Macronutrients (dissolved inorganic nitrogen, phosphate, and silicic acid) play an essential role in marine biogeochemical processes and are key water quality indicators. The concentration levels of macronutrients (in the range of micromoles per liter, $\mu mol \cdot L^{-1}$) differ by several orders of magnitude between different marine environments: coastal waters, surface and deep ocean waters. The availability of macronutrients in marine ecosystems is mainly governed by natural processes, such as atmospheric deposition, organic matter decomposition, lightning, and geological formations. However, a range of anthropogenic processes (enhanced use of fertilizers, anthropogenic inputs to coastal waters from domestic and industrial wastes) affect the nutrient supply tor marine microbial organisms, thereby changing the state of marine ecosystems. The health of oceans depends on a balance between multiple elements and factors. For example, phytoplankton build their biomass with a stoichiometric carbon-to-nitrogen-to-phosphorus (C:N:P) ratio of 106:16:1, known as the *Redfield ratio* (Redfield, 1958).

Nitrogen is a key element for all forms of life and is the fourth most abundant element after carbon, oxygen, and hydrogen in organic matter (Zehr and Kudela, 2011). It is available in different chemical forms and has oxidation states between -3 and +5. Major chemical forms of nitrogen in the marine environment are nitrate (NO_3^-), ammonium (NH_4^+), nitrite (NO_2^-), dinitrogen (N_2), nitrous oxide (N_2O), dissolved organic nitrogen (DON, e.g. amino acids) and urea ($(NH_2)_2CO$) (Zehr and Kudela, 2011). **Figure 1.3** presents the conversion of nitrogen forms with related microbial processes (such as nitrate assimilation, denitrification, nitrification, and anammox) in the water column. The assimilation of NO_3^-, NO_2^- and NH_4^+ is related to the photosynthetic fixation of carbon by phytoplankton. Nitrification is defined as conversion of the fixed organic nitrogen to NO_3^- by remineralisation processes, and denitrification is the sequential reduction of nitrogen from NO_3^- to N_2.

The transformation of NO_2^- and NH_4^+ to N_2 is referred to as anammox process and only occurs in anoxic waters (Gruber, 2008; Voss et al., 2013). These microbial processes also affect the habitat of nitrogen forms. For example, in surface waters, nitrogen fixation is an important process and N_2 is the most abundant form but only accessible by nitrogen-fixing microorganisms. NH_4^+, NO_2^-, DON, and $(NH_2)_2CO$ are mostly present in low concentrations, as they are rapidly recycled and assimilated by autotrophic and heterotrophic organisms. In coastal upwelling zones and in deep ocean NO_3^- is the dominant form of bioavailable nitrogen (Zehr and Kudela, 2011).

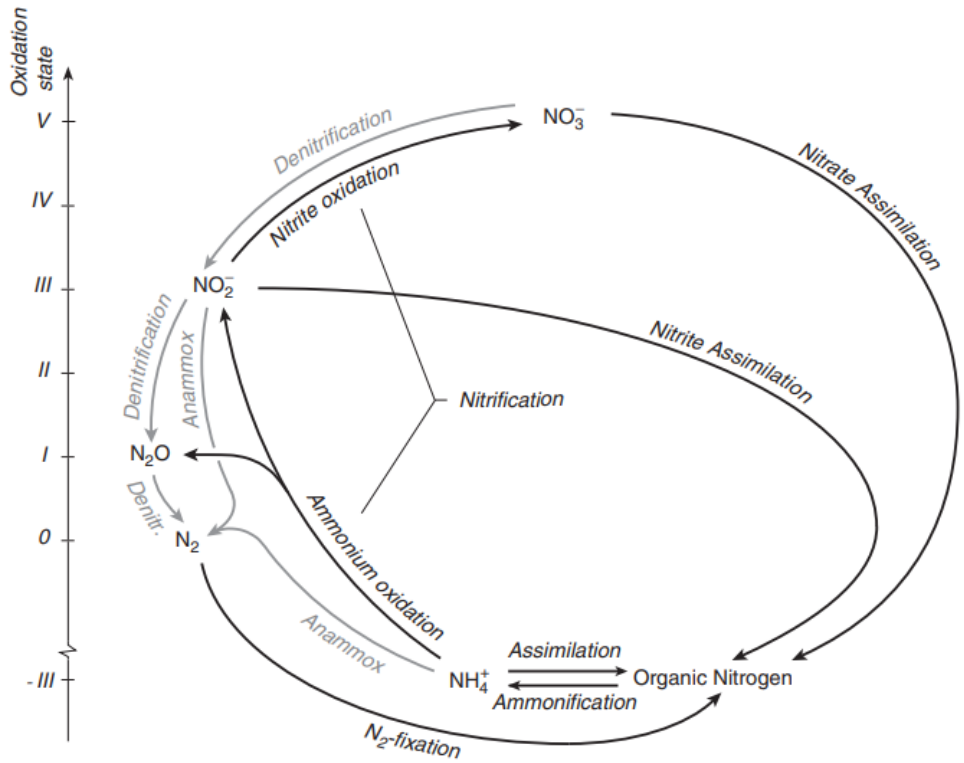

Figure 1.3: The oxidation states of nitrogen in the marine environment and microbial processes related to the transformation of major nitrogen forms. Processes shown in grey is valid only in anoxic environments (Source: Gruber, 2008).

Nitrate (NO_3^-) is the primary nutrient utilised for photosynthesis and primary production. Oceans have a dynamic distribution of NO_3^- concentrations ranging from nearly nanomolar (nM) levels in tropical and subtropical surface waters, to several tens of µM in the Arctic and Antarctic Oceans (Voss et al., 2013).

A depletion or an increase in NO_3^- levels negatively affect marine ecosystems; for example, under low NO_3^- conditions primary production is limited and when NO_3^-supply is enhanced excessive growth or eutrophication may occur. Therefore, monitoring NO_3^- levels in marine waters helps us to understand the state of the ecosystem. NO_3^- is a routinely analyzed parameter in oceanographic studies based on conventional methods of discrete collection of bottled seawater samples and a benchtop laboratory analysis (Hansen and Koroleff, 1999). However, the spatial and temporal resolution of conventional analysis is not sufficient for obtaining an ecosystem-scale perspective. Currently, a suite of wet-chemical colorimetric and ultraviolet (UV) spectrophotometric sensors exist to assess NO_3^- in situ and overcome the under-sampling issue with discrete water sampling (Daniel et al., 2020). The sensors proved to be suitable for measurements of NO_3^- concentrations in almost all natural waters (Zielinski et al., 2007; Sakamoto et al., 2009, 2017b; Beaton et al., 2011, 2017; Johnson et al., 2013; Frank et al., 2014; Pasqueron de Fommervault et al., 2015). The wet-chemical colorimetric sensors have a high sensitivity but the drawback of requiring chemical reagents, waste storage, and using fragile moving microfluidic components like syringes, pumps, and valves. To date, the most common commercially available NO_3^- sensors are based on the UV spectrophotometric principle, as they do not require chemical reagents and are suitable for high-resolution, cost-effective, long-term monitoring. However, the validity of the NO_3^- data must be carefully assessed. The analytical principle of the UV spectrophotometric sensors is based on the determination of light absorbed by the sample in a particular wavelength range. The absorbed light is then proportional to the concentration of the NO_3^- from *Beer Lambert's Law*.

NO_3^- naturally absorbs light in the UV wavelengths below 240 nm (Johnson and Coletti, 2002). However, at the same wavelength range other natural compounds in seawater like bromide (Br^-) absorb light, and interfere with the NO_3^- measurements. The quality of NO_3^- data, therefore, depends on elaborate mathematical corrections, which is specific to a particular sensor. So far, several algorithms have been proposed to successfully estimate the Br^- absorbance (using the temperature, salinity, and pressure dependence of its absorption spectra) in raw spectral data before computing NO_3^- concentrations (Sakamoto et al., 2009, 2017a; Frank et al., 2014; Pasqueron de Fommervault et al., 2015; Johnson et al., 2018).

In Chapter 3, we describe the principle of hyperspectral nitrate detection, the data post-processing algorithm used to compensate for interferences, the accuracy levels of multiple sensors, and highlight the need for standardizing the data processing of optical nitrate sensors by taking the sensor-specific properties into account. In addition, we provide new insights specific to the TriOS OPUS sensor used for high-resolution, in situ monitoring of nitrate in marine waters.

1.1.4. Principle of Spectrophotometers: The Current Advantages and Limitations of Compact Versions

Spectrophotometers have a broad range of applications in various branches such as chemical, environmental, pharmaceutical, medical, and astronomical instrumentations. The instruments are composed of four main components: a light source, a sample holder, a monochromator, and a detector.

The basic principle is that each chemical substance or solution interacts with light (such as absorbance transmission, reflection, scattering) over a particular wavelength range. Then, spectrophotometers detect the amount of light that passes through the sample (Germer; et al., 2014). The quantity of light interaction is directly related to the concentration of the solution, as stated by the *Beer-Lambert Law*, and the mathematical expression is as follows;

$$A = \varepsilon \cdot l \cdot c$$

where A is the absorbance, ε is the molar extinction coefficient or molar absorptivity, and c is the concentration of the sample solution. l is the patch length of light in the sample cuvette.

The commercialization of the first instrumental spectrophotometry can be traced back to the mid-1930s by Dr. Arnold J. Beckman and his colleagues at National Technologies Laboratories (Arnold and Mabel Beckman Foundation). Since then, it has been a convenient tool for the analysis of most chemical compounds.

The improvements in spectrophotometric devices are still ongoing to meet the requirements of complex applications better. Although the classical benchtop spectrophotometers are high in sensitivity with low stray light (Germer; et al., 2014), their large dimensions limit their field applications in real-time and in situ. Advancements in technology and miniaturization have allowed the reduction of benchtop instruments to handheld-scale without sacrificing performance.

To date, a wide range of compact spectrophotometers is available from various manufacturers, i.e., Hamamatsu Photonics, Avantes, StellarNet Inc., Ocean Insight, Zeiss, etc. New generation, compact spectrophotometers are highly portable, rapid, and cost-effective. They can also be embedded in submersible environmental monitoring devices to provide on-site measurements, such as the optical sensors presented throughout the thesis. **Figure 1.4** shows an exemplary illustration of a classic benchtop and modern compact analyzers. In general, compact spectrometers are more sensitive to stray light than benchtop versions; the increased noise may interpret as a signal, leading to misinterpretation of the measured data. Besides, real-time and in situ spectrophotometric measurements in highly dynamic marine waters are challenging compared to measurements of discretely collected water samples under laboratory conditions. Both physical and electronic limitations of detectors may enhance the noise in the measured signal, which restricts their use in some dynamic environmental applications. Therefore, compensating for potential interference and improving the signal-to-noise ratio have been the goal of various studies to obtain high-quality spectral data using compact spectrophotometers. In Chapter 4, the potential noise sources (dark currents, temperature variations, blooming, the uncertainty of integration time, wavelength calibration, stray light, and detector non-linearity) are explained in detail. In theory, the detector signal should increase linearly with increasing light intensity. However, any deviation from this can seriously affect the quality of data. We provide optimization work to overcome this specific to the compact charge-coupled device (CCD) spectrometer, the core element of optical sensors used in autonomous ocean observation studies.

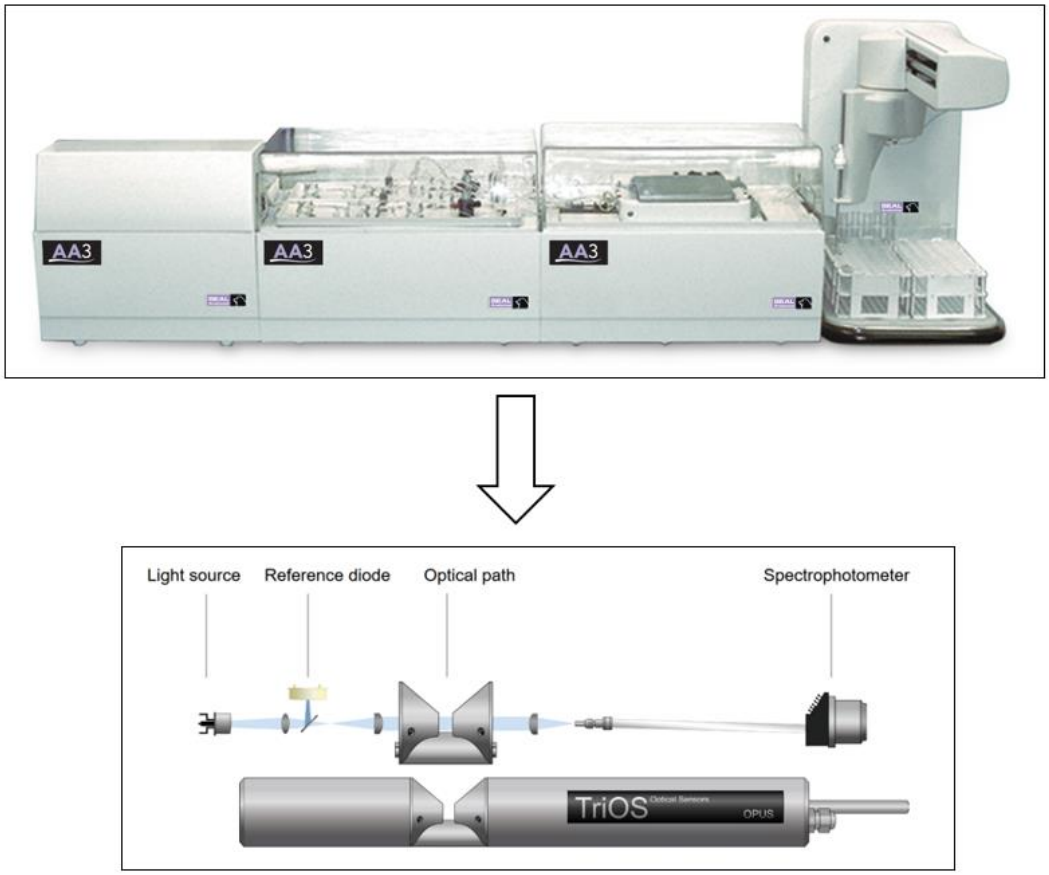

Figure 1.4: An example demonstration of the evolution of spectrophotometric analysers from lab to field: a benchtop SEAL AA3 Flow Injection Nutrient Analyser and a submersible optical nitrate sensor.

(Retrieved from: https://seal-analytical.com/Products/Segmented-Flow-Analyzers/AA3-HR-AutoAnalyzer and TriOS GmbH, 2017).

1.2. Dissertation and Chapter Overview

The overarching goal of this Doctoral thesis is to improve and demonstrate autonomous chemical sensors for marine waters, with a particular focus on the optimization of sensors based on the spectrophotometric method. The dissertation is written in a cumulative manner and subdivided into the following five chapters. Chapters 2, 3 and 4 have been published in peer-reviewed journals.

This introductory **Chapter 1** describes the necessary theoretical background of the particular ocean observational areas (in most need of autonomous, high-resolution, in situ data) and present levels of autonomous sensing technologies for marine waters. Additionally, this chapter gives an overview of current autonomous ocean observing systems with their advantages and drawbacks and highlights the main research gaps.

Currently, spectrophotometric pH sensors are at the highest maturity level among submersible carbonate chemistry analyzers. **Chapter 2** investigates the performance of an automated, submersible spectrophotometric analyzer, a LOC sensor, for high-resolution in situ pH determinations in dynamic estuarine and coastal waters. The sensor was deployed in Kiel (Germany) in the southwest of the Baltic Sea. Its suitability to reveal pH dynamics on a fine-scale was assessed. In situ pH data from the LOC sensor were compared with those from benchtop laboratory analysis of discrete water samples. This chapter has been published as:

Münevver Nehir, Mario Esposito, Socratis Loucaides, Eric P. Achterberg: **Field Application of Automated Spectrophotometric Analyzer for High-Resolution In Situ Monitoring of pH in Dynamic Estuarine and Coastal Waters, *doi.org/10.3389/fmars.2022.891876***

Author Contributions: Münevver Nehir performed the laboratory and field work, statistical analysis and data visualization. Mario Esposito performed the installation of the sensors on the deployment platform. Münevver Nehir wrote the first draft of the manuscript. All authors contributed to the article and approved the submitted version.

TriOS OPUS UV sensor, which is portable, reagent-free, small in size, and light in weight, is the latest version of commercially available optical nitrate sensors for marine waters. **Chapter 3** describes the optimization efforts for the TriOS OPUS UV sensor and explains the need to improve output data quality utilizing an OBP approach by providing advanced calibration and data processing procedures. To assess whether the calibration coefficients were sensor dependent, five OPUS were deployed simultaneously under the same conditions in the laboratory, and similarities and differences among sensors were evaluated. In situ data from the field deployments of the sensor, through underway surface measurements in the southeastern North Sea and vertical profiles (down to 4,000 meters depth) on a CTD frame in the tropical Atlantic Ocean, were evaluated against the reference discrete water samples. This chapter has been published as:

Münevver Nehir, Mario Esposito, Christian Begler, Carsten Frank, Oliver Zielinski, Eric P. Achterberg: **Improved Calibration and Data Processing Procedures of OPUS Optical Sensor for High-Resolution in situ Monitoring of Nitrate in Seawater, *doi.org/10.3389/fmars.2021.663800***

Author Contributions: Münevver Nehir and Eric P. Achterberg conceptualized the study and methodology. Christian Begler and Oliver Zielinski supported experimental tools. Christian Begler provided initial Matlab scripts and assisted in the development of the OPUS controller. Mario Esposito assisted during laboratory and field tests. Münevver Nehir wrote the article with edits and contributions from all co-authors.

Compact charge-coupled device (CCD) spectrometers are a core component of various analytical laboratory devices and autonomous sensors. The physical and electronic capabilities of CCD spectrometers may limit their usability as analytical applications become more complex. **Chapter 4** describes a more technical aspect of optimizing spectrophotometers to improve the signal-to-noise ratio of readings and expand the use of CCD spectrometers by proposing a simple experimental approach to compensate for their nonlinear effects. A Hamamatsu C10082CA mini-spectrometer was used to display the results for each pixel. This chapter has been published as:

Münevver Nehir, Carsten Frank, Steffen Aßmann, Eric P. Achterberg: **Improving Optical Measurements: Non-Linearity Compensation of Compact Charge-Coupled Device (CCD) Spectrometers, *doi.org/10.3390/s19122833***

Author Contributions: Carsten Frank and Steffen Aßmann developed the concept of this study. Münevver Nehir, Carsten Frank, Steffen Aßmann and Eric P. Achterberg contributed to the implementation of the research, to the analysis of the results, and the preparation of the manuscript.

Chapter 5 finalizes the dissertation with a summary of the main findings and concluding remarks for the oceanographic community, also gives future suggestions to fill the gaps in current knowledge.

2. Field Application of Automated Spectrophotometric Analyzer for High-Resolution In Situ Monitoring of pH in Dynamic Estuarine and Coastal Waters

Münevver Nehir[1,*], Mario Esposito[1], Socratis Loucaides[2], Eric P. Achterberg[1]

Published in *Frontiers in Marine Science*

DOI: 10.3389/fmars.2022.891876

[1] GEOMAR Helmholtz Centre for Ocean Research Kiel, Wischhofstr. 1-3, 24148 Kiel, Germany

[2] National Oceanography Centre, Southampton, Southampton SO14 3ZH, UK

Abstract

High quality pH measurements are required in estuarine and coastal waters to assess the impacts of anthropogenic atmospheric CO_2 emissions on the marine carbonate system, including the resulting decrease in pH. In addition, pH measurements are needed to determine impacts on carbonate chemistry of phytoplankton blooms and their breakdown, following enhanced anthropogenic nutrient inputs. The spectrophotometric pH technique provides high quality pH data in seawater, and is advantageous for long-term deployments as it is not prone to drift and does not require in situ calibration. In this study, a field application of a fully automated submersible spectrophotometric analyzer for high-resolution in situ pH measurements in dynamic estuarine and coastal waters is presented. A Lab-on-Chip (LOC) pH sensor was deployed from a pontoon in the inner Kiel Fjord, southwestern Baltic Sea, for a total period of 6 weeks. We present a time-series of in situ pH_T (total pH scale) and ancillary data, with sensor validation using discretely collected samples for pH_T and laboratory analysis. The difference between the sensor and laboratory analyses of discrete samples was within ±0.015 pH_T unit, with a mean difference of 0.001 (n=65), demonstrating that the LOC sensor can provide stable and accurate pH_T measurements over several weeks.

Keywords: pH sensor, Lab-on-Chip, Spectrophotometric, mCP, Kiel Fjord, coastal carbonate system, ocean acidification.

2.1. Introduction

The oceans play a significant role in the global carbon cycle as one of the main reservoirs of carbon. Since the beginning of the Industrial Revolution, anthropogenic CO_2 emissions have perturbed the exchange of CO_2 between the atmosphere and oceans. Oceans have absorbed about a quarter of anthropogenic carbon dioxide (CO_2) emissions (Friedlingstein et al., 2020), a process causing a long-term pH decrease (ocean acidification). To date, several studies have focused on determining the progression of ocean acidification by using long-term ocean observations datasets (Dore et al., 2009; Midorikawa et al., 2010; Hu et al., 2015; Van Dam and Wang, 2019; Ishida et al., 2021). Time-series measurements of surface ocean pH over the past two decades have reported a decrease of about 0.1 units since the pre-industrial era from ca. 8.2 to 8.1 (Orr et al., 2005). An additional decrease in surface ocean pH of more than 0.4 units is expected by the end of the 21st century (Feely et al., 2009; Jiang et al., 2019; Kwiatkowski et al., 2020).

Estuarine and coastal waters are more complex than open ocean waters and are highly dynamic environments where freshwater discharges mix with seawater, with many systems impacted by anthropogenic activities. For example, nutrient run-off results in eutrophication with the ensuing breakdown of organic matter produced by phytoplankton blooms causing high pCO_2 and reduced pH values, adding to the acidification caused by anthropogenic CO_2 uptake (Wallace et al., 2014; Zhao et al., 2020). The acidification of estuarine and coastal waters is affecting ecosystems negatively and various biogeochemical processes in a water column (Guinotte and Fabry, 2008; Hall et al., 2020; Thomas et al., 2022). For example, enhanced acidic conditions threaten the growth, abundance, and survival of shell-forming organisms (corals, some plankton species, and commercial shellfish (Doney et al., 2020; Fox et al., 2020; Wilson et al., 2020; Blaisdell et al., 2021) and affect the solubility and speciation of trace metals (Millero et al., 2009; Hoffmann et al., 2012). To improve our

understanding of the current state of the kinetics and dynamics of various physical and biogeochemical processes in estuarine and coastal waters, monitoring activities with a high-resolution are essential (Carstensen et al., 2018), and pH is one of the keystone parameters to be observed.

High-resolution measurements of pH are essential for tracking the thermodynamic state of acid-base processes in seawater. pH is a measure of the concentrations of hydrogen ion on a logarithmic scale and one of the four measurable parameters of the marine carbonate system. Others are the partial pressure of carbon dioxide (pCO_2), dissolved inorganic carbon (DIC) and total alkalinity (A_T) (Millero, 2007). The gaseous form of CO_2 dissolve in surface waters and is converted into carbonic acid (H_2CO_3), hydrogen (H^+), bicarbonate (HCO_3^-), carbonate (CO_3^{2-}) ions (Dickson et al., 2007) as follows:

$$CO_{2\,(g)} \leftrightarrow CO_{2\,(aq)}$$

$$CO_{2\,(aq)} + H_2O_{(l)} \leftrightarrow H_2CO_{3\,(aq)}$$

$$H_2CO_{3\,(aq)} \leftrightarrow HCO_3^-{}_{(aq)} + H^+{}_{(aq)}$$

$$HCO_3^-{}_{(aq)} \leftrightarrow CO_3^{2-}{}_{(aq)} + H^+{}_{(aq)}$$

Four different seawater pH scales; NBS (U.S. National Bureau of Standards), free, total, and seawater, are described in literature and the total scale is favoured in oceanography as it includes the effect of sulfate ions (Mosley et al., 2004; Dickson, 2010; Fassbender et al., 2020). The calculation of the dissociation constant of the sulfate ion can be eliminated using the total proton scale (Zeebe and Wolf-Gladrow, 2001). All pH data reported in this study are on the total $[H^+]_T$ scale, expressed as: $pH_T = H^+ + HSO_4^-$.

The traditional carbonate chemistry observations in marine systems are based on discrete water sample collection, storage, transportation, and land-based laboratory analysis. Discrete water samples for carbonate chemistry can be collected using dedicated samplers such as Niskin bottles, and then stored following poisoning using mercuric chloride until laboratory analysis for pH,

DIC and A_T using standard operational procedures (Dickson et al., 2007). pH can be determined directly using potentiometric or spectrophotometric techniques (Dickson et al. (2007), but also calculated via the CO2Sys software following e.g. A_T and DIC measurements (Lewis and Wallace, 1998; Pierrot et al., 2006). The main limitations of this approach are the inadequate temporal resolution and duration and the high costs associated with the collection, preservation, shipping, and analysis of samples.

Advancements in marine technology and observational oceanography have enabled the development of miniaturized in situ pH sensors that can be integrated into stationary or autonomous platform for monitoring marine environments at a high temporal and spatial resolution (Sastri et al., 2019). To date, a range of pH sensors have been reported for autonomous in situ pH measurements, and are based on three different analytical methods, potentiometry (electrodes), fluorescence (optodes) and, spectrophotometry (indicator dyes). **Table 2.1** presents examples of the current in situ pH sensors and their application in multiple oceanographic studies. Each system has a range of advantages and limitations (Rérolle et al., 2012, 2018; Sastri et al., 2019). Potentiometric pH sensors for seawater (i.e., Honeywell Durafet Ion-Sensitive Field Effect Transistor (ISFET), SeaFET, SeapHOx) do not require chemical reagents and have a fast sampling frequency (6 seconds per measurement), but measurements are limited to a salinity range between 20 and 40 (Sea-Bird Electronics, Inc.). Besides, Honeywell Durafet based pH sensors may be prone to drift (potentially more than 0.02 pH unit/week) (Rérolle et al., 2016), therefore require preconditioning of the electrode for 5 to 10 days and frequent calibrations (Sabine et al., 2004; Martz et al., 2010; Bresnahan et al., 2014; Mclaughlin et al., 2017; Miller et al., 2018). To date, the Deep Sea Durafet sensor has been deployed on a range of profiling floats, and the assessment and correction for any potential drift to reduce bias in the pH measurements have been comprehensively evaluated by Johnson et al., 2016. Recent work introduced a self-calibrating SeapHOx system for seawater,

periodic flushing of the sample cell with a calibration solution of Tris buffer in artificial seawater (Bresnahan et al., 2021), which is yet limited to seawater applications. The main limitations of fluorescent-based pH measurements are the interfering compounds of natural seawater (i.e., chlorophyll-a), drift with time, and the sensor spot is also light sensitive (Clarke et al., 2015). Staudinger et al. (2018) presented a stand-alone optode sensor system for pH, oxygen, and carbon dioxide with an integrated battery and logger and its short-term applications in the Baltic Sea and mentioned the need for drift correction and assessment of biofouling for long-term deployments.

The spectrophotometric method for pH, developed in the 1980s (Robert-Baldo et al., 1985), provides many advantages for marine studies as it is robust, stable, calibration-free and not prone to drift (Rérolle et al., 2012). Under oceanic conditions, spectrophotometric pH measurement systems have demonstrated excellent performance (Clayton and Byrne, 1993; Bellerby et al., 2002; Aßmann et al., 2011; Rérolle et al., 2016). Commercially available, submersible spectrophotometric sensors (see **Table 2.1**, Lab-on-Chip (LOC) and SAMI-pH) have been successfully tested for fine-scale, autonomous and in situ monitoring of pH in a wide variety of environments, from freshwater (Martz et al., 2003) to seawater (Seidel et al., 2008; Rérolle et al., 2018; Yin et al., 2021). Indicator impurities and wavelength accuracy of spectrophotometers are some of the potential sources of uncertainty in spectrophotometric pH measurements, which DeGrandpre et al. (2014) has reported in detail. The quality of the pH data is related to how well the molar extinction coefficients and the second dissociation constant of an indicator dye have been determined as a function of sample temperature and salinity. To date, the experimental characterization and modelling of a meta-Cresol Purple (mCP) for estuarine ($S \leq 20$, Mosley et al., 2004; Lai et al., 2016, 2017; Douglas and Byrne, 2017b; Müller and Rehder, 2018) and hypersaline ($35 \leq S \leq 100$, Loucaides et al., 2017) waters have been reported.

Table 2.1: Examples of the current in situ pH sensors used in oceanographic studies.

Model, Manufacturer	**Analytical method**	**pH Monitoring Applications**
Honeywell Durafet ISFET, SeaFET and SeapHOx (Sea-Bird Electronics, USA)	Potentiometric	Deployment of ISFET pH sensor on vertical profiling platforms from 2,000 m to the surface over several months (Johnson et al., 2016): <0.010 pH units accuracy. Deployment of ISFET pH sensor in coastal waters over months periods (Bresnahan et al., 2014): <0.030 pH units accuracy. Commercially available SeaFET and SeapHOx sensors based on ISFET technology: ±0.050 pH units accuracy (https://www.seabird.com/seafet-v2-ocean-ph-sensor/product-details?id=54627921732&callback=qs). SeaFET pH sensor deployment in coastal waters of south-central Alaska, USA for a period of 3 to 5 months (Miller et al., 2018): <0.025 pH units accuracy.
pH optodes (Custom-made)	Fluorescent optode	Shipboard surface seawater measurements in the Southern Ocean, over a month (Clarke et al., 2015): accuracy is not reported, 0.0074 pH units precision. Profiling on a pier in Southampton, UK, for 6 days (Staudinger et al., 2018): 0.020 pH units accuracy.
SAMI-pH (Sunburst Sensors, LLC, USA)	Spectrophotometric	Coastal waters, deployment at the pier at Scripps Institution of Oceanography for about 22 days (Seidel et al., 2008): ±0.0017 pH units accuracy. Commercially available SAMI-pH sensor: ±0.003 pH units accuracy (http://www.sunburstsensors.com/products/oceanographic-ph-sensor.html).
CONTROS HydroFIA-pH (4H-Jena engineering GmbH, Germany)	Spectrophotometric	Shipboard measurements in the North Sea over 6 weeks period (Aßmann et al., 2011): 0.0081 pH units accuracy compared to CRM and 0.0005 pH units to a reference system, short-term precision: ± 0.0007. Note: The sensor is a benchtop unit, not yet submersible.
National Oceanography Centre, University of Southampton, UK, Lab-on-Chip pH (ClearWater Sensors, Southampton, UK)	Spectrophotometric	Deployed in surface waters of northwest European shelf seas for about a month period (Rérolle et al., 2018): 0.004 pH units accuracy compared to CRM. Deployed on fixed and moving platforms over varying environmental salinity, temperature, and pressure condition (Yin et al., 2021): +0.003 ± 0.022 pH units accuracy compared to discrete validation seawater samples.

Recently, the capabilities of the LOC pH sensor have been successfully demonstrated on fixed and moving platforms under different environmental conditions, including deployments in surface waters of Southampton (S>24) for several months, and in deep ocean waters (~4820 m) (Yin et al., 2021). However, the performance of this LOC pH sensor in estuarine and coastal waters has not yet been thoroughly investigated.

The aim of this study was to evaluate the performance of an automated spectrophotometric analyser, a LOC sensor, for high-resolution in situ pH determinations in dynamic estuarine and coastal waters, and expand the applicability of the sensor to waters with a wide salinity range (13.2-21.8). The sensor was deployed from a floating pontoon at GEOMAR Helmholtz Centre for Ocean Research (Kiel, Germany) in the southwestern Baltic Sea between summer and autumn 2018 for a total period of 6 weeks. Ancillary data were obtained to assess the control of pH dynamics at the sampling site. Additional spectrophotometric pH_T measurements were conducted in the laboratory on discretely collected samples, and the measurements were validated with certified reference material (DIC-A_T CRM, Batch-151, obtained from Prof. A. G. Dickson at Scripps Institute of Oceanography, USA).

2.2. Materials and Methods

2.2.1. Sensor Overview

The LOC pH sensor is a submersible unit that performs autonomous in situ pH analysis with a spectrophotometric technique using microfluidic components and was initially developed in 2012 by the Ocean Technology and Engineering group at National Oceanography Centre (NOC) and University of Southampton, UK (Rérolle et al., 2013). It is now (since 2021) commercially available from ClearWater Sensors, Southampton, UK. A schematic diagram of the fluidic design of the sensor is shown in **Figure 2.1**. All components were mounted on a three-layer microfluidic chip made from tinted

poly(methylmethacrylate) (PMMA) (Floquet et al., 2011; Perez et al., 2016), and together with the electronics placed in a mineral oil-filled (M3516 from Merck, viscosity≤30.0cps) pressure compensated, watertight cylindrical polyvinylchloride housing (15 cm diameter, 56 cm height, 920 g weight in air). Detailed information of the sensor housing and microfluidic chip unit can be found in (Grand et al., 2017).

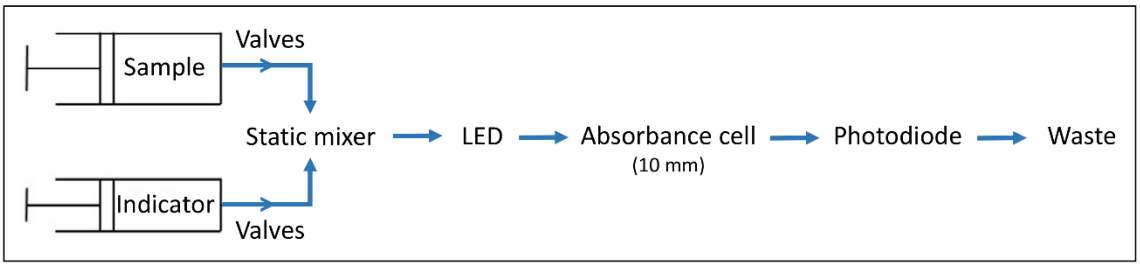

Figure 2.1: The schematic diagram of the fluidic design of the LOC pH sensor.

The operation of the sensor is explained in brief here. A sample and indicator dye are injected by two separate syringe pumps, controlled by valves, and mixed in a static mixer before entering a 10 mm optical cell. The change in the intensity of light transmitted by a Light Emitting Diode (LED, Roithner Lasertechnik, Austria) at 435 nm (15 nm full width at half maximum (FWHM)) and 590 nm (15 nm FWHM) through the optical cell is recorded by a photodiode detector (TSL257, TAOS Inc., USA) (Floquet et al., 2011; Rérolle et al., 2013; Perez et al., 2016). To account for slight discrepancies between the wavelengths of the LED's emission and the mCP's absorption maxima (434 and 578 nm) the pH sensor is calibrated post-manufacture according to Yang et al. (2014). The ratio of absorbances at the absorbance maxima of the acidic and basic forms of the indicator dye is then used to assess the pH value of a sample (Clayton and Byrne, 1993). In continuous operation mode, the sensor requires low power about 3 W or 1300 J per measurement and one measurement takes approximately 8 minutes (Yin et al., 2021). For each measurement, 3 µl of indicator dye is added to 700 µl of sample according to a pre-programmed

measurement routine stored internally on the sensor unit. Approximately 0.4 mL of indicator is consumed per day when the sensor operates in continuous mode. Stock solutions of mCP are stored in 50 mL gas impermeable Flexboy bags (Sartorius Stedim Biotech, UK), wrapped in black tape to protect from light and avoid photo bleaching. The mCP stock solution remains stable for several months up to 2 years, when stored appropriately (Takeshita et al., 2021). It is possible to conduct up to 16.666 analyses with one reagent bag of 50 mL, which was attached externally to the LOC pH unit. Waste was collected into an additional external bag attached to the sensor. The WetChem Graphical User Interface (GUI) was used to operate the sensor and visualize intensity values, measurement time, pump position, internal temperature in real-time.

2.2.2. Analytical Principle and Data Processing of the LOC pH Sensor

The analytical principle of spectrophotometric pH determination is based on an addition of a pH-sensitive diprotic sulfonephthalein indicator dye (H_2I) to a water sample. The dye changes color according to the pH of the seawater sample, i.e., the color changes from pink to yellow when it is in the acidic [HI^-] and to purple when it is in the more basic [I^{2-}] form (Clayton and Byrne, 1993). Chemical equilibria between three dissociation forms of the dye can be expressed as follows:

$$H_2I \overset{K_1}{\Leftrightarrow} HI^- + H^+ \qquad K_1 = \frac{[H_2I]}{[H^+] \cdot [HI^-]} \tag{1}$$

$$HI^- \overset{K_2}{\Leftrightarrow} I^{2-} + H^+ \qquad K_2 = \frac{[HI^-]}{[H^+] \cdot [I^{2-}]} \tag{2}$$

where [] indicates concentration, K_1 and K_2 are first and second dissociation constant of the indicator, respectively. The pK_2 (in other terms $-log(K_2)$) of mCP is close to the pH of seawater, which is typically between 7.6 to 8.3 (Dickson et al., 2007).

The pH of a seawater sample ($pH = -log[H^+]$) can then be quantified as:

$$\mathrm{pH_T} = -log(K_2) + log\left(\frac{[I^{2-}]}{[HI^-]}\right) \quad (3)$$

According to the *Beer-Lambert Law*, the amount of [I^{2-}] and [HI^-] can be calculated using their distinct absorption properties at 434 and 578 nm:

$$\mathrm{A_\lambda} = \left(\varepsilon_\lambda^{\mathrm{I^{2-}}} \cdot [\mathrm{I^{2-}}] + \varepsilon_\lambda^{\mathrm{HI^-}} \cdot [\mathrm{HI^-}]\right) \cdot l \quad (4)$$

where A_λ is the absorbance, ε_λ is the molar absorptivity values at wavelength λ, and l is the optical path length.

Then, the equation used to quantify pH can be rearranged as follows:

$$\mathrm{pH_T} = -log(K_2 e_2) + log\left(\frac{\mathrm{R} - e_1}{1 - \mathrm{R} \cdot \frac{e_3}{e_2}}\right)$$

$$\text{where } e_1 = \frac{\varepsilon_{578}^{[\mathrm{HI^-}]}}{\varepsilon_{434}^{[\mathrm{HI^-}]}}, e_2 = \frac{\varepsilon_{578}^{[\mathrm{I^{2-}}]}}{\varepsilon_{434}^{[\mathrm{HI^-}]}}, e_3 = \frac{\varepsilon_{434}^{[\mathrm{I^{2-}}]}}{\varepsilon_{434}^{[\mathrm{HI^-}]}} \quad (5)$$

where R is the ratio of absorbance at 578 (maximum peak for [I^{2-}]) to 434 nm (maximum peak for [HI^-]), R = A_{578} / A_{434} (Clayton and Byrne, 1993; Liu et al., 2011).

A recent study reports on the characterization of a range of sulfonephthalein indicator dyes in detail, including mCP, for a broad range of environmental conditions (Hudson-Heck et al., 2021). Data processing of the LOC sensors raw data involves computation of molar extinction coefficients (in terms of *e1, e3/e2*), and second dissociation constant value (pK_2) of mCP at sample temperature and salinity using the equations and coefficients obtained from the literature (*e1, e3/e2* were computed from (Liu et al., 2011) and pK_2 was

computed from Müller and Rehder, 2018, which is valid for salinity range 5-20 and temperature range 5-35°C). In situ temperature and salinity data of the sample were collected in parallel by external sensors (see section 2.2.3.).

In this study, a purified mCP (Acros Organics, 99%) indicator dye was used as its ε_λ and pK_2 are well-established for estuarine waters (Lai et al., 2016, 2017; Müller and Rehder, 2018). The purification of mCP was done by following the protocol described in Liu et al. (2011) and Loucaides et al. (2017). A 4 mM mCP reagent solution adjusted to pH 8.0±0.1 at 25°C was prepared and verified by a glass pH electrode.

2.2.3. Field Deployments: Sampling site and ancillary data

In situ field demonstration of the LOC pH sensor was performed on a floating pontoon facility of GEOMAR (Kiel, Germany; 54°19'48.78″N, 10° 8'59.44″E) for a period of 6 weeks between August 1st to 13th and October 20th to November 19th, 2018. The sampling site is surrounded by dockyards and cruise ship terminals, and the city of Kiel with a population of ca. 250,000. The Kiel Fjord has a length of 9.5 km, an inner width of 250 m with depth of 10 to 12 m, an outer width of up to 7.5 km with depths greater than 20 m (Nikulina et al., 2008). The fjord drains into the southwest Baltic Sea. The waters in the inner fjord are homogeneously mixed, except during the summer period following water column stratification. Most of the freshwater delivered to the system is from rainwater and the Schwentine River on the eastern shore (Nikulina et al., 2008).

The LOC sensor was programmed to sample at hourly intervals (except for the first 5 days in August: 20 min intervals). A 0.45 µm Millex HP PES in-line filter (Millipore, Merck, Darmstadt, Germany) was placed at the sample inlet of the LOC sensor to prevent particles from entering the microfluidic channels (Rérolle et al., 2013). The filter surface area is relatively large compared to the volume of sample withdrawn and therefore no significant underpressure is

required to draw sample through. The sensor was powered externally by a 12 V power supply.

Salinity, temperature and oxygen were measured with a sampling interval of one minute using a SBE 37-SMP-ODO MicroCAT CTD and dissolved oxygen (DO, dO_2) sensor (Sea-Bird Electronics, USA). The LOC, CTD, and DO sensors were mounted on a stainless steel sensor frame that was lowered from the side of the pontoon and positioned at a depth of ca 2 m. Discrete water samples were collected daily, once in the morning and/or once in the evening, using a peristaltic pump (Cole Palmer, Masterflex L/S series) placed on the floating pontoon. The inlet of an acid cleaned (with 1 M HCl) 6.4 mm ID C-Flex tubing (Cole Palmer Masterflex) was attached to the frame close to the sample inlet of the LOC pH sensor. Discrete seawater samples for direct spectrophotometric laboratory analysis of pH_T (Yin et al., 2021) were pumped into 250 mL borosilicate bottles and sealed with a ground stopper. Analyses of unpreserved samples were performed within few hours in the laboratory using a benchtop spectrophotometric CONTROS HydroFIA pH analyzer (4H-Jena engineering GmbH, Aßmann et al., 2011). Measurements of the LOC sensor and HydroFIA analyzer were validated using the DIC-A_T CRM (Batch-151, pH_T 7.862 at temperature 25°C and salinity 33) from Prof. A. G. Dickson (Scripps Institute of Oceanography, USA) before and after deployments. The correction of sample pH_T was done using equations described in section 2.2 and in situ temperature and salinity values. Seawater samples of inorganic nutrients (NO_3^-, PO_4^{3-} and SiO_4^{-4}) were collected after filtration through an AcroPak 500 (Pall GmbH, Germany) in acid-cleaned (1 M HCl) 50 mL polypropylene centrifuge tubes (Jet Bio-Filtration Co., Ltd., Guangzhou, China) and stored at -20°C for about a month until the wet-chemical colorimetric laboratory analysis using a Seal QuAAtro autoanalyser (Becker et al., 2019).

The GEOMAR pontoon facility is used for continuous time-series measurements of various biogeochemical and physical parameters in Kiel Fjord as part of the KIMOCC environmental data monitoring program. Here, we used the one-minute interval post-processed pCO_2 data of the installed CONTROS HydroC CO_2 sensor (4H-Jena engineering GmbH, Germany). An overview of the analytical principle of the CO_2 sensor and data processing can be found in Fietzek et al. (2014). CO2Sys was used to calculate concentration of dissolved CO_2 gas in the water sample. Throughout the study, in situ pCO_2 levels are in µatm and dissolved CO_2 gas levels are in $\mu mol \cdot kg^{-1}$ SW. Weather data (wind speed, rainfall, solar irradiation) were obtained from the GEOMAR weather station, and were available for every 8 min. The tide gauge water level (meter) measurements at Kiel Fjord were obtained from the IOC Sea Level Monitoring Facility (http://www.ioc-sealevelmonitoring.org/station.php?code=kiel). All sensors and ancillary data presented throughout this study were examined and processed using Python software (version 3.7.4).

2.3. Results and Discussion

2.3.1. Validation of in situ pH sensor measurements

A total of 65 individual samples were collected during deployments that were analyzed employing a benchtop spectrophotometric analyzer to ensure the accuracy of pH values reported using the LOC sensor. The LOC sensor and discrete water samples pH data followed a consistent pattern throughout both deployments (**Figure 2.2a**) and were significantly indifferent (a paired t-test, $p \leq 0.05$). A linear regression yielded $y=0.998x+0.004$ ($R^2=0.99$) for a total of 65 samples. No offset was applied to the sensor data and both sensor and discrete pH results were calculated independently. The average difference between the sensor and discrete samples pH (ΔpH_T=LOC sensor-discrete water samples) was 0.001 pH units, but ranged from -0.015 to 0.015 over the duration of the summer and autumn deployments (**Figure 2.3**). No clear correlation was

found between ΔpH_T and ancillary data (T, S, dO_2), however, the relationship between pH_T and ancillary data will be detailed in the next section. Additional validation of the sensor pH measurements was done by calculating pH_T from salinity-derived A_T and in situ pCO_2. Computational details of salinity-derived A_T will be clarified in section 2.3.2. pH data from the summer and autumn deployments pooled together and for a total pH value of 978, a linear regression analysis resulted in R^2 =0.86, with an equation of y=1.030x-0.217 (**Figure 2.2b**).

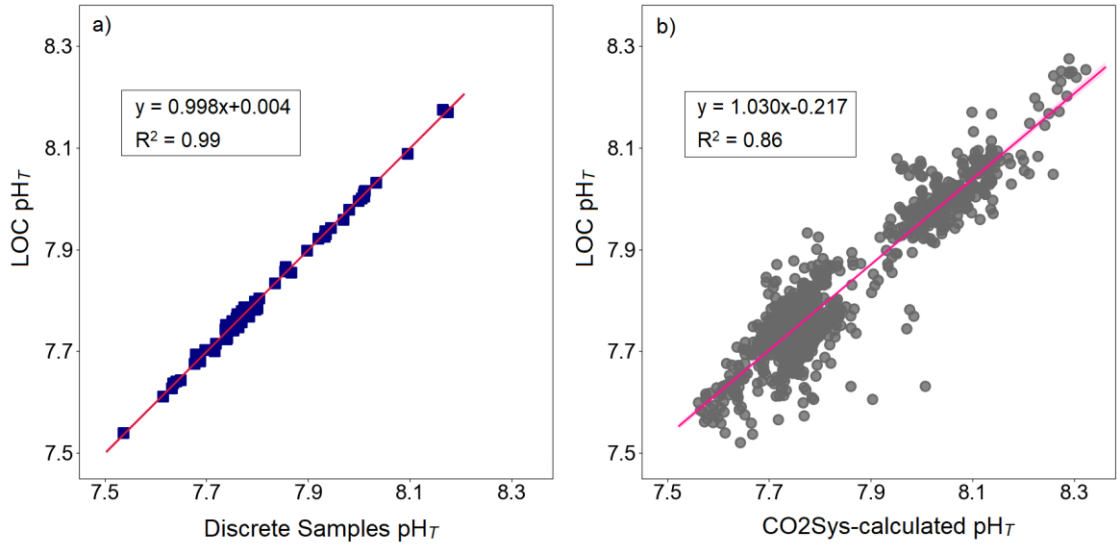

Figure 2.2: Linear regression fits between all summer and autumn pH_T values obtained from a) discrete water samples vs LOC sensor (data: blue squares, linear fit; solid red line, n=65), and b) CO2Sys-calculation vs LOC sensor (data: grey circles, linear fit; solid pink line, n=978).

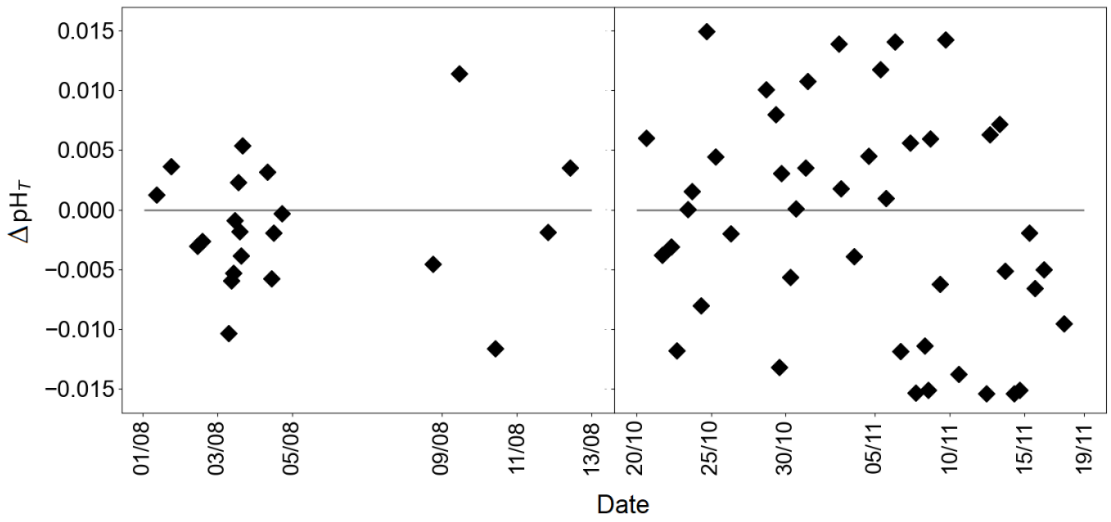

Figure 2.3: The residuals of ΔpH_T (LOC sensor-discrete water samples) over the duration of summer and autumn deployments, respectively.

Both the LOC sensor and HydroFIA analyzer measurements were validated by consecutive measurements of DIC-TA Certified Reference Material (CRM) (Batch-151, pH_T=7.862 at T=25°C, S=33) before and after the field deployments. The mean pH values obtained from ten consecutive CRM measurements in July, September, and November 2018 were 7.858±0.002, 7.860±0.002 and 7.859±0.001 pH units for the LOC pH sensor and 7.861±0.001, 7.862±0.002 and 7.860±0.001 pH units for the HydroFIA pH analyzer. Both analyzers had a precision about 0.001 pH units, and the accuracy of the measurements were slightly better with the HydroFIA analyzer (<0.002 pH units).

2.3.2. Statistical distribution and diel variations of in situ pH and ancillary data

The main focus of this work was to demonstrate the capability of the LOC pH sensor in a highly dynamic system, and analysis of the biogeochemical data was completed to investigate the biogeochemical processes influencing carbonate chemistry dynamics in the Kiel Fjord. The statistical distribution of all data (seawater temperature, salinity, pH_T, dO_2, pCO_2, NO_3^-, PO_4^{3-} and SiO_4^{-4} is presented in **Table 2.2** and allows a closer examination of the summer and autumn data. The seawater temperature and salinity, characterizing the hydrographic situation, showed marked changes; the mean salinity values were about 4 units higher and the mean temperature values were about 10 units lower in autumn, indicating saltier and colder water intrusion in the fjord, with fresher waters in summer. Highly dynamic salinity conditions for Kiel Fjord ranging from 2.6 to 22.4 have been reported, with a mean of 14.3 (Schories et al., 2006). During our summer deployment the salinity values ranged between 13.2 and 18 (mean 15.7), and in autumn deployment within 19.6 to 21.8 (mean 20.7). Enhanced seawater temperatures ranging between 18.1 and 24.2°C (mean 22.1°C) characterized the summer deployment. In autumn, temperature dropped to a minimum value of 8.7 and ranged up to 14.1°C (mean 11.5°C).

The LOC sensor determined in situ pH_T values were within 7.520-8.275 (mean 7.954) and within 7.560-7.932 (mean, 7.742) in summer and autumn, respectively. High mean pCO_2 levels were observed related to lower pH values towards autumn. The pCO_2 values ranged between 264-1446 µatm (mean 845 µatm) in summer and between 521-1402 µatm (mean, 904 µatm) in autumn. The dO_2 observations showed values between 4.5-9.5 $mg \cdot L^{-1}$ (mean 7.3 $mg \cdot L^{-1}$) in summer, and 5.8-8.7 $mg \cdot L^{-1}$ (mean, 7.7 $mg \cdot L^{-1}$) in autumn, respectively. Although, the mean dO_2 levels were almost identical in two seasons, dO_2 levels were about two times more dynamic in summer (ΔdO_2 was 5 $mg \cdot L^{-1}$ in summer and 2.9 $mg \cdot L^{-1}$ in autumn, respectively).

Table 2.2: Summary statistics for in situ pH_T and ancillary data from summer and autumn deployments. Δ refers to the difference between maximum and minimum values, n is the sample size.

Parameter	Summer	Autumn	Parameter	Summer	Autumn
T (°C)			**dO_2 (mg·L^{-1})**		
Mean	22.1	11.5	Mean	7.3	7.7
Min-Max	18.1-24.2	8.7-14.1	Min-Max	4.5-9.5	5.8-8.7
ΔT	6.1	5.4	ΔdO_2	5	2.9
n	1,325	6,483	n	1,170	6,477
S			**NO_3^-(µM)**		
Mean	15.7	20.7	Mean	0.31	2.09
Min-Max	13.2-18.0	19.6-21.8	Min-Max	0.08-	0.84-3.83
ΔS	4.8	2.2	ΔNO_3^-	0.81	2.99
n	1,325	6,483	n	0.73	75
				32	
pH_T			**PO_4^{3-} (µM)**		
(Sensor)	7.954	7.742	Mean	0.47	1.30
Mean	7.520-	7.560-	Min-Max	0.16-	1.11-1.55
Min-Max	8.275	7.932	ΔPO_4^{3-}	1.51	0.44
ΔpH_T	0.755	0.372	n	1.35	75
n	346	632		32	
pCO_2(µatm)			**SiO_4^{4-}(µM)**		
Mean	845	904	Mean	9.12	24.3
Min-Max	264-1446	521-1402	Min-Max	1.7-23.3	19.9-28.6
ΔpCO_2	1182	881	ΔSiO_4^{4-}	21.6	8.7
n	53,293	41,756	n	32	75

Discretely analyzed samples of nutrients exhibited that NO_3^- concentrations in summer were depleted with values between 0.08 and 0.81 µM (mean 0.31 µM), and was followed by an increase in autumn, with concentrations between 0.84 and 3.83 µM (mean 2.09 µM). Mean PO_4^{3-} and SiO_4^{-4} concentrations were also higher in autumn. In summer, the concentration range for PO_4^{3-} was 0.16-1.51 µM (mean 0.47 µM) and for SiO_4^{-4} 1.7-23.3 µM (mean 9.12 µM), whilst in autumn PO_4^{3-} concentrations varied from 1.1 to 1.55 µM (mean 1.30 µM) and SiO_4^{-4} from 19.9 to 28.6 µM (mean 24.3 µM). The wind speed was maximum 11 m·s^{-1} in summer (mean 3.2 m·s^{-1}), and 13 m·s^{-1} in autumn (mean 4.1 m·s^{-1}).

Diel variations of seawater temperature, salinity, pH_T, and ancillary variables (pCO_2, A_T, dO_2, nutrients, water level, solar irradiance and wind speed) obtained during the first deployment in summer 2018 are presented in Figure 4. A total of 346 LOC sensor measurements and 21 discrete seawater samples for pH and 32 for nutrients were collected from August 1 to August 13 on the GEOMAR pontoon facility in Kiel Fjord. The 3-day gap in the dataset, between August 5 and 8, was associated with an electrical failure of the power supply to the sensor. The ranges of all variables and the number of samples measured are presented in **Table 2.2**.

Co-located deployment of independent sensors facilitated the validation of the time-series data at a higher spatial and temporal resolution than can be achieved by analysis of discrete samples (Martz et al., 2015). Considering the high diel variability in temperature, salinity, pH_T, and the ancillary data presented in **Figure 2.4**, there was a clear difference between the waters sampled at the beginning and end of the deployment. At the beginning of the deployment period until about August 9, 2018, it can be stated that there was not much activity in the water, referring to tidal ranges (difference between high tide and low tide) below 0.3 m and relatively stable ancillary data.

A rapid decrease in pH_T from 8.249 to 7.573 (determined by the LOC sensor), increase in pCO_2 from 292 to 1029 µatm and decrease in dO_2 from 9.2 to 5.4 $mg \cdot L^{-1}$ was observed within 24 h from August 9 to 10, 2018, corresponded to a heavy storm event with wind speeds up to 11 $m \cdot s^{-1}$. This event coincided with the extreme weather alert from the German Weather Service (https://www.dwd.de/DE/presse/pressemitteilungen/DE/2018/20180830_deutschlandwetter_august_news.html). A typical tidal range for the Fjord is ±1 m (Geißler et al., 2021). The water level, temperature and salinity measurements presented in **Figure 2.4** illustrate the impact of the storm on the sampled waters. The surface waters of the Kiel Fjord are characterized by enhanced temperature and low salinity, as opposed to the bottom waters of low temperature and high

salinity. Shifts in seawater temperature (approximately 3°C decrease) and salinity (approximately 2 units increase) values were observed during the storm. Nutrients were in a trend consistent with pCO_2 and both increased in response to increased wind speed and decreased temperatures (**Figure 2.4**). Enhanced biological activity was evidenced as while nutrients and pCO_2 were increasing, A_T and dO_2 were in decreasing trend. The in situ determined pH_T values were a reflection of pCO_2 and dO_2 levels.

Anomalous characteristics of the Baltic Sea waters with respect to major ions and hence alkalinity do not allow a straightforward calculation of alkalinity using salinity that applies to all regions of the Baltic Sea in general (Hammer et al., 2014; Müller et al., 2016). Müller et al. (2016) describes the temporal alkalinity trends in the Baltic Sea using long-term historical datasets and shows the relationship between alkalinity and salinity at four different basins. Instead, we have theoretically calculated A_T using in situ salinity data from our deployments and the equation for the Atlantic waters ($0°C<T<20°C$, $31<S<37$) from Lee et al. (2006) to compute pH_T using CO2Sys and have a view of A_T values for our study site. During the summer deployment, salinity-derived A_T values ranged between 2205 and 2427 $\mu mol \cdot kg^{-1}$ with a mean of 2267 $\mu mol \cdot kg^{-1}$. Although the salinity-derived A_T values are not exactly suitable for our study area, when the pH_T values calculated using these A_T and in situ pCO_2 data are compared with the sensor pH_T values, a significant relationship is seen (**Figure 2.2b**).

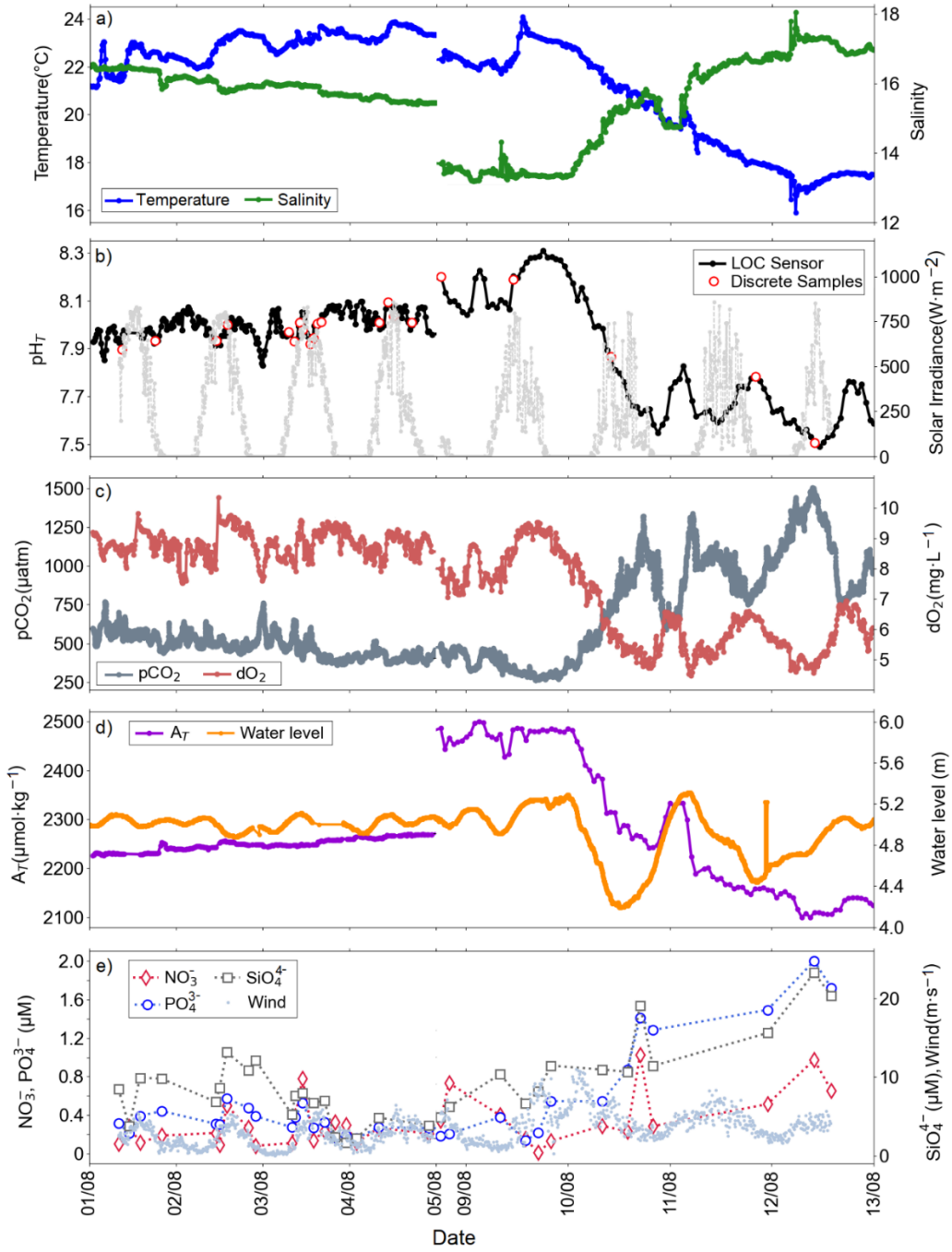

Figure 2.4: Diel variations of a) in situ temperature (blue), in situ salinity (green), b) in situ pH_T (black: LOC sensor, red circles: discrete water samples), solar irradiance (light grey), c) in situ pCO_2 (dark grey), in situ dO_2 (coral), d) salinity-derived A_T (purple), water height (orange), and e) NO_3^- (red diamond), PO_4^{3-}, (blue circles), SiO_4^{-4} (grey squares), and wind speed (pale blue dots) with multiple sensors deployed at the GEOMAR pontoon in Kiel Fjord in summer 2018, from 01.08 to 05.08 and from 08.08 to 13.08.

The second deployment at the same location took place in autumn 2018, from October 20 to November 19, during which 632 LOC sensor measurements were conducted, and discrete seawater samples for discrete seawater samples for pH (n=44) and for nutrients (n=75) were collected. Diel variations of the seawater pH_T and ancillary data are shown in **Figure 2.5** and the corresponding value ranges are provided in **Table 2.2**. The tide gauge water level measurements at Kiel Fjord corresponding to our measuring period indicated that during a heavy storm (wind speed up to ca. 13 $m \cdot s^{-1}$, **Figure 2.5e**), the water level increased by about 1 m (from 4.46 to 5.46 m, **Figure 2.5d**).

During the autumn deployment a further notable weather event occurred starting from October 26th, a storm flood approached at the sampling site, followed by successive winds (speed >10 $m \cdot s^{-1}$) for about 3 days. Over the same period, daily rain intensities (precipitation) of ca. 10 mm were captured, which is a threshold of a heavy rainfall event for Germany (Deumlich and Gericke, 2020), and reductions in water temperature and salinity of about 2 units were observed with additional responses in pH_T, pCO_2, dO_2 and NO_3^- levels. Strongly variable increases in pH_T values were observed, presented in the yellow circle in **Figure 2.5b**, and were not included in **Table 2.2**. This was likely due to the variations in the physical conditions of the fjord waters with winds and tides. The in line filter of the LOC sensor was changed on November 1, 2018, to avoid possible clogging after dynamic water conditions. The gaps (couple of hours) in the LOC sensor dataset between October 25 and 26, as well as November 11 and 12, were related to the power cuts.

The salinity-derived A_T values ranged between 2075 and 2130 µmol·kg^{-1} with a mean of 2099 µmol·kg^{-1} in autumn, much lower than those reported in summer. Compared to the first deployment (**Figure 2.4**), the time series data presented in **Figure 2.5** were relatively uniform with small differences between maximum and minimum values of all parameters (as indicated by low Δ values, **Table 2.2**). An increase in NO_3^- concentrations, from 1.70 to 3.83 µM, was noticed over a one-day period, between November 5 and 6, 2018. The dO_2 levels decreased from 8.5 to 7.9 mg·L^{-1}, whilst pCO_2 levels increased from 704 to 961 µatm. The acidification process was evidenced with decreasing pH values from 7.858 to 7.752. This event can be ascribed to supply of subsurface waters enriched in DIC due to organic matter respiration process (see also section 2.3.3).

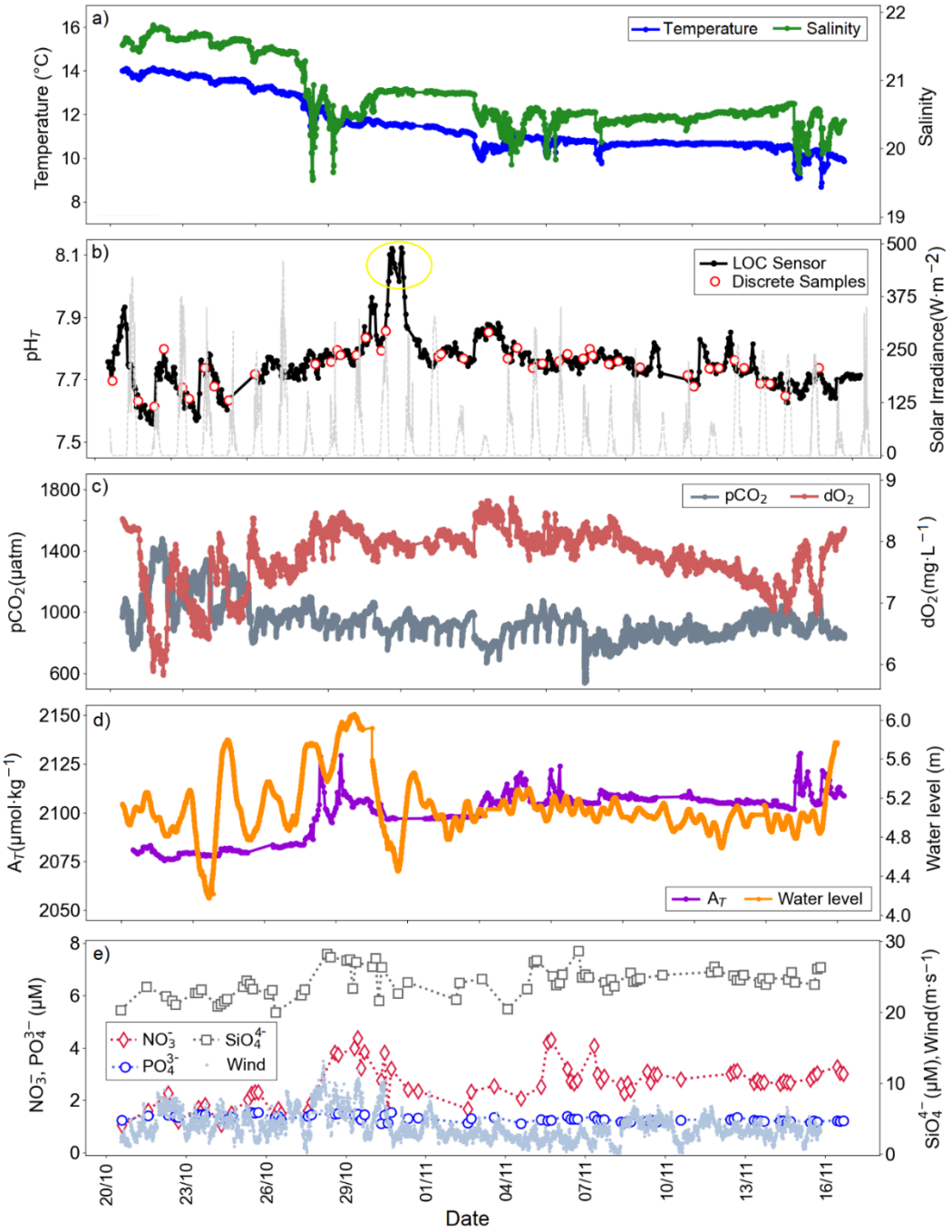

Figure 2.5: Diel variations of a) in situ temperature (blue), in situ salinity (green), b) in situ pH_T (black: LOC sensor, red circles: discrete water samples), solar irradiance (light grey), c) in situ pCO_2 (dark grey), in situ dO_2 (coral), d) salinity-derived A_T (purple), water height (orange), and e) NO_3^- (red diamond), PO_4^{3-}, (blue circles), SiO_4^{-4} (grey squares), and wind speed (pale blue dots) with multiple sensors deployed at the GEOMAR pontoon in Kiel Fjord in autumn 2018, from October 20 to November 19.

2.3.3. Carbonate chemistry dynamics in Kiel Fjord

Estuarine and coastal waters feature complex hydrological conditions, often including strong variations in surface salinity (Castelao et al., 2010). Carbonate chemistry in coastal waters is regulated by variety of factors, including biological metabolic (photosynthesis, respiration, and calcium carbonate precipitation or dissolution), and physical processes (ocean currents, tide, weather conditions) (Kristiansen et al., 2001; Feely et al., 2010; Stokowski et al., 2020; Huang et al., 2021). A change in the mass balance of the carbonate system or thermodynamic conditions of the waters affect the surface pCO_2 levels, consequently the pH dynamics (Dai et al 2009).

pH_T and ancillary data, presented in this study, exhibited clear diel variations (**Figure 2.4 and 2.5**), and the patterns were different in the two seasons, suggesting that distinct internal processes may be involved in regulating these variations. At our deployment site, observations indicated that in the nearshore surface waters of Kiel Fjord were colder, saltier, and more acidic in autumn compared to summer (**Figure 2.6**). The ΔpH_T was 0.372 units in autumn and 0.755 units in summer, respectively.

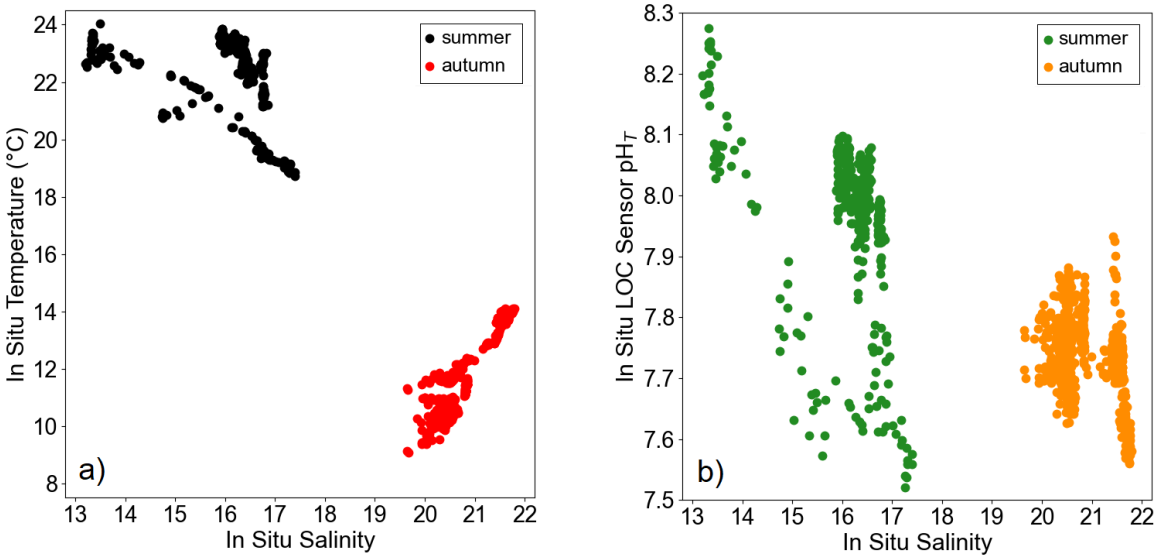

Figure 2.6: In situ a) temperature-salinity and b) pH_T-salinity diagram of the period investigated, illustrating different hydrological periods in summer (black, green circles) and autumn (red, orange circles).

pH, pCO_2 and dO_2 are important indicators for characterizing water masses and biological processes (Orr et al., 2005; Staudinger et al., 2018). An increase in dO_2 concentrations corresponded to an increase in pH and decrease in pCO_2 levels in waters, due to enhanced photosynthetic activity of algae. The mean differences in dO_2 between summer and autumn can also be attributed to the fact that the effect of wind mixing on the water was sharper in our summer distributions, as the waters are generally not well mixed in the summer. The increase in nutrient concentrations and pCO_2 while the dO_2 decreases are evidence of the biological life in the environment. The pH time-series data mirrors that of pCO_2 and dO_2, when fit to a linear regression yielded r^2=0.85 and r^2=0.77 in summer and yielded r^2=0.46 and r^2=0.70 in autumn, respectively (**Figure 2.7**). Besides, pCO_2 data can be considered as a form of validation of the pH data, as in situ measurements were conducted using two different sensors; CONTROS HydroC and LOC.

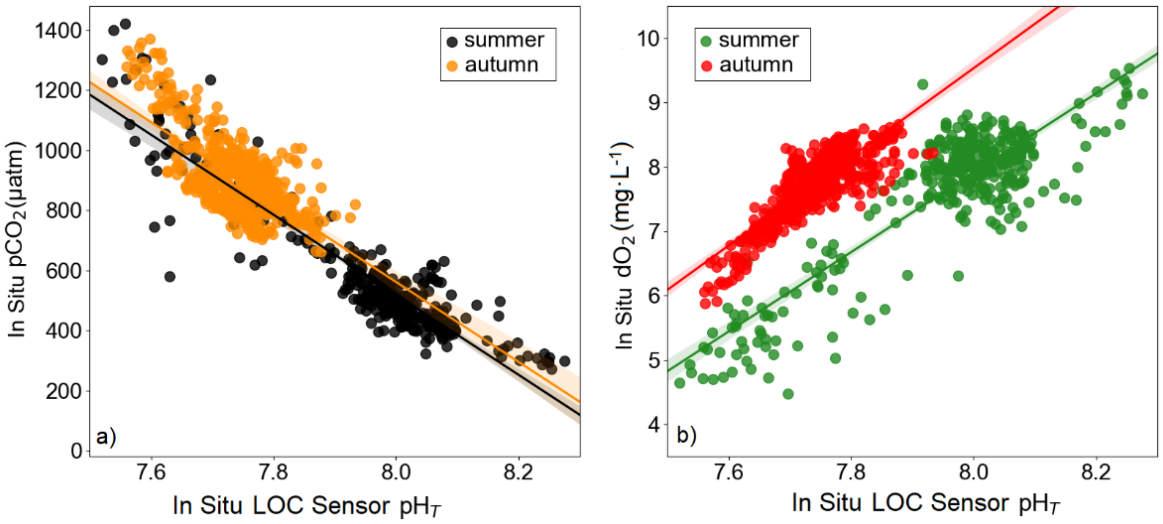

Figure 2.7: Linear regression (solid lines) plots between a) pCO_2 and pH_T (black circles present the data from the summer time-series in situ data presented in Figure 2.4, linear fit yielded r^2=0.85 (n=346) and orange circles present the data from the autumn time-series in situ data presented in Figure 2.5, linear fit yielded r^2=0.46 (n=632), and b) dO_2 and pH_T (green circles present the data from the summer time-series in situ data presented in Figure 2.4, linear fit yielded r^2=0.77 (n=346) and red circles present the data from the autumn time-series in situ data presented in Figure 2.5, linear fit yielded r^2=0.70 (n=632).

The observed Redfield ratios, defining the stoichiometry of the photosynthesis and respiration reactions (Redfield et al., 1963), are shown in **Table 2.3**. The molar ratios between carbon, nitrogen, and phosphorus from simultaneous measurements on the deployment site indicated that the C:N ratio was largely above the proposed Redfield ratio of 106C:16N, which may be related to N loss processes due to denitrification (Gruber, 2008). The N:P ratio in our data was below the Redfield ratio of 16N:1P, which may again be related to N loss through denitrification and additional benthic P supply from anoxic sediments (Lenton and Watson, 2000).

Table 2.3: Molar ratios of C, N and P derived from simultaneous observations during deployment periods.

	C:N Ratio Summer	N:P Ratio Summer	C:N Ratio Autumn	N:P Ratio Autumn
Min	17.6	0.213	10.3	0.650
Max	224	2.64	48.2	3.07
Mean	86.9	0.798	21.8	1.65

Our data from the Kiel Fjord shows strongly elevated in situ pCO_2 (maximum of 1420 µatm) levels, even higher than reported for other estuaries. For example the Polish Oder Estuary which also drains into the Baltic Sea has reported pCO_2 values of <1200 µatm (Stokowski et al., 2020). Higher CO_2 levels were related to nutrient enrichment in the system (**Figure 2.8**), with respiration resulting in O_2 consumption and CO_2 production (**Figure 2.4 and 2.5**).

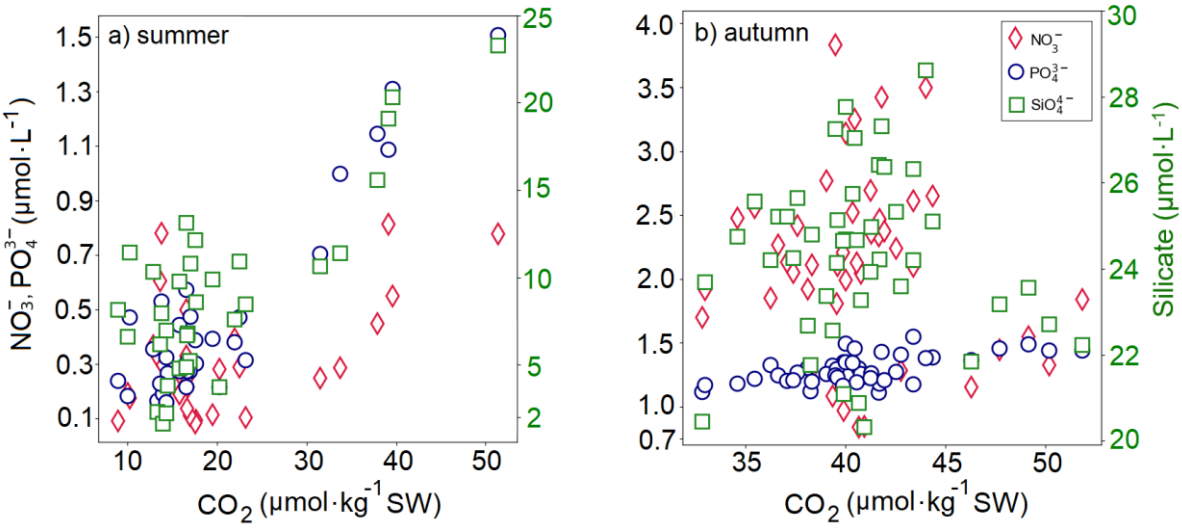

Figure 2.8: Dynamics of in situ concentration of dissolved CO_2 gas in the water sample (calculated using the CO2Sys) vs nutrients during the a) summer and b) autumn deployment.

The physical mixing and enhanced remineralization of organic substances in estuaries, promoted by high nutrient loads from land, determine the chemical composition of the system (Bauer et al., 2013; Stokowski et al., 2020). While it is beyond the scope of this study to precisely quantify the intensity of photosynthesis/respiration processes, studies from different estuaries have suggested that intensity levels of biological activities are modulated by wind-driven inputs of nutrients from subsurface waters (Gazeau et al., 2005; Saderne et al., 2013; Li et al., 2020).

Given our in situ data and the main biological and physical drivers of the carbonate chemistry of the estuarine systems, the carbonate system in Kiel Fjord is regulated by i) respiration, and ii) wind-driven mixing. During the deployment periods storm events were captured, in which subsurface waters (with enhanced pCO_2 and nutrient levels) were transferred to the surface, evidenced by temperature and salinity observations.

2.4. Conclusion

Understanding spatial and temporal changes in pH in association with environmental variables is essential for a sustainable management of marine systems. Hydrodynamic and biogeochemical processes in coastal estuaries change rapidly from minutes to days, triggering acidification in the system (Xu et al., 2017; Wright-Fairbanks et al., 2020). Those sudden changes often cannot be resolved through sampling and analyses of discrete water samples. The automated real-time observation of carbonate chemistry dynamics with sensors like LOC offer a potentially substantial improvement in that regard. While the performances of the LOC sensor for high-resolution spectrophotometric pH measurements has been demonstrated in surface waters of shelf seas with salinities above 24 (Rérolle et al., 2018; Yin et al., 2021), this is the first report on deployments of the sensor in dynamic estuarine waters (S<20).

Our study shows the effects of respiration and wind-driven mixing of water masses leading to consecutive impacts on the carbonate chemistry of the Kiel Fjord. The presented in situ data from observations conducted within a period of six weeks in two seasons (summer and autumn) showed the suitability of the LOC pH sensor for revealing the strong dynamics in highly dynamic estuarine waters on a fine temporal scale. The applicability of the sensor is broad, it was integrated on a Seaglider (iRobot/Kongsberg) (Possenti et al., 2021), on an Autosub Long Range AUV (Yin et al., 2021), and on an ROV (Monk et al., 2021). The unique depth rating (6000 m), low power and reagent consumption, low cost, high portability, and ease to use without calibration for long-term monitoring make the LOC sensor a good choice for autonomous pH observations on various monitoring platforms. Work is currently underway for integration of the LOC pH sensor on other AUVs (pers. comm. Socratis Loucaides). The measurement frequency (~8 min) is the main weakness of the sensor when deployed on fast-moving and profiling platforms such as gliders and floats. Future works should focus on optimizing the measurement duration of the sensor to achieve better performance on such platforms.

Author Contributions

Münevver Nehir performed the laboratory and field work, statistical analysis and data visualization. Mario Esposito performed the installation of the sensors on the deployment platform. **Münevver Nehir** wrote the first draft of the manuscript. All authors contributed to the article and approved the submitted version.

Funding

This study was supported by funding to Eric P. Achterberg from the European Union's Horizon 2020 Research and Innovation Program under the AtlantOS program, grant agreement No. 633211. Eric P. Achterberg acknowledges funding for the OCEANSensor project as part of the MARTERA Programme and financed by the German Federal Ministry of Economic Affairs and Energy (BMWi; Funding Agreement 03SX459A).

Acknowledgements

The authors thank Class Hiebenthal and Christian Begler for providing the post-processed pCO_2 data of the CONTROS HydroC CO_2 sensor, and Björn Buchholz for assistance with the deployment facility on a floating pontoon at GEOMAR Helmholtz Centre for Ocean Research (Kiel, Germany). The authors also thank Maria Martinez-Cabanas and Felix Geissler for their assistance with the collection of discrete water samples.

3. Improved Calibration and Data Processing Procedures of OPUS Optical Sensor for High-Resolution In Situ Monitoring of Nitrate in Seawater

Münevver Nehir[1,*], Mario Esposito[1], Christian Begler[1], Carsten Frank[2], Oliver Zielinski[3], Eric P. Achterberg[1,*]

Published in *Frontiers in Marine Science*

DOI: 10.3389/fmars.2021.663800

[1] GEOMAR Helmholtz Centre for Ocean Research Kiel, Wischhofstr. 1-3, 24148 Kiel, Germany

[2] Hamburg University of Applied Sciences, Faculty of Life Sciences, Ulmenliet 20, 21033 Hamburg, Germany

[3] Center for Marine Sensors, Institute for Chemistry and Biology of the Marine Environment, University of Oldenburg, 26382 Wilhelmshaven, Germany

Abstract

Nitrate, an essential nutrient for primary production in natural waters, is optically detectable in the ultraviolet spectral region of 217-240 nm, with no chemical reagents required. Optical nitrate sensors allow monitoring at high temporal and spatial resolutions that are difficult to achieve with traditional approaches involving collection of discrete water samples followed by wet-chemical laboratory analysis. The optical nitrate measurements are however subject to matrix interferences in seawater, including bromide, at the spectral range of interest. Significant progress has been made over the last ten years in improving data quality for seawater nitrate analysis using the ISUS and SUNA (Seabird Scientific, USA) optical sensors. Standardization of sensor calibration and data processing procedures are important for ensuring comparability of marine nitrate data reported in different studies. Here, we improved the calibration and data processing of the OPUS sensor (TriOS GmbH., Germany), and tested five OPUS sensors simultaneously deployed under identical conditions in the laboratory in terms of inter-sensor similarities and differences. We also improved the sampling interval of the OPUS to 3 s in a continuous mode by a custom-build controller, which facilitates the integration of the sensor into autonomous profiling systems. Real-time, high-resolution, *in situ* measurements were conducted through (1) underway surface measurements in the southeastern North Sea and (2) depth profiles on a CTD frame in the tropical Atlantic Ocean. The nitrate data computed from the optical measurements of the sensor agreed with data from discrete water samples analysed via conventional wet-chemical methods. This work demonstrates that the OPUS sensor, with improved calibration and data processing procedures, allows *in situ* quantification of nitrate concentrations in dynamic coastal waters and the open ocean, with an accuracy better than ~2 µM and short-term precision of 0.4 µM NO_3^-. The OPUS has a unique depth rating of 6,000 m and is a good and cost-effective nitrate sensor for the research community.

Keywords: nitrate, optical sensor, data processing, *in situ* spectrophotometer, ultraviolet spectrophotometer, autonomous monitoring.

3.1. Introduction

Nitrogen is a crucial nutrient for the functioning of all living organisms. The principal form of fixed dissolved inorganic nitrogen in marine waters is nitrate (NO_3^-), which is identified as one of the Essential Ocean Variables by the Global Ocean Observing System community (EOVs). Nitrate is utilised by microorganisms, including phytoplankton, for primary production and thereby facilitates ocean uptake of atmospheric carbon dioxide (Wong et al., 2002). The availability of nitrate leads to direct and indirect effects on marine ecosystem health: it can limit primary productivity when depleted (Kristiansen et al., 2001) and cause eutrophication when supplied at high levels (Beusekom, 2018). Traditionally, the determination of nitrate in marine waters has been undertaken through collection of discrete water samples, preservation if required, and laboratory analysis using wet-chemical techniques (Grasshoff et al., 1983; Becker et al., 2019). Infrequent sampling intervals result in missing episodic and transient events that lead to important temporal and spatial variations in nitrate concentrations (Prien, 2007; Pidcock et al., 2010). High-frequency *in situ* observations on autonomous platforms are therefore required to capture the variability in nitrate concentrations, overcome risks of sample contamination and degradation, and reduce high sampling/analysis costs as well as relatively long analysis times.

Over the past 30 years, advances in technology and analytical chemistry have allowed the development of submersible analysers for marine waters that can provide *in situ* NO_3^- measurements. To date, wet-chemical colorimetric analyzers and ultraviolet (UV) optical sensor technologies are available for marine water applications (Daniel et al., 2020). These sensors allow autonomous NO_3^- analysis in marine waters on various platforms and at enhanced temporal and spatial resolution. However, their performance can be limited by analytical, biological, optical, and physical factors, including detection limit, reagent stability, biofouling, power consumption and depth range. Wet-chemical analyzers such as the WIZ probe (Systea, Italy, Vuillemin

and Sanfilippo, 2010) and Lab-on-Chip sensor (NOC, UK, Beaton et al., 2012) have a measurement frequency of ca. 15 min, a limit of detection of 0.025 µM NO_3^-, require chemical reagents, and have moving components (pumps, syringes). The analytical principle is based on the colorimetric reaction method where NO_3^- is determined using the Griess assay with a copperized cadmium column, and *in situ* calibration using standard solutions (Beaton et al., 2012). The optical sensors are based on direct spectrophotometric NO_3^- determinations in the UV wavelength region, as NO_3^- has a strong spectral signature up to 240 nm (Johnson and Coletti, 2002), and these sensors have a high measurement frequency (up to 1 Hz) (Johnson and Coletti, 2002, Johnson et al., 2006). UV optical sensors offer several advantages over colorimetric sensors, as they are not prone to issues associated with degradation of chemical reagents, fragile microfluidic components and chemical waste. The optical sensors are small in size (portable), light in weight (typically 2 kg), capable of operating on the order of seconds, and have the potential to be used for long-term deployments because of their low power consumption ($\leq$ 8 W).

Initial sea trials of the first version of a UV optical NO_3^- sensor measuring at six wavelengths; 205, 220, 235, 250, 265 and 280 nm were reported over 20 years ago (Finch et al., 1998). High-resolution and long-term hyperspectral oceanic measurements of NO_3^- have been reported using a ISUS sensor (Seabird Scientific, USA) that employed a 256-pixel array detector with a spectral range of 200-400 nm (Johnson and Coletti, 2002). Thereafter various hyperspectral UV optical sensors such as the SUNA (Seabird Scientific, USA), NITRATAX plus sc (Hach Lange GmbH, Germany), S::CAN Spectro::lyser (S::CAN Messtechnik GmbH, Austria), ProPS and OPUS (TriOS GmbH, Germany), have become commercially available with a range of detectors, light sources, and path lengths. These sensors have been used in a range of environmental applications, including monitoring of wastewaters (Rieger et al., 2008), freshwaters (Pellerin et al., 2012), coastal waters (Zielinski et al., 2011;

Frank et al., 2014), and the open ocean (Johnson, 2010; Pasqueron de Fommervault et al., 2015).

The ISUS sensor has been mounted on autonomous profiling Biogeochemical Argo floats in the ocean, generating high-frequency (1 measurement per second) long-term (>2.5 years) NO_3^- data (Johnson et al., 2013). Recently, the OPUS was deployed in brackish waters of the Baltic Sea in which the potential use of the sensor on a Conductivity-Temperature-Depth *(*CTD) rosette sampler (1 measurement per 20 s) was demonstrated (Meyer et al., 2018). Bittig et al. (Bittig et al., 2019) deployed the OPUS on an experimental Biogeochemical Argo float, however to date, results and data evaluations have not been published. The ISUS and OPUS sensors differ in their light sources; ISUS utilizes a deuterium and OPUS a xenon lamp. Each lamp has a specific thermal and spectral stability, brightness, spectral output and lifetime (Finch et al., 1998). A xenon flash lamp has a relatively large-scale spectral variability at the wavelength range of interest (<240 nm) compared to deuterium (Johnson and Coletti, 2002), and an advantageously longer lifetime (a xenon lamp ~2,000-3,000 h and deuterium ~1,000 h) (Pellerin et al., 2013).

The UV absorption spectrum of seawater is determined by bromide (Br^-) and NO_3^-, and to a lesser extent by the optically measurable fraction of coloured dissolved organic matter (CDOM) (Ogura and Hanya, 1966; Johnson and Coletti, 2002). The accuracy of NO_3^- data output using UV optical sensors depends on how well interfering substances are compensated for (Frank et al., 2014). Several data post-processing algorithms have been proposed (Sakamoto et al., 2009, 2017a; Frank et al., 2014; Pasqueron de Fommervault et al., 2015; Johnson et al., 2018; Meyer et al., 2018) to correct for the chemical interferences and compute NO_3^- concentrations from raw spectral data. The need to compensate for Br^- interferences in optical nitrate analysis in seawater using temperature and salinity dependence of absorption has been reported (Zielinski et al., 2007). Over 10 years, various oceanographic studies with the ISUS or SUNA sensors commonly used a temperature-corrected salinity

subtracted (TCSS) algorithm introduced by Sakamoto et al. (Sakamoto et al., 2009, 2017a). Calculation strategies of nitrate concentrations from *in situ* optical nitrate sensors, such as the ProPS, were further improved for turbid marine environments (Zielinski et al., 2011).

To date, the OPUS is lacking a reliable sensor calibration and data processing approach for marine waters. There is nevertheless a need to standardize the handling of the raw spectral data of the sensors in order to ensure the output data is comparable among different studies that cover different regions of the global ocean (Daniel et al., 2020).

The objective of this study was to improve the calibration and data processing procedures of the OPUS for high-resolution *in situ* monitoring of NO_3^- in marine waters. When handling raw spectral data in different ways, such as using the LSA-like calibration (from the manufacturer, see **Table 3.1**) or SUNA-like calibration (Johnson et al., 2018) and distinct approaches to compensate for Br^- and CDOM related interference in measurements, and comparing the output NO_3^- data might lead to inconsistencies. This study presents a new application of the TCSS approach (introduced by Sakamoto et al. (2009) for the ISUS/SUNA) for the OPUS sensor. For this, sensor-specific parameters related to the calibration and Br^--compensation algorithm were derived through a series of laboratory experiments. Besides, a total of five OPUS sensors were deployed simultaneously under controlled laboratory conditions, and similarities and differences between the sensors were evaluated. The temporal resolution of NO_3^- measurements by the OPUS sensor has been increased to 3 s by a newly developed controller, achieving high-resolution monitoring on moving marine platforms such as CTD profilers. OPUS sensors were further employed during research expeditions in the (1) southeastern North Sea, and (2) tropical Atlantic Ocean. Reference discrete water samples were collected in the field and analysed in the laboratory using conventional wet-chemical methods for validation purposes.

Table 3.1: Characteristics of the OPUS sensor, as provided by the manufacturer (Operating Instructions, TriOS GmbH).

Parameters	**OPUS**
Optical Features	
Light source	Xenon flash lamp
Lamp lifetime	~ 2,000-3,000 h (Pellerin et al., 2013)
Detector	High-end miniature spectrophotometer
Wavelength range	200-360 nm
Wavelength resolution	0.8 nm/pixel
Physical Features	
Instrument housing material	Stainless steel or titanium
Dimensions (Length x Diameter)	470 mm x 48 mm (with 10 mm path) for stainless steel (regular) 511 mm x 59 mm (with 10 mm path) for titanium (deep-sea)
Sample path lengths	0.3, 1, 2, 5, 10, 20, 50 mm
Weight in air	~ 3 kg for stainless steel and 2 kg for titanium (regular) ~ 4 kg for titanium (deep-sea)
Sampling frequency	3 s (with a custom-build controller) 30 s (regular)
Accuracy	±5 % + 0.01 of readings
Precision	0.4 µM
Maximum depth ratings	300 m for stainless steel 6,000 m for titanium
Power consumption	≤8 W
Input voltage	12 V
Communication interface	Ethernet, RS-232 or RS-485 (Modbus-RTU)
Operation temperature range	2-40°C
Internal data storage capacity	2 GB
Data Processing Features	
Manufacturer calibration file	Reference sum spectra of the LSA group
System configuration and data download	TriOS web-based interface

3.2. Materials and Methods

3.2.1. Instrument Description

The OPUS nitrate sensor is portable, small in size, and light in weight (**Table 3.1**). The device utilizes a xenon flash lamp, a reference diode and a 256-channel high-end miniature spectrophotometer. Briefly, a xenon flash lamp is directed through an optical path with the sample, and the intensity of light passing through the sample is recorded by the spectrophotometer over a wavelength (λ) range of 200 to 360 nm with an integration time of 256 ms. A reference diode monitors the intensity of the light source. A schematic diagram of the sensor is shown in **Figure 3.1**. All components are housed in a single stainless steel or titanium pressure case.

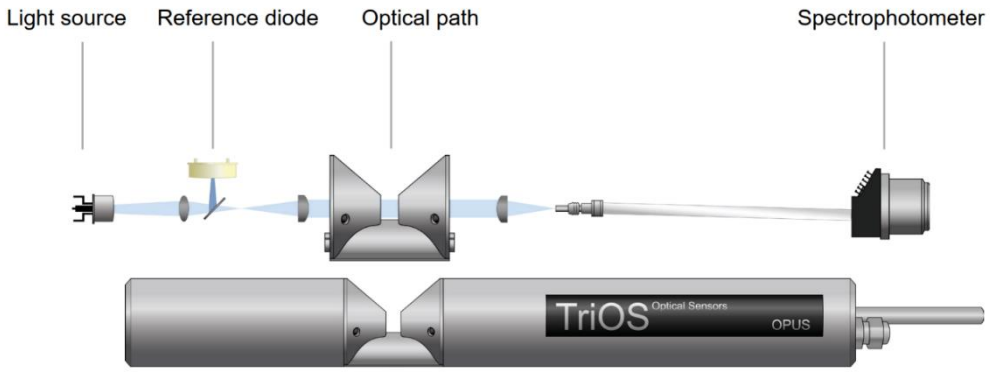

Figure 3.1: Schematic of the OPUS sensor unit (courtesy of TriOS GmbH).

The regular (factory setting) sampling interval of the OPUS is 30 s when set to operate in a continuous sampling mode. This is suitable for stationary deployments, but not when deploying the sensor on gliders or autonomous profiler systems, such as CTD frames with a vertical profiling speed of 1 m/s. We developed at GEOMAR a ATMega128 (Atmel Corporation) based controller that triggers the raw spectral (dark and light) measurements of the OPUS via a Modbus-RTU protocol. The wiring diagram of the controller is provided in **Figure 3.2**. Electrical power to the OPUS and controller is provided through an auxiliary port of the CTD system. Measurements are conducted every 3 s at a defined sequence, with measurements of ten times light followed by one-time dark spectrum. A drift up to 60 s per day in the internal clock of the OPUS was observed. To eliminate this, the controller is set to autonomously synchronize time during each dark measurement. Another important feature of the controller is that it provides backup power for a few seconds to allow the OPUS to finish its measurement in case of power loss.

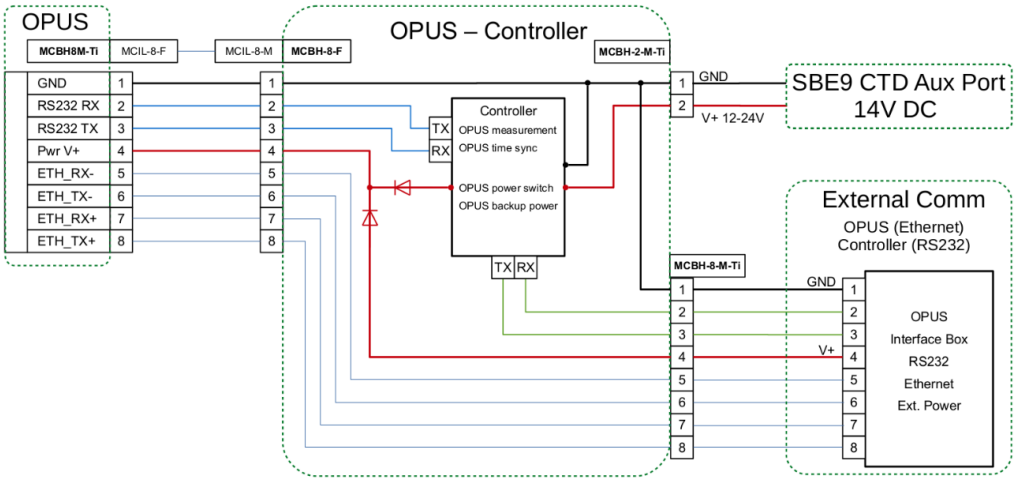

Figure 3.2: Schematic of the wiring diagram of the controller for enhancing measurement frequency of OPUS sensor.

3.2.2. Laboratory Tests

The first part of this study consisted of experiments carried out under controlled laboratory conditions. Freshly dispensed deionized water (Milli-Q, resistance ≥18 MΩ cm^{-1}, Merck Millipore) was used to prepare calibration solutions of 840 µM Br^-, with and without 40 µM NO_3^-, and additional 1, 2, 4, 7, 10, 20 and 60 µM NO_3^- solutions, from stock solutions of 1,000 µM KBr (Fisher Scientific ACS reagent grade) and 1,000 µM KNO_3 (Merck Millipore ACS reagent grade). The calibration solutions were kept in acid cleaned (1 M HCl) glass bottles. A total of five OPUS sensors, all with 10 mm optical path length, were utilized in parallel under conditions described below. We assigned them consecutive numbers, i.e., OPUS1 to OPUS5, to which we refer throughout the study. The OPUS1 sensor was a deep-sea version and others were shallow water versions (see **Table 3.1**). The sensors were fully immersed in a thermally insulated glass container (15 L) sequentially filled with calibration solutions in a deionized water medium. The container was connected via Teflon tubing (I.D. 50 mm) to a water bath (7 L, Julabo GmbH) to control the temperature and circulate the solution (**Figure 3.3**). A custom-made polystyrene lid was placed on top to avoid contamination and heat exchange, and keep the sensors at the same height in the container. Prior to the measurements, optical windows of the sensors were cleaned with a few drops of acetone and wipes (Kimtech) followed by rinsing with deionized water. The surface of the sensors, volume of the container, water bath and tubings contacting sample were all rinsed at least three times with deionized water at the beginning of the setup and between changes of solutions. First, freshly dispensed deionized water was carefully poured into the container, care was taken to avoid the formation of air bubbles on the optical paths, and a reference spectrum was recorded. Then, UV spectra of two calibration solutions were measured as a function of temperature. The water bath temperature was set to a total of 4 fixed temperatures between 5 and 20°C, and enough time was given to stabilize the sample temperature. The OPUS1 sensor was set to 3 s while the other sensors were set to 30 s for about 30 min (as only one controller for higher frequency analysis was available at

the time of the experiment). The calibration solutions were used to assess the temperature effect and to derive molar extinction coefficients - the strength of chemical species to absorb light at a particular wavelength - of Br^- ($\varepsilon_{Br^-,cal}$) and NO_3^- ($\varepsilon_{NO_3^-,cal}$).

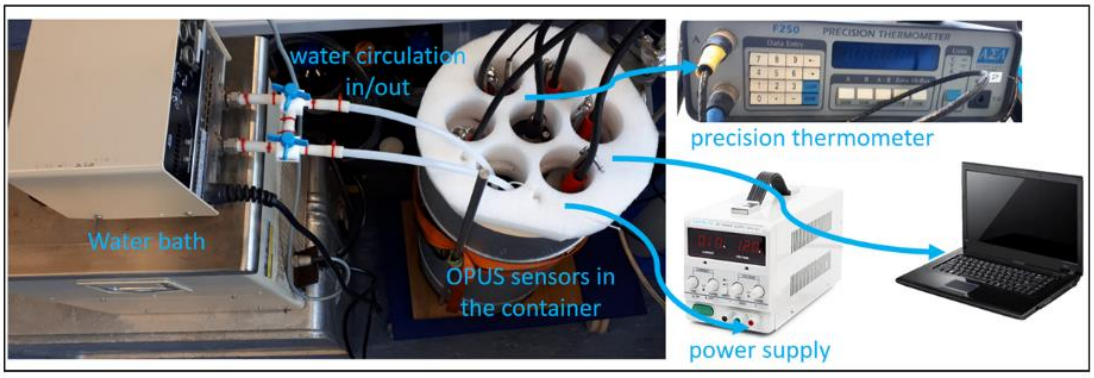

Figure 3.3: The laboratory setup for testing of OPUS sensors.

Laboratory measurements were conducted in 840 µM Br^-, which is equivalent to Br^- concentrations in seawater with salinity 35. Other chemical interferences from small seawater components are expected to be low below 240 nm, and therefore these were not the subject of this study. The laboratory experiments were conducted in a freshly dispensed deionized water medium in order to have full control over the measurements and avoid potential matrix effects. The concentration unit of µM reported throughout the study indicates micromoles per liter ($\mu mol \cdot L^{-1}$).

During the experiments, *in situ* temperature in the container was measured with a Kelvimat® 4323 thermometer (Burster Präzisionsmesstechnik GmbH) equipped with a Pt100 temperature probe, which has an accuracy of ± 0.01°C. The sensors, temperature probe of the precision thermometer and external computer were all synchronized via coordinated universal time (UTC). The TriOS web-based software was used to operate the sensors and download the internally recorded data. Power (12 V) was supplied to sensors by an external benchtop power supply.

3.2.3. Field Campaigns

One of the OPUS (OPUS1) sensor was employed in the southeastern North Sea on April 16-17, 2019 during the Sternfahrt-1 MOSES research expedition onboard RV Littorina. The expedition track from Büsum to Helgoland and return, and the location of the German Bight are shown in **Figure 3.4**. Helgoland is located about 60 km away from the German coast and Elbe River mouth (Ey et al., 2017), and the coastal waters are a mixture of riverine and saline North Sea waters. Prior to the deployment, the sensor housing was cleaned with deionized water, and the OPUS was fully immersed in a cylinder filled with deionized water to update the waterbased spectrum. The sensor was fully immersed in a test tank (volume of 160 L) placed on deck of the vessel and was continuously supplied with surface water (from 2 m depth) at a flow rate of 80 L/min. UV spectral measurements of seawater were recorded with the OPUS at a 1-min sampling interval. *In situ* salinity and temperature values were recorded at 1-min interval using a CTD system (Seabird SBE 37-SMS-ODO), placed in the test tank. Discrete water samples were collected periodically at about 30 min intervals to validate the sensor measurements. For this, the water samples from the test tank were filtered (0.45 µm pore size PES filter, Fisher Scientific) and stored in 50 ml polypropylene tubes (Jet Biofil) that had been acid cleaned (1 M HCl). The tubes were rinsed three times with filtered seawater prior to collection. Samples were stored at -20°C, and analysed within one month at GEOMAR using an autoanalyser (Seal QuAAtro) with standard wet-chemical colorimetric techniques (Becker et al., 2019).

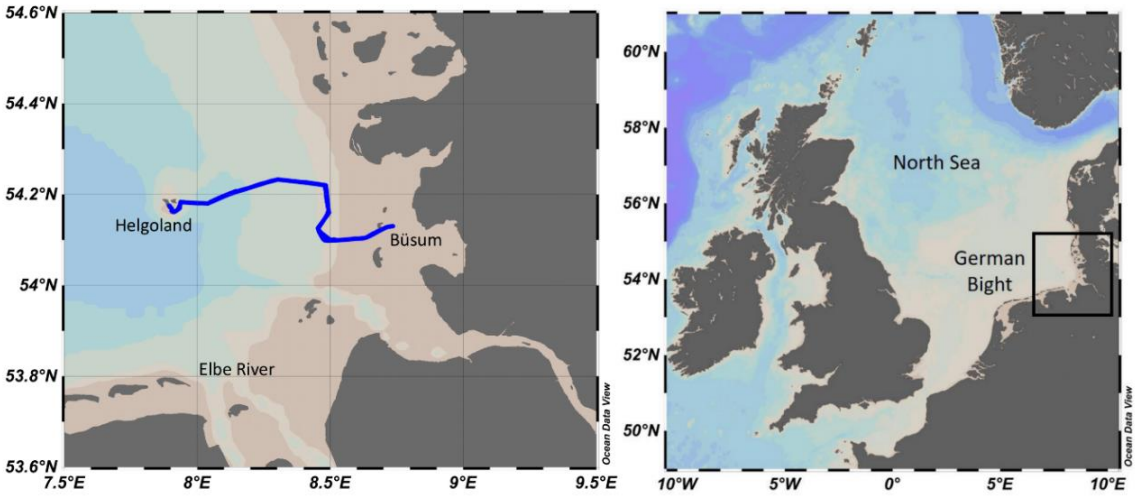

Figure 3.4: Left panel: Map showing the expedition track of the RV Littorina during the Sternfahrt-1 in the southeastern North Sea, from Büsum to Helgoland. Right panel: North Sea and location of the German Bight.

The second field test took place in the tropical Atlantic Ocean, where the OPUS1 was mounted on a CTD frame and deployed on a cast down to 4,000 m depth (00°00.00'S, 30°00.00'W, October 15, 2019, CTD71, M158 research cruise, R/V *Meteor*). Ancillary data (including dissolved oxygen and inorganic nutrients; NO_3^-, nitrite, silicate and phosphate) were obtained at various depths during the deployment.

3.3. Results and Discussion

3.3.1. Assessment of the Effect of Temperature on Bromide Absorbance

Br^- is a conservative component of seawater with a concentration of ca. 840 µM at salinity 35 (Morris and Riley, 1966). The strength of absorbance for both Br^- and NO_3^- ions are closely related and overlap in the lower UV region, as indicated in a figure of their molar extinction coefficients versus wavelength (**Figure 3.5**). Spectral discrimination of these ions is required to accurately compute NO_3^- concentrations. For this, the spectral region between 217 and 240 nm, where NO_3^- is dominant, is used (Zielinski et al., 2011).

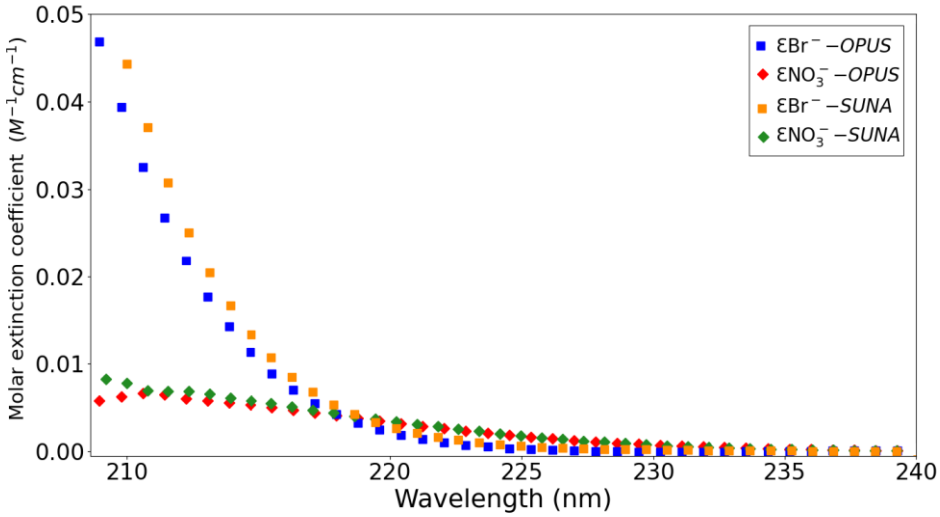

Figure 3.5: Molar extinction coefficient (ε) values of 840 µM Br^- and 40 µM NO_3^- at wavelengths from 210 to 240 nm at 20°C from OPUS and SUNA-specific (Johnson et al., 2018) calibration files.

Br^- absorption is temperature-dependent as it occurs through a charge transfer process; the rate of charge transfer varies with ambient temperature (Jortner et al., 1964; Sakamoto et al., 2009). On the other hand, NO_3^- absorbance is independent of temperature due to the fact that it occurs within the molecule through π to π* transition process (Mack and Bolton, 1999). During the laboratory tests, we used the calibration solutions to assess the temperature effect on Br^- absorbance. The absorbance of the 840 µM Br^- solution

exponentially increased with an increasing temperature (**Figure 3.6a**), and gradually decreased with increasing wavelength (**Figure 3.6b**).

The relative change in absorbance with respect to temperature remained constant for 840 µM Br^- with and without 40 µM NO_3^-, there was no additional temperature effect on absorbance due to the presence of NO_3^- ions (not shown here). It should be noted here that the 840 µM Br^- and 40 µM NO_3^- do not necessarily reflect the real seawater conditions, and the exact *in situ* levels of both constituents might vary in time and space, nevertheless this can be computed using the algorithm (see Eqn. 4 in section 3.3.2.).

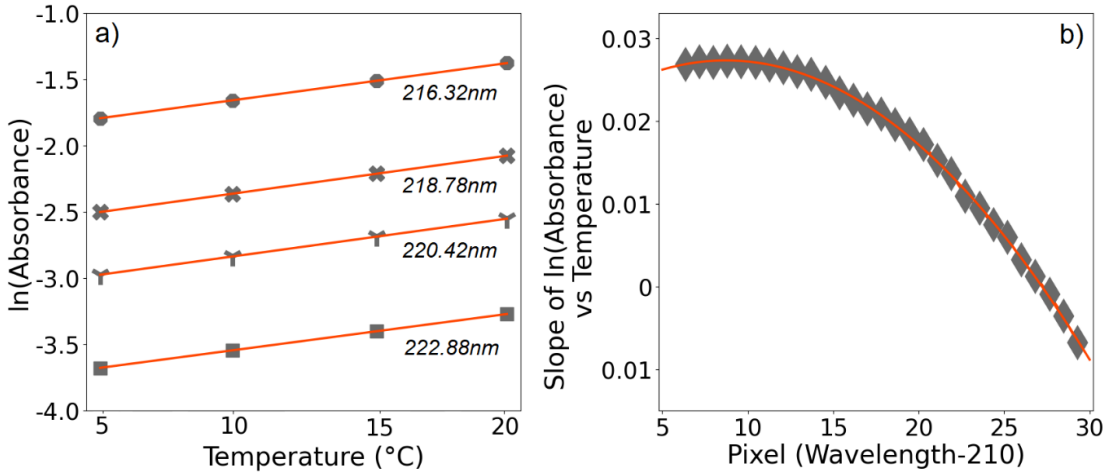

Figure 3.6: a) The ln(absorbance) values of 840 µM Br^- solution plotted vs. temperature of the solution; at 216.32, 218.78, 220.42 and 222.88 nm. Data are shown in grey. The solid red lines refer to the linear regression (r^2=0.99), with y=0.0277x-1.9323, y=0.0284x-2.6439, y=0.0282x-3.1159 and y=0.0271x-3.8135, respectively. b) The slope of ln(absorbance) vs. temperature plotted vs. pixel. In here, pixel refers to wavelength-210, within 216 and 239 nm. The solid red line presents the third order polynomial fit and has y=1e-07x^3–9e-05x^2+0.0016x+0.0212, r^2 =0.99.

The raw spectral data of the calibration solutions were processed using the procedure described in section 3.3.2. An example spectral area attributed to NO_3^- after data processing is shown in **Figure 3.7**.

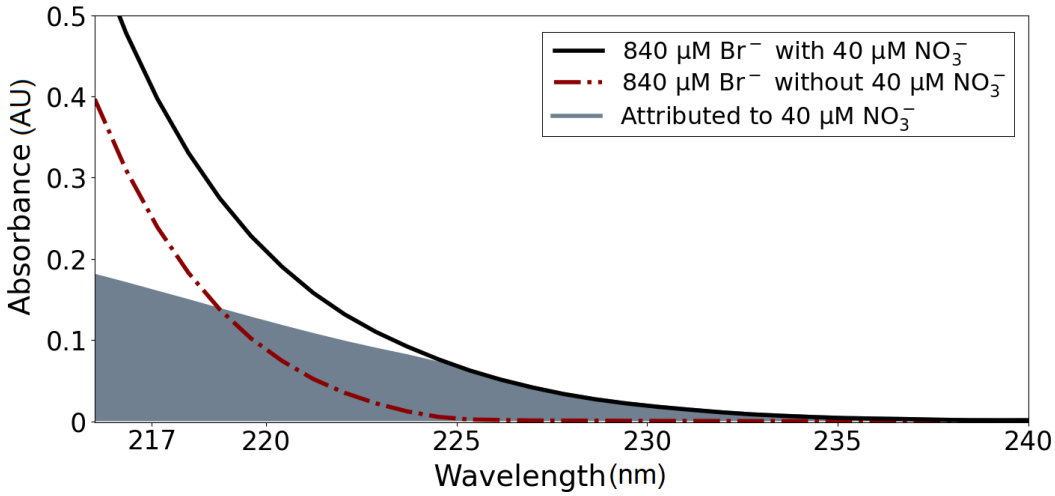

Figure 3.7: The spectral signature of calibration solutions at 20°C. The grey filled area is attributed to absorbance due to NO_3^-.

3.3.2. Data Processing Procedure for OPUS

Raw spectral data of the OPUS was processed by taking potential lamp degradation, Br^- interference and CDOM-baseline effect into account prior to calculating NO_3^- concentrations. The lamp degradation was taken into account during calculation by recording detector intensities in deionized water before and after each deployment (see section 3.3.3.). We determined OPUS-specific molar extinction coefficients for Br^- and NO_3^- prior to data processing and developed a new algorithm (Eqn. 4) for the compensation of Br^- interferences. Data processing procedure is outlined as follows;

1. Calculation of the measured absorbance of a sample in the UV spectral region of interest between 200 and 260 nm: The absorbance ($A_{measured}$) is logarithmically related to a transmitted light intensity according to Beer-Lambert's law:

$$A_{measured} = -\log\left(\frac{I_\lambda - I_D}{I_{\lambda_0} - I_D}\right) \qquad (Eqn.\ 1)$$

where I_λ refers to detector intensity for the sample and I_{λ_0} is the detector intensity for deionized water. I_D is the dark current that is periodically recorded

by the spectrophotometer when the light source is off. I_D was subtracted from each spectrum to eliminate internal noise (Nehir et al., 2019) before the data is used. λ is the wavelength (nm).

2. Calibration Coefficients: It should be noted here that the calibration coefficients were determined in the laboratory following the procedures described in section 3.2.2, and a sensor-specific calibration file was produced prior to the deployments. This file includes wavelength, $\varepsilon_{Br^-,cal}$, $\varepsilon_{NO_3^-,cal}$, calibration temperature and reference intensity recorded in deionized water (Johnson et al., 2018). $\varepsilon_{Br^-,cal}$ and $\varepsilon_{NO_3^-,cal}$ were determined from a linear relationship between absorbance and concentration of the substance according to Beer-Lambert's Law:

$$\varepsilon_{Br^-,cal} = \frac{A_{Br^-\,cal}}{S_{cal} \cdot l} \qquad at\ T_{cal} \qquad (Eqn.2)$$

$$\varepsilon_{NO_3^-,cal} = \frac{A_{NO_3^-\,cal}}{c_{NO_3^-,cal} \cdot l} \qquad (Eqn.3)$$

where $A_{Br^-\,cal}$ is the absorbance of Br^- calibration solution, and is normalized to a salinity of 35 (for [Br^-]=840 µM). $A_{\ NO_3^-\,cal}$ is the absorbance of NO_3^- calibration solution, and $c_{NO_3^-,cal}$ is the concentration of the solution, 40 µM. T_{cal} is the temperature value of the solution during the calibration, 20°C. The units for $\varepsilon_{Br^-,cal}$ and $\varepsilon_{NO_3^-,cal}$ are $M^{-1}\ cm^{-1}$, which are dependent on the path length of the sensor. In this study, the optical path length (*l*) of the OPUS sensors was 10 mm.

3. Br^- related interference compensation: In order to compensate Br^- interference in optical nitrate measurements, we determined the relative change in 840 µM Br^- absorbance –salinity normalized to 35– with respect to wavelength and temperature under controlled laboratory conditions. From this, we developed a new algorithm (Eqn. 4), based on **Figure 3.6**, to calculate Br^- absorbance theoretically at *in situ* conditions. Previously, it was shown that pressure also has an effect on the Br^- absorbance of about -2% (Pasqueron de Fommervault et al., 2015) or -2.6% per 1,000 dbar (Sakamoto et al., 2017a). This correction can be described as follows:

$$\varepsilon_{Br-,in\ situ} = \varepsilon_{Br-,cal} \cdot \exp\left(a \cdot w^3 + b \cdot w^2 + c \cdot w + d \cdot (T_{in\ situ} - T_{cal})\right) \quad (Eqn.\ 4)$$

$$\varepsilon_{Br-,in\ situ} = \varepsilon_{Br-,in\ situ} \cdot (1 - (P_F \cdot P_{in\ situ}/1000)) \quad (Eqn.\ 5)$$

$$A_{in\ situ\ Br^-} = \varepsilon_{Br-,in\ situ} \cdot S_{in\ situ} \quad (Eqn.\ 6)$$

$$A_{residual} = A_{measured} - A_{in\ situ\ Br^-} \quad (Eqn.\ 7)$$

where *w* refers to wavelength minus 210, a wavelength offset (*wo*) value of 210. It was used for scaling purposes, and is a tuneable parameter (Pasqueron de Fommervault et al., 2015; Johnson et al., 2018). $\varepsilon_{Br-,in\ situ}$ is the molar extinction coefficients of Br^- at the *in situ* temperature ($T_{in\ situ}$, °C). The parameters a, b, c and d are regression parameters of 1e-07, -9e-05, 0.0016 and 0.0212, respectively. The parameters were obtained by fitting the 'slope of absorbance of the Br^- calibration solution versus *in situ* temperature' to 'wavelengths from 216 to 239 nm' (**Figure 3.6**) to the third order polynomial function. $P_{in\ situ}$ and $S_{in\ situ}$ refer to the *in situ* pressure (dbar) and salinity values, respectively. P_F refers to a pressure factor of 0.026. $A_{in\ situ\ Br^-}$ (*in situ* Br- absorbance) was then subtracted from $A_{measured}$, and $A_{residual}$ (remaining absorbance) was then used to fit NO_3^- and CDOM.

Although, in theory one method for the bromide-temperature relationship (calibration and fit coefficient) should be valid for all sensors, our results demonstrate that in practice the optical differences among each device (lamp, spectrometer, etc.) can have an impact on measurement quality. New fitting (Eqn. 4) and calibration coefficients (**Figure 3.5**) were introduced for the OPUS sensor, whilst the overall procedure and handling of the raw spectral data followed the well-developed approaches from the literature.

4. CDOM-baseline correction and NO_3^- quantification: The absorbance due to CDOM, also termed as yellow substances (Frank et al., 2014), often occurs at wavelengths above 240 nm, with a maxima near 260 nm, through electron transition between lone pairs or π-electrons (Guenther et al., 2001; Stedmon and Nelson, 2015). So far, linear (Sakamoto et al., 2009; Zielinski et al., 2011) and quadratic (Johnson and Coletti, 2002) mathematical functions have been proposed for the compensation of this interference, at wavelengths between 240

and 260 nm, based on the shape of the observed absorbance spectra. There appears no obvious difference between a linear and quadratic model, as both approaches are based on rough estimations of CDOM-related absorption spectrum (Frank et al 2014).

The concentrations and characteristics of CDOM are highly variable in natural waters with complex origins. Therefore, the preparation of an artificial solution under laboratory conditions is not ideal to compensate for CDOM interference. In this study, $A_{residual}$ was attributed to absorbance due to NO_3^- ($A_{NO_3^-}$) and CDOM-baseline (A_{CDOM}). Each spectrum was corrected for the contribution of A_{CDOM} (Eqn. 9), which was determined from the linear regression between absorbance and wavelength (see Fig 8):

$$A_{CDOM} = i + j \cdot \lambda \qquad (Eqn. 8)$$

where i and j refer to baseline intercept and slope, respectively, and are adjustable parameters based on measured *in situ* absorbance.

The final determination of NO_3^- concentration ($c_{NO_3^-}$) was done by solving a linear regression using a singular value decomposition method at approximately 30 pixels (0.8 nm/pixel) within 217 and 240 nm. This can be expressed as:

$$A_{residual} = \begin{bmatrix} 1 & \lambda_1 & \varepsilon_{NO_3^-,cal,\lambda_1} \\ 1 & \lambda_2 & \varepsilon_{NO_3^-,cal,\lambda_2} \\ & & \dots \\ 1 & \lambda_{n-1} & \varepsilon_{NO_3^-,cal,\lambda_{n-1}} \\ 1 & \lambda_n & \varepsilon_{NO_3^-,cal,\lambda_n} \end{bmatrix} \cdot \begin{pmatrix} i \\ j \\ c_{NO_3^-} \end{pmatrix} \qquad (Eqn. 9)$$

where λ_1 to λ_n refers to wavelengths between 217 and 240 nm where the Br^- and CDOM interferences are lowest (Sakamoto et al., 2009; Zielinski et al., 2011). $\varepsilon_{NO_3^-,cal,\lambda_1}$ is shown in Eqn. 3.

Figure 3.8 illustrates an example of the spectral signature of CDOM on optical NO_3^- determination.

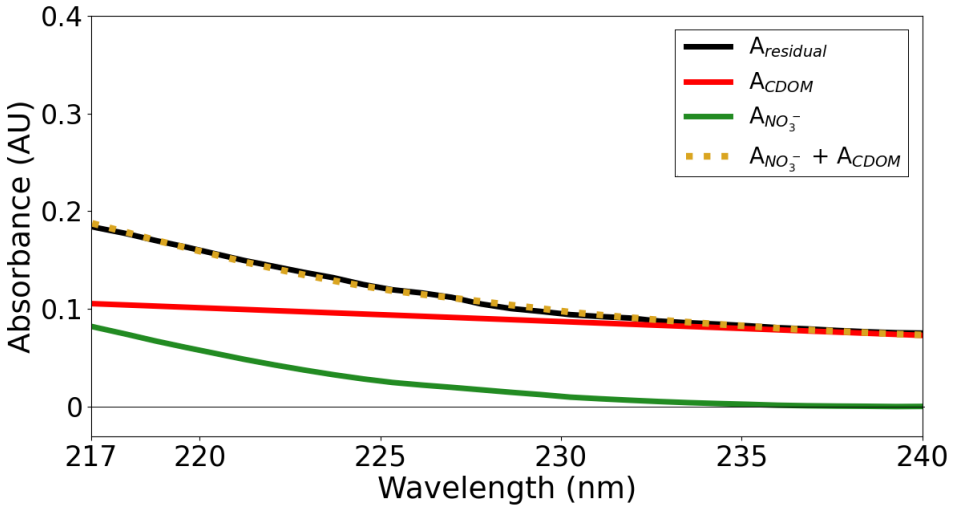

Figure 3.8: The spectral signature of CDOM and NO_3^- within 217 and 240 nm (cNO_3^-=19.4 µM, S=35.4, T=13.6°C at 211 m depth during the M158-CTD71 deployment).

All data processing described and statistical analysis throughout the study were undertaken in MATLAB (Mathworks, R2018a) software. A mat file with the complete data from each recorded activity was produced. The code ingests the OPUS raw data file, calibration file, CTD file, and all equations above, and is available at https://github.com/uv-nitr/proc.

3.3.3. Calibration of OPUS Sensors: Inter-Sensor Comparison

The OPUS sensor is factory calibrated at the manufacturer and a sum absorption spectra of expected seawater constituents at pre-defined concentrations is saved in the unit (see **Table 3.1**, Operating Instructions, TriOS GmbH). The other optical nitrate sensors, such as the ISUS and SUNA, are calibrated to derive the molar extinction coefficients of Br^- and NO_3^- (Sea-Bird Coastal SUNA, 2015). Recent documentation of these sensor's calibration, and data processing can be found in the "Processing Bio-Argo nitrate concentration at the DAC Level" and "8th BGC-Argo Meeting" reports (Johnson et al., 2018; Claustre and Johnson, 2019). In this work, the factory calibration of the OPUS was ignored and individual calibration coefficients were obtained (Eqns. 2-3).

The correlation for ε_{Br_cal} and $\varepsilon_{NO_3\_cal}$ for about 75 pixels between 200 and 260 nm was examined using the Pearson correlation matrix and coefficients. A correlation coefficient value close to 1.0 indicates an excellent correlation between the respective datasets. Results indicated that the OPUS sensors were in excellent agreement (≥0.95) for both ε_{Br_cal} and $\varepsilon_{NO_3\_cal}$ values (**Figure 3.9**), and are greater than 0.99 within 217 and 240 nm (for about 30 pixels, wavelength range of the NO_3^- fit, not shown here). The sensors wavelength values vary about 4-5 nm at the same pixel. Improvement of technical characteristics such as wavelength registrations, gratings in CCDs were beyond the scope of the study. However, the reason for not identical correlation coefficients for the same pixels can be explained not in absolute value of sensors but in sensitivity. For example, the OPUS1 sensor had a spectral resolution of 0.82 nm while the OPUS2 had 0.79 nm resulting in better sensitivity.

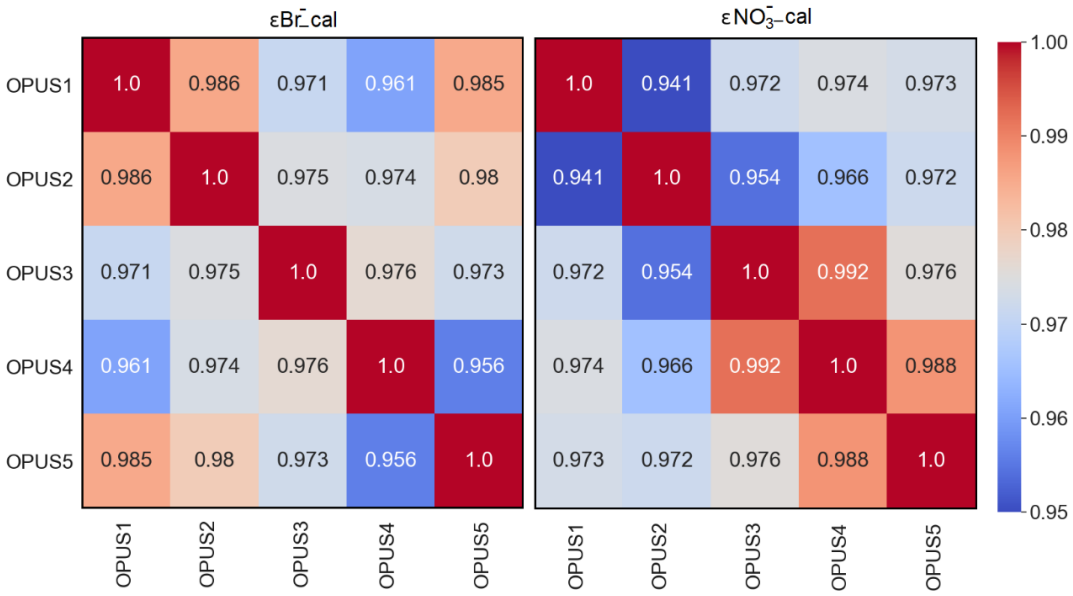

Figure 3.9: The Pearson's correlation matrix for ε_{Br_cal} and $\varepsilon_{NO_3\_cal}$ for the OPUS sensors used.

Results from the laboratory a test of the OPUS sensors under identical conditions, and using a series of 1, 2, 4, 7, 10, 20, 40, 60 µM NO_3^- solutions in 840 µM Br^- medium, are presented in terms of NO_3^- bias across the five sensors. The NO_3^- concentration obtained from the OPUS sensor with the mean and laboratory analysis of discrete water samples was fit to a linear regression (r^2= 0.99, **Figure 3.10**). The standard deviation of NO_3^- for the lowest concentration was ~0.64 µM, which translates to a limit of detection of ca. 2 µM NO_3^- (three times the standard deviation of blank). An accuracy of better than ~2 µM NO_3^- was determined from the residuals of the regression, while overall precision of NO_3^- sensor measurements was ~0.4 µM, from the consecutive measurements of the identical sample.

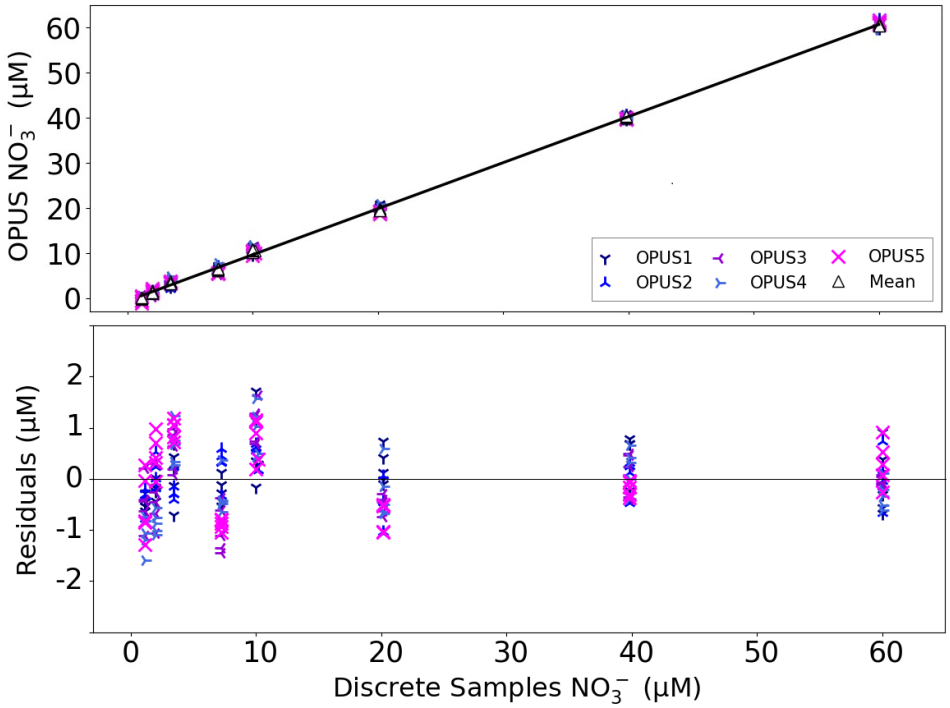

Figure 3.10: Linear regression fit (solid line) between mean NO_3^- concentrations from the OPUS sensors versus laboratory analysis of discrete water samples (y=1.021x-0.641, r^2 = 0.99). The residuals of the regression for each sensor were within ±2 µM NO_3^-.

An additional parameter used for the calibration is the reference spectrum recorded for deionized water medium using the OPUS sensors. The detector intensity of the sensor in deionized water was used in Eqn. 1. Each OPUS sensor has a unique spectral output of its xenon flash lamp in the UV range (**Figure 3.11**). The design of the OPUS is comparable to the SUNA, except for the xenon lamp. Although this is not an OPUS vs SUNA comparison study, a demonstration of reference intensity (recorded in deionized water) values of the xenon lamp based OPUS sensor and deuterium lamp based SUNA sensor are shown in **Figure 3.11**. Please note here that the data presented for the SUNA sensor was adopted from the literature (Johnson et al., 2018). Observing large differences in spectral output of xenon and deuterium lamps raised concerns regarding the need to derive OPUS specific coefficients. Therefore, it is important that the true performance of each specific OPUS sensor is verified in the laboratory following well-established guidelines used for other optical nitrate sensors, because the varying registrations, resolutions, and flash lamp spectra (i.e., ε values) are specific to each sensor. As this sensor-specific calibration is currently not available from the manufacturer, the five units were compared in the laboratory.

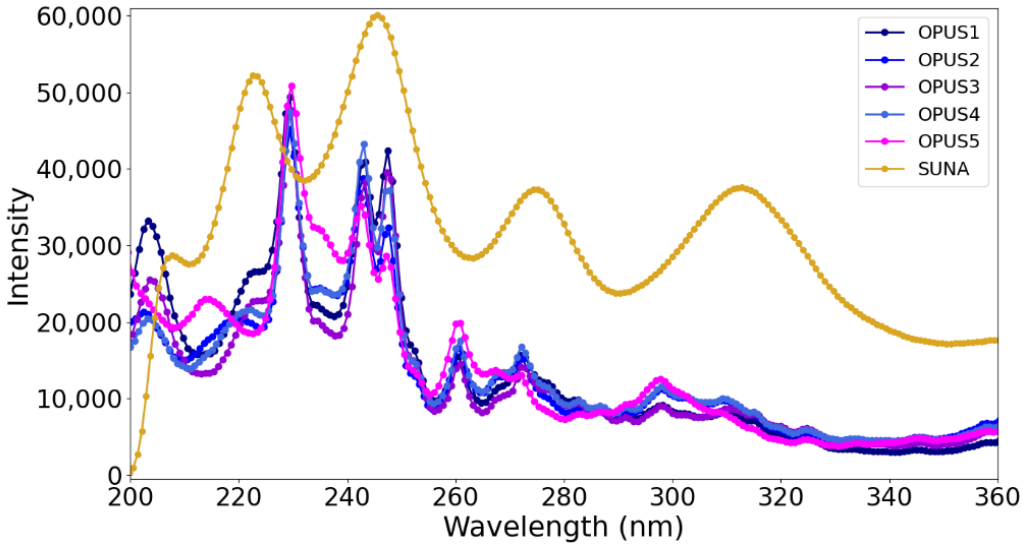

Figure 3.11: The detector intensity of the optical nitrate sensors in deionized water at all wavelengths.

The five OPUS sensors are not identical in terms of their reference spectrum as each unit has a unique compact spectrometer and wavelength registration. In addition, the sensors are not identical in terms of their age (some were several years old and others several months). The reference spectrum needs to be updated periodically (before and after each deployment) for each individual unit to minimize potential sensor drift due to aging of the lamp or obstacles in the optical path (Pellerin et al., 2013) and ensuring sensor stability over time.

3.3.4. Field Deployments

The second part of this study focused on the validation of the NO_3^- computational algorithm for the OPUS. Real-time *in situ* measurements were undertaken with the OPUS1 and CTD sensors during the Sternfahrt-1 MOSES expedition in the North Sea, where the influence of the outflow plume of the Elbe River is pronounced (Voynova et al., 2017). Temporal trends in surface water variables such as temperature, salinity and NO_3^- were determined along the cruise track. The Elbe system is subject to short-term dynamic extreme events such as heatwaves and heavy rainfall which significantly affect the waters of the southern North Sea (Voynova et al., 2017; Chegini et al., 2020). A total of 730 measurements were performed by the OPUS sensor during the 2 days cruise period. The time series of NO_3^-, temperature and salinity are shown in **Figure 3.12**. The NO_3^- values ranged between 24.6-70.9 µM on the first day (**Figure 3.12A**), and 14.2-60.7 µM on the second day (**Figure 3.12B**). Temperature ranged between 7.22 and 8.34°C, and salinity between 24.09 and 31.66.

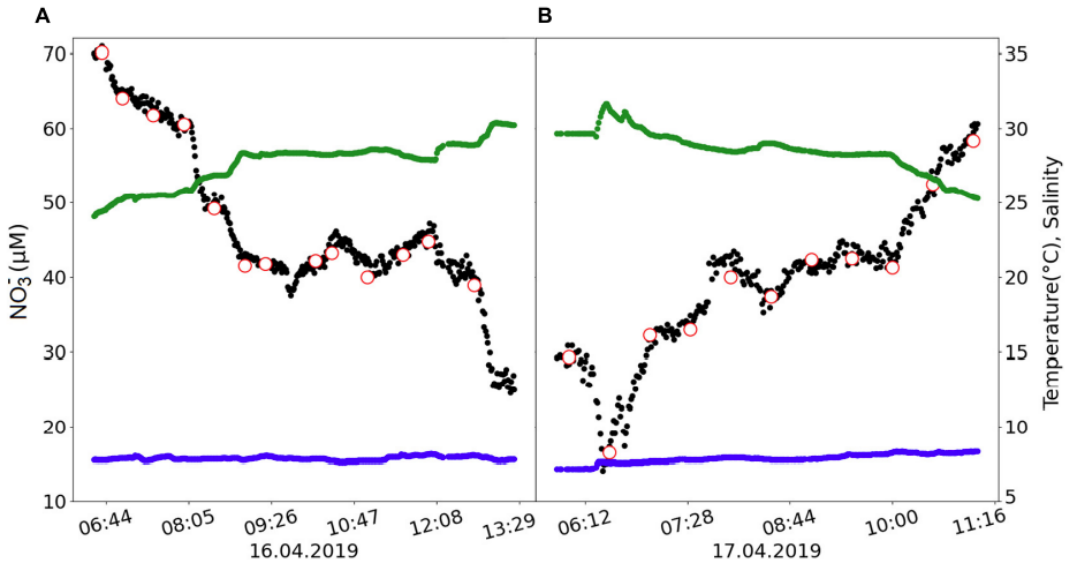

Figure 3.12: Time series of NO_3^- (µM), temperature (°C) and salinity during the Sternfahrt-1 expedition on (A) the first day sailing from Büsum to Helgoland, and (B) the second day sailing from Helgoland to Büsum. Black dots refer to the post-processed OPUS NO_3^- data output, and red circles are the NO_3^- concentrations of the discrete water samples analyzed in the laboratory by a wet-chemical analyzer. Blue and green dots indicate the *in situ* temperature and salinity of the sample, respectively.

The high variability in NO_3^- concentrations over short time scales during the approximately 6-h transects can be attributed to dynamic interactions between the waters of the North Sea and the Elbe River, with additional mixing through tidal actions. Enhanced salinity levels (towards 32) away from the coast and Elbe River coincided with lower NO_3^- concentrations (14.2 µM; **Figure 3.13**) and indicates a dilution of the nitrate-rich Elbe waters with lower NO_3^- North Sea waters. Our values agreed with NO_3^- values reported for the southern North Sea area; ≥50 µM near Elbe river (Voynova et al., 2017; Sanders et al., 2018) and ≤40 µM near Helgoland (Ey et al., 2017) in spring.

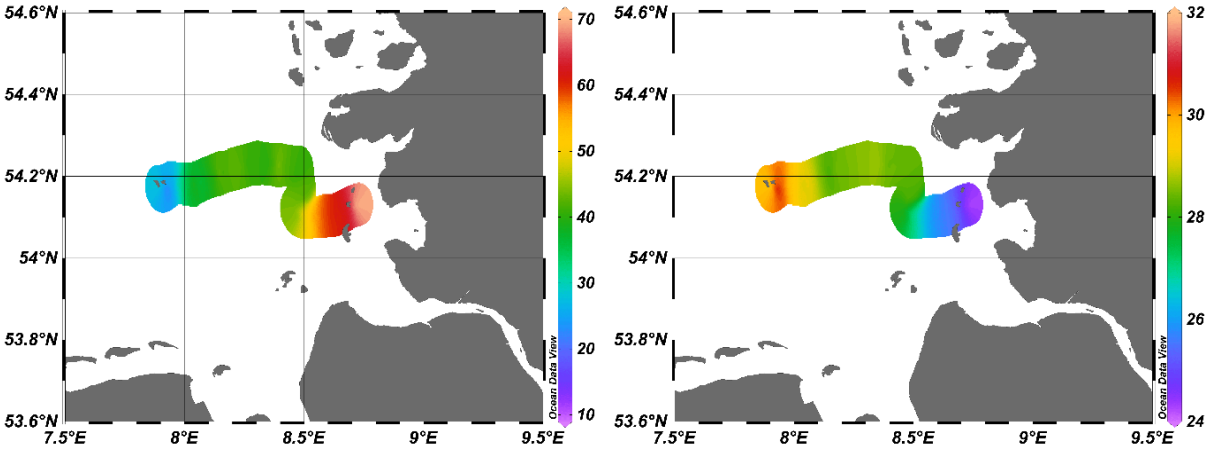

Figure 3.13: Distributions of surface NO_3^- concentrations (µM) obtained using the OPUS sensor (left panel) and surface salinity values recorded by the CTD (right panel) during the Sternfahrt-1 expedition. Colour bars represent the levels of NO_3^- (left) and salinity (right) data.

A deep ocean field demonstration took place during the M158 research expedition in the tropical Atlantic Ocean in October 2019. The OPUS was mounted on a CTD frame and deployed with a vertical profiling speed of 1 m/s, which results in a vertical resolution of 2-3 m. The data presented here refers to the CTD71 deep cast deployment in which the OPUS sensor generated a total of 2,667 measurements (once every 3 s). A total of 13 discrete water samples were collected through closure of Niskin water samplers at various depths during the deployment.

Vertical profiles of (1) NO_3^- concentrations derived from post-processing of the OPUS data with the OPUS coefficients (section 3.3.2) and SUNA coefficients (TCSS algorithm and ε_{Br_cal}, $\varepsilon_{NO_3\_cal}$ values from Sakamoto et al., 2009; Johnson et al., 2018) and discrete water samples analyzed in the laboratory, (2) temperature, salinity, and (3) ancillary data (phosphate, silicate and dissolved oxygen) are presented in **Figure 3.14**. The OPUS data were obtained during the upcast and downcast profiles, whilst discrete water samples were collected only during the upcast profile. The OPUS NO_3^- data presented in **Figure 3.14** is

independent of an offset correction (i.e., adding the NO_3^- bias determined in surface waters to the rest of the data) and averaging. The mean and standard deviation of 18 replicate measurements at the shallowest depth of this cast (27 m) is 0.16±0.67 µM NO_3^-, and 18 replicate measurements at the deepest depth (3,905 m) is 22.24±0.97 µM NO_3^-.

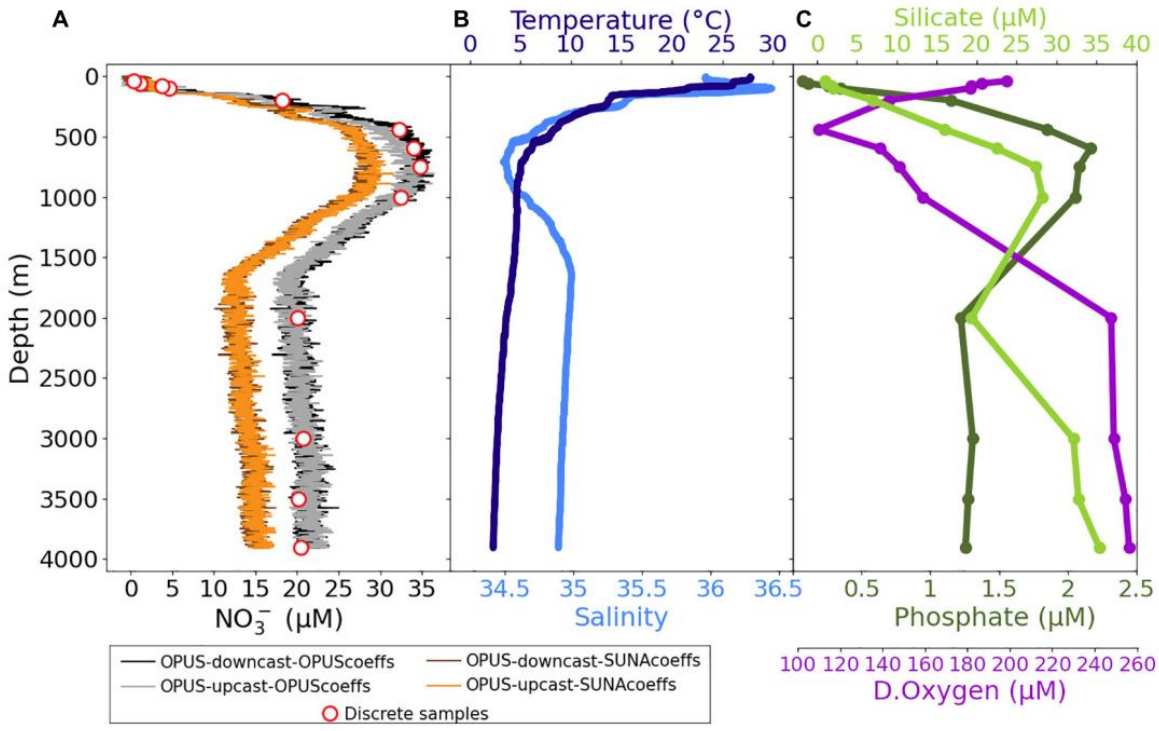

Figure 3.14: Vertical profiles of (A) NO_3^- concentrations (µM), (B) *in situ* temperature (°C) and salinity, (C) silicate (µM), phosphate (µM), and dissolved oxygen (µM) for cruise M158 cast CTD71 (00°00.00'S, 30°00.00'W). Black lines show NO_3^- values of the post-processed OPUS data obtained during the downcast, grey lines show NO_3^- values of the upcast profile, and red circles are for the discrete water samples analysed in the laboratory by the wet chemistry-based method. Brown and orange lines are for the NO_3^- values of the post-processed OPUS data with the SUNA coefficients (Johnson et al., 2018).

Temperature values ranged between 2.3°C and 27.7°C, salinity between 34.4 and 36.4, characteristic of the hydrographic situation in the water column of the tropical Atlantic. The observed silicate values were between 1.02 and 35.3 µM,

phosphate were from 0.07 to 2.17 µM, and dissolved oxygen levels were from 112 to 258 µM. The NO_3^- concentrations increased with depth towards the thermocline, from below the detection limit of the sensor (2 µM) in the surface mixed layer, to 36 µM at 800 m depth and then decreasing to 20-23 µM below 2,000 m (see NOAA-NODC for literature comparison; NO_3^- concentrations in October at surface, 800 m and 4,000 m are ca. 0, 35 and 22 µM, respectively).

The sensor and discrete water samples data followed a broadly consistent pattern throughout the deployment period. Direct adoptation of SUNA-coefficients resulted in bias in NO_3^- values of ca. 6 µM (**Figure 3.14**). Results indicate that improving the calibration and data processing procedure of the OPUS by deriving specific OPUS-coefficients (Eqn. 4 and OPUS-specific calibration file) increases the reliability of the NO_3^- data when compared to discrete water samples. The time of the sampling was precisely matched to a sensor measurement. However, a bias in NO_3^- was observed below 500 m (**Figure 3.14**) and attributed to specific optical characteristics of the sensor, which can be corrected by modifying wavelength offset and pressure factor (Pasqueron de Fommervault et al., 2015).

The sensor NO_3^- data presented throughout the study was post-processed with a wavelength offset of 210 nm (*wo* in Eqn. 4), pressure factor of 0.026 (P_F in Eqn. 5) and calibration file recorded at 20°C. **Figure 3.15** shows an example of the impact of *wo* from 206 to 212, pressure factor of 0.020 (at *wo*=210), and calibration file recorded at 5°C (at *wo*=210) on the deviation of NO_3^- for the M158-CTD71 cast data. Using a lower *wo* with respect to the reference value of 210 nm results in lower NO_3^- values at temperatures below 20°C and higher NO_3^- values at temperatures above 20°C. Because our laboratory and field data are not adequate/sufficient for direct determination and quantification of the pressure dependence of Br^- spectra for the OPUS sensor, adaptation of the pressure factor of 0.020 (Pasqueron de Fommervault et al., 2015) can be advantageous to eliminate the overestimated NO_3^- at deep waters. Another

reason for the deviation in NO_3^- could be related to the sharp temperature decrease, from 27.7 to 2.3°C, over short time scales (1 h), which might have affected the lamp output. The intensity of a xenon flash lamp changes with fluctuations in ambient temperature due to the fact that the gas pressure inside the bulb is temperature dependent; at 25°C, the intensity is 100% and decreases with decreasing temperatures (Hamamatsu Photonics K.K., 2005). Determination of the stability of the lamp with respect to temperature was beyond the scope of the study; however, reference water-based spectra recorded at temperatures close to the sampled environment (i.e., 5°C) might be used for data below 500 m to minimize the dispersion.

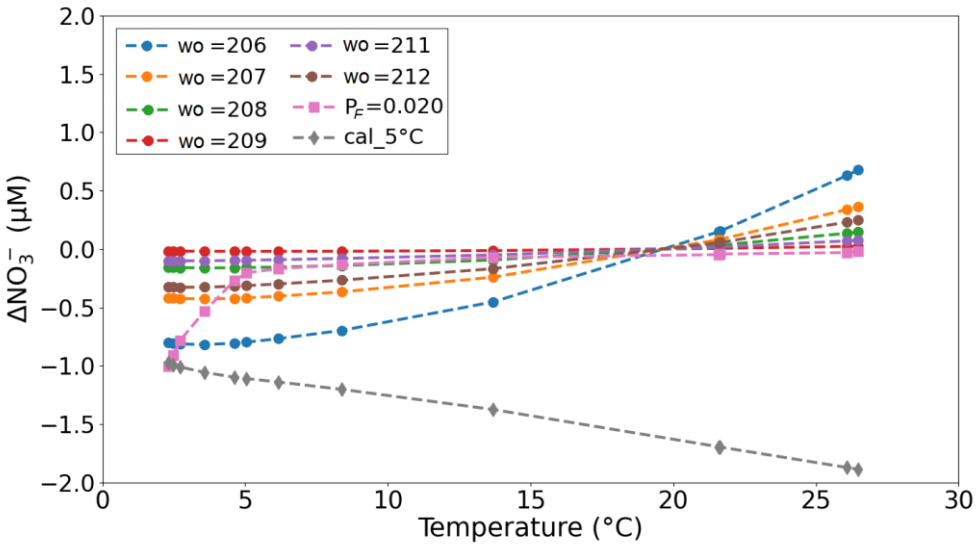

Figure 3.15: Deviation of the NO_3^- estimation with a *wo* of 210 nm, P_F of 0.026 and calibration file recorded at 20°C (OPUS-coefficients data presented in Figure 3.14A) as a function of *in situ* sample temperature. The results for P_F =0.020 and calibration at 5°C were obtained at *wo*=210.

The slight increase in sensor NO_3^- values with depth between 2,000 and 4,000 m shown in **Figure 3.14** is unlikely to be a temperature effect because at these depths the measured temperature decrease was from 3.6 to 2.3°C and a comparison of the 20 and the 5°C calibration curves in **Figure 3.15** suggests only a weak temperature effect (~0.1 µM). Thus, a pressure effect on NO_3^- bias

is more likely, and the NO_3^- values at depths are more vertical when processed with P_F=0.020 than with P_F=0.026 for the M158-CTD71 data presented (**Figure 3.16**).

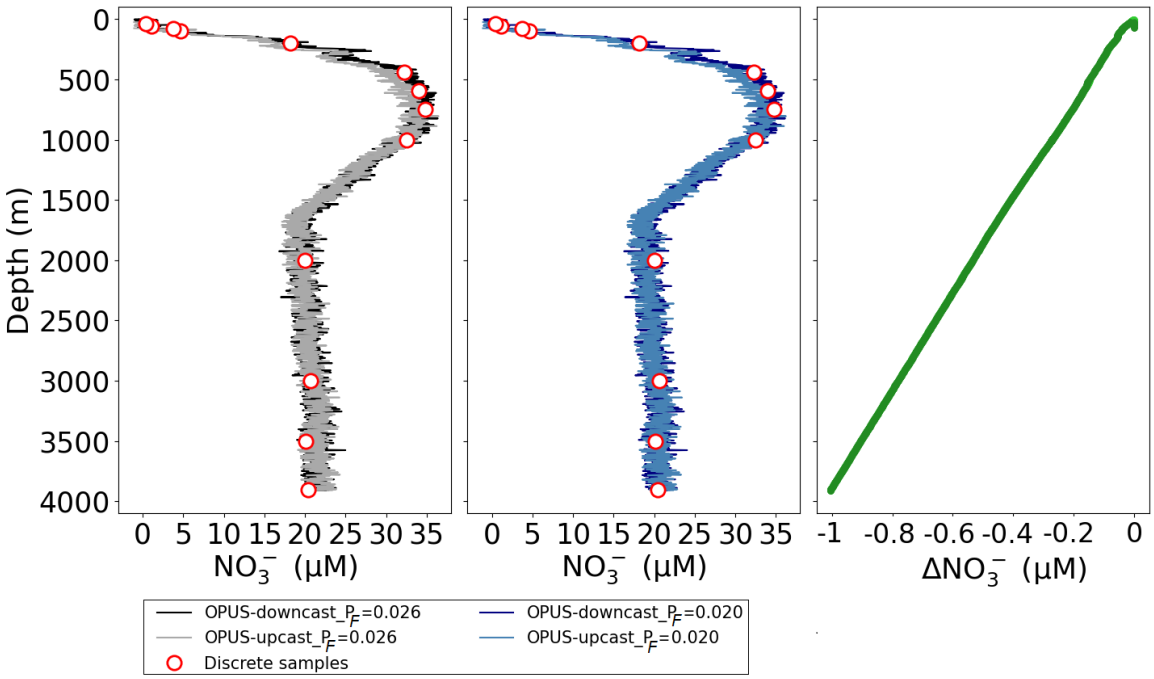

Figure 3.16: Vertical profiles of NO_3^- concentrations (µM) for cruise M158 and cast CTD71, in which the sensor data was processed using both P_F=0.026 (left panel, black and grey lines) and P_F=0.020 (middle panel, dark and light blue lines). The offset between them is presented in the right panel; ΔNO_3^- refers to the sensor NO_3^- data obtained with P_F 0.020– obtained with 0.026. Red circles are for the discrete water samples analysed in the laboratory (see also Figure 3.14).

The fast sampling interval of the sensor was advantageous for a better spatial resolution of NO_3^- concentrations in the water column compared to discrete water samples. The OPUS sensor successfully captured the NO_3^- dynamics in the water column, agreeing with the values of discrete water samples analyzed in the laboratory during both field tests; the Sternfahrt-1 and the M158. A paired t-test confirmed no statistically significant differences (p-value ≤ 0.05) between NO_3^- values obtained from the sensor and discrete samples. A linear regression

yielded y = 0.99x+0.65 (r^2=0.99, n=24) for the Sternfahrt-1 and y=0.95x+0.26, (r^2=0.99, n=13) for the M158 data (**Figure 3.17**). The residuals of the fit are shown in **Figure 3.17**. The results indicated lower residual values for the open ocean deployment when compared to the coastal water deployment, and the maximum value for both cases was <2 µM NO_3^-.

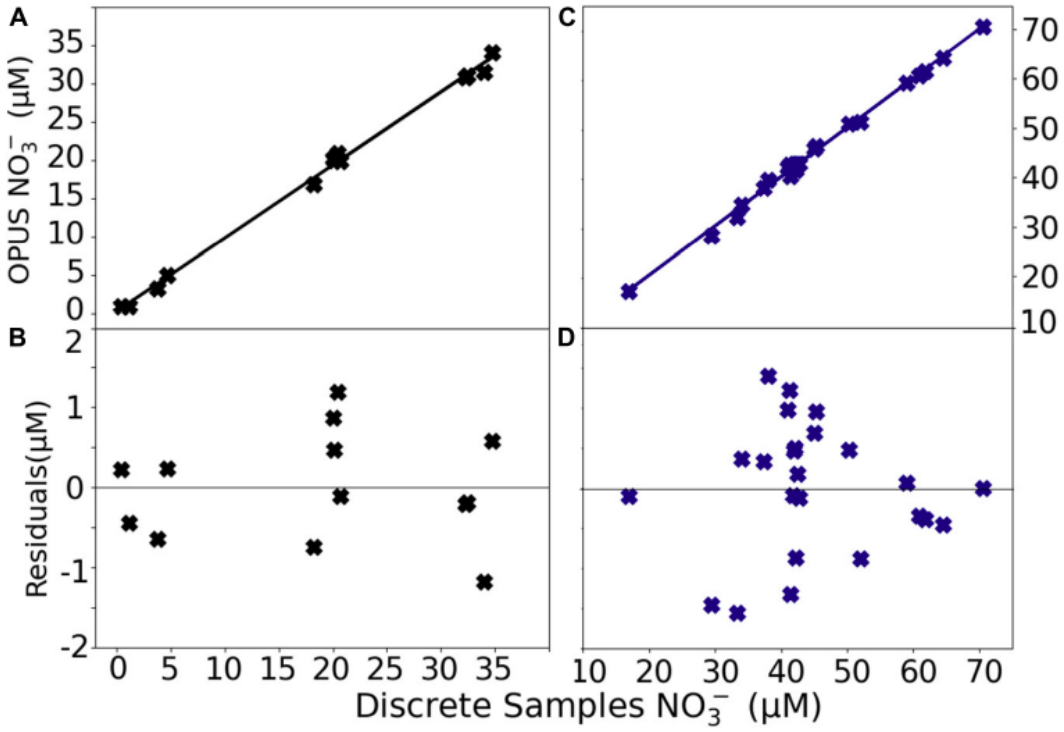

Figure 3.17: Regression plots of NO_3^- concentrations determined *in situ* with the OPUS sensor vs in the laboratory via autoanalyser and residuals of the regression for the M158 data (A and B, see also Figure 3.14) and Sternfahrt-1 data (C and D, Figure 3.12).

The coastal waters can be high in dissolved organic materials that may interfere with optical NO_3^- determination. Although the algorithm (see section 3.3.2.) performs a CDOM correction (Eqn. 8), the high and variable content of CDOM might have partly affected the nitrate outputs. We used the difference in NO_3^- concentrations between the sensor and discrete water samples versus the total absorbance in the CDOM wavelength range (240-260 nm) to check whether the

NO_3^- bias is CDOM related, but no significant relationship was found (not shown here). Time series of measured absorbance at 254 nm and at 360 nm (wavelengths outside of the NO_3^- detection range) can be used to check anomalies related to yellow substances and particles, respectively. We checked this for both deployments data presented and found stable absorbances over time below <0.5 AU at 254 and 360 nm. Further investigation on the impact of yellow substances and particles on optical nitrate measurements in regions with a high organic matter content is needed. The effect of path length, as well as CDOM, on optical NO_3^- measurements were reported in detail by Snazelle (2016). The absorbance is directly proportional to path length. Another option could indeed be the use of a 5 mm or smaller path length instead of 10 mm.

The sensor measurements at the two shallowest depths, where the NO_3^- levels are below 2 µM, can be improved by small adjustments in data processing parameters as shown in **Figure 3.15**. We would like to mention that this is the first demonstration of a deep deployment of the OPUS sensor and so the initial step for future investigations such as an OPUS-specific pressure correction factor. Pressure-dependent experiments require more sophisticated experimental setups (Sakamoto et al., 2017a).

Overall, the laboratory and field data presented throughout the study verified the success of the improvement work on calibration and data processing procedures of the OPUS.

3.4. Conclusion

This work highlights that the OPUS sensor is a useful tool to determine NO_3^- dynamics in the water column in real-time by providing high-resolution *in situ* data, and thereby provides strong advantages over traditional laboratory analysis of discrete water samples. The data processing strategies of the OPUS described in this study strongly improved the quality of the sensor's NO_3^- data output, and resulted in a comparable quality to the ISUS and SUNA sensors, with an accuracy of ~2 µM, and short-term precision of 0.4 µM NO_3^-. An inter-comparison between five OPUS sensors deployed in parallel under identical laboratory conditions showed no significant difference between the sensors. Deployment in coastal surface waters and the deep ocean demonstrated that the OPUS sensor can capture spatial variations across short spatial scales with results that were in excellent agreement with discrete water samples analysed in the laboratory. The firmware design of the OPUS sensor is not suitable for a faster sampling rate than 3 s. Although the sampling rate of 3 second translates to a vertical resolution of 2-3 m, the sensor is advantageous due to the depth range of 6,000 m and it is the deepest operating optical nitrate sensor available for the research community. Another advantage of the OPUS are the long periods between lamp replacements. The previous version of the OPUS sensor named as ProPS was using a deuterium lamp and had a lifetime of 2 years, at 20°C and 15 min sampling interval. The expected lifetime of the OPUS is above 10 years, at 20°C with 1-min sampling interval (communication from manufacturer). Besides, the cost of the OPUS sensor (in Europe, about 10-12k €) is considerably lower compared to other commercial UV nitrate sensors (i.e., SUNA about >40k €) and therefore economically more affordable, especially for EU customers. The OPUS sensor is promising for future oceanographic studies. This study provides new insights specific for the OPUS sensors in the form of an 'Ocean Best Practice' approach. Future work will focus on the assessment of the long-term performance of the OPUS on marine autonomous platforms, such as FerryBox systems and deep-sea gliders.

Author Contributions

Eric P. Achterberg and **Münevver Nehir** conceptualized the study and methodology. Christian Begler and Oliver Zielinski supported experimental tools. Christian Begler provided initial Matlab scripts and assisted in the development of the OPUS controller. Mario Esposito assisted during laboratory and field tests. **Münevver Nehir** wrote the manuscript with edits and contributions from all co-authors.

Funding

This study was supported by funding to Eric P. Achterberg from the European Union's Horizon 2020 Research and Innovation Program under the AtlantOS program, grant agreement No. 633211. Eric P. Achterberg acknowledges funding for the OCEANSensor project as part of the MARTERA Programme and financed by the German Federal Ministry of Economic Affairs and Energy (BMWi; Funding Agreement 03SX459A). Additional funding for Oliver Zielinski is acknowledged from SpectralArgo-N (BMBF; Funding Agreement 03F0825A).

Acknowledgements

We would like to thank our colleagues André Mutzberg for analyzing discrete water samples for nutrients, and Dr. Gerd Krahmann for providing the M158 raw data. We thank TriOS GmbH for their assistance in implementing high-resolution analysis mode.

4. Improving Optical Measurements: Non-Linearity Compensation of Compact Charge-Coupled Device (CCD) Spectrometers

Münevver Nehir[1] , Carsten Frank[2,3], Steffen Aßmann[3,4], Eric P. Achterberg[1,*]

Published in *Sensors*

DOI: 10.3390/s19122833

[1] GEOMAR Helmholtz Centre for Ocean Research Kiel, Wischhofstr. 1-3, 24148 Kiel, Germany

[2] Hamburg University of Applied Sciences, Faculty of Life Sciences, Ulmenliet 20, 21033 Hamburg, Germany

[3] Helmholtz Centre Geesthacht, Institute of Coastal Research, Max-Planck-Str. 1, 21502 Geesthacht, Germany

[4] Kongsberg Maritime Contros GmbH, Wischhofstr. 1, 24148 Kiel, Germany

Abstract

Charge-coupled device (CCD) spectrometers are widely used as detectors in analytical laboratory instruments and as sensors for in situ optical measurements. However, as the applications become more complex, the physical and electronic limits of the CCD spectrometers may restrict their applicability. The errors due to dark currents, temperature variations, and blooming can be readily corrected. However, a correction for uncertainty of integration time and wavelength calibration is typically lacking in most devices, and detector non-linearity may distort the signal by up to 5% for some measurements. Here, we propose a simple correction method to compensate for non-linearity errors in optical measurements where compact CCD spectrometers are used. The results indicate that the error due to the non-linearity of a spectrometer can be reduced from several hundred counts to about 40 counts if the proposed correction function is applied.

Keywords: charge-coupled device, compact spectrometer, optical measurements, spectrometer errors, non-linearity correction.

4.1. Introduction

Charge-coupled device (CCD) spectrometers are compact detectors that provide spectral information about the light that reaches the image sensor component. The devices usually consist of an entrance slit, a collimating lens, a transmission grating, a focusing mirror, a CCD line/image sensor, and some electronics. A schematic view of a CCD spectrometer is shown in **Figure 4.1**. While there are various configurations available where a reflective rather than a transmissive grating is applied, or the entrance slit is omitted and instead an aperture of a fiber bundle is used, the error sources remain the same.

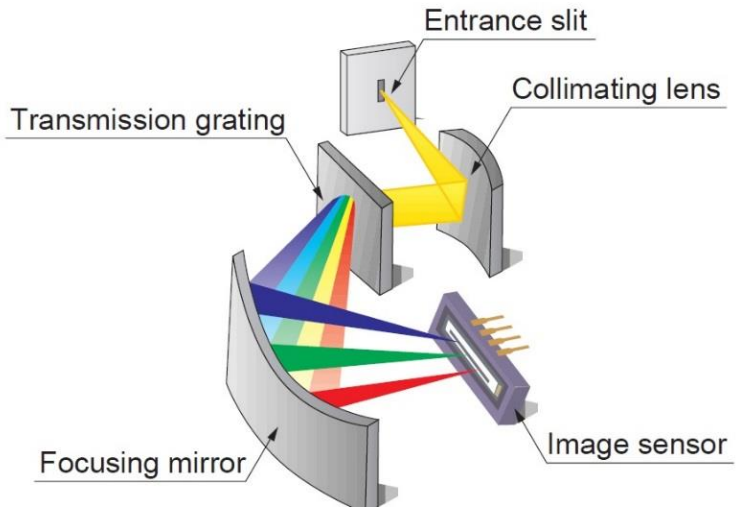

Figure 4.1: Schematic of a Hamamatsu C10082CA miniaturized spectrometer

(Hamamatsu Photonics K. K., 2017).

When using CCD spectrometers, error sources at each pixel that cause a deviation of the corresponding signal from the correct value have to be considered. The CCD spectrometers usually have a dark current, which has to be determined and subtracted from each spectrum before the data is used. For older CCD spectrometers, one has to account for blooming of super-saturated pixels (Oda et al., 1983). These errors can be readily compensated for, or are negligible for the more recent CCD sensors. Li et al. (2017) studied the effect

of temperature on the response of CCD spectrometers, and obtained a deviation of less than 1% between the measured and calculated responses at randomly selected temperatures between 5 and 40 °C. Furthermore, the non-linear behavior of the CCD line has to be considered as a significant measurement error source. Experiments have indicated that the non-linearity at an intensity of about 50,000 (of a maximum of 65,535) counts is in the range of up to 1000 counts on the intensity scale, or up to 0.04 absorption units on the absorbance scale, using a Hamamatsu C10082CA mini-spectrometer (Aßmann et al., 2011). Non-linearities in the light intensity response of CCD spectrometers greater than 10% were found in recent studies and the corresponding corrections resulted a non-linearity of less than 0.5% (Xia et al., 2015; Pulli et al., 2017); in one study a custom-designed spectrometer (Xia et al., 2015) was used and in the other an Avantes Avaspec-ULS2048L spectrometer and a StellarNet Blue-Wave spectrometer (Pulli et al., 2017) were used. To the best of our knowledge, Ocean Optics Inc. is the only supplier that provides non-linearity correction software (OOINLCorrect, Ocean Optics Inc., Dunedin, FA, USA) for their CCD spectrometers, which provides linearities >99.8% (OceanOptics).

Other miniature spectrometers are equipped with a photodiode detector array (PDA) instead of a CCD detector and offer some advantages. There are different semiconductor technologies used to build PDAs, one is the complementary metal-oxide-semiconductor field-effect transistors (CMOS) technology. These PDAs are generally more linear compared to CCD detectors and have a wider dynamic range. However, they are less sensitive and therefore less common (CCD, PDA Detector Definitions) and were not tested in this work.

Charge-coupled device-based spectrometers are used in a variety of applications, including spectrophotometric flow injection analysis using only one or two wavelengths for simple absorption measurements (Neves et al., 2008), multiple wavelengths for multi-component determination (Yuanqian et

al., 2002), and for the direct determination of a certain analyte in the context of a complex background signal (Frank et al., 2014).

Specific fields of these applications are the determination of dissolved phosphate (Neves et al., 2008), dissolved trace metals (Yuanqian et al., 2002), pH (Aßmann et al., 2011; Rérolle et al., 2012; Müller et al., 2018), and hyper-spectral determination of nitrate, bromide, and colored dissolved organic matter (Zielinski et al., 2011; Frank et al., 2014) in seawater.

Another important application field of CCD spectrometers is in space instrumentation, where they are used to explore astronomical objects (Pereyra et al., 2016). The CCD spectrometers are also used in meteorology, for example, to detect changes in spectral UV irradiance due to changes in the thickness of the ozone layer (Seckmeyer et al., 2001). While these applications are very different, the challenges with the spectrometers are similar (Seckmeyer et al., 2010).

Further uses of CCD are in imaging applications combined with a single photon camera and a multichannel detector, which is straightforward and significantly improves the performance of time-correlated photon counting (Canet-Ferrer et al., 2019).

Other optical sensors that use a CCD-detector but rely on a different optical setup may also be affected by the non-linear response of the CCD line. One example is a method that allows time resolved measurements based on a stroboscopic light source and a revolving grating (Smalley et al., 2018).

Compared with the conventional bench-top spectrophotometers, CCD spectrometers have the advantages of being low-cost, small in size, light in weight, robust, and suitable for high-speed data assimilation (milli-seconds) with a steady performance (Davenport et al., 2015; Huang et al., 2018).

In this study, we describe and evaluate a non-linearity correction method for a CCD spectrometer that only depends on the intensity of the signal and is independent of integration time and wavelength. We aim to broaden the applicability of the CCD spectrometers. Our findings are illustrated for each pixel using a Hamamatsu C10082CA mini-spectrometer.

4.2. Theory

4.2.1. Design of a CCD Spectrometer

In this study, a Hamamatsu S10420-1106-01 CCD line was connected via an amplifier to a 16-bit analog-to-digital converter (ADC). The ADC was connected to a microcontroller that controlled the measurement parameters (e.g., integration time) and transmitted data to the interface via USB and/or RS232. **Figure 4.2** shows a simple schema, which is nevertheless a good approximation of most of the possible circuit variations.

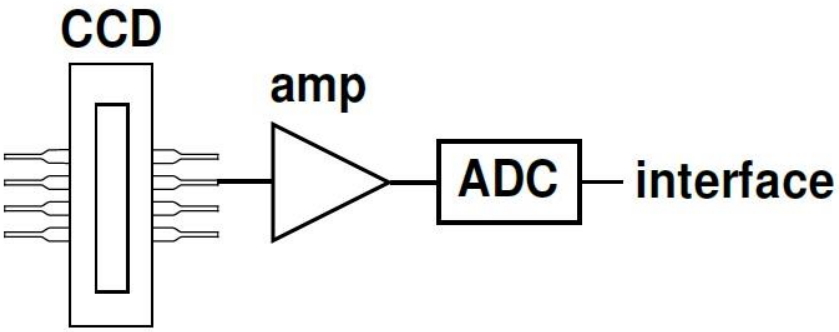

Figure 4.2: Simplified diagram of the basic internal circuit that connects the charge-coupled device (CCD) line with the interface (RS232 or USB) of the computer. The CCD line is connected via an amplifier (amp) with the analog-to-digital converter (ADC). The latter is either part of a microcontroller or connected to a microcontroller that communicates with the computer.

4.2.2. Signal Composition

There are several error sources for CCD spectrometers, which can also be found in common monochromator-based desktop instruments. We describe the sources below.

ADC Offset

An ADC device is used to convert an analog to a digital signal, and its resolution is determined by the number of bits (e.g., a 16-bit device has 2^{16} discrete digital output values). An ADC offset (w_{ADC}) is used to shift the lowest possible signal into the range of voltages that can be converted by the ADC (**Figure 4.3**). It can be expected that a similar limitation exists at the upper end of the sensitivity range, called 'headspace' in **Figure 4.3**. This, however, is inconsequential for the presented approach as the working range is defined up to 50,000 counts.

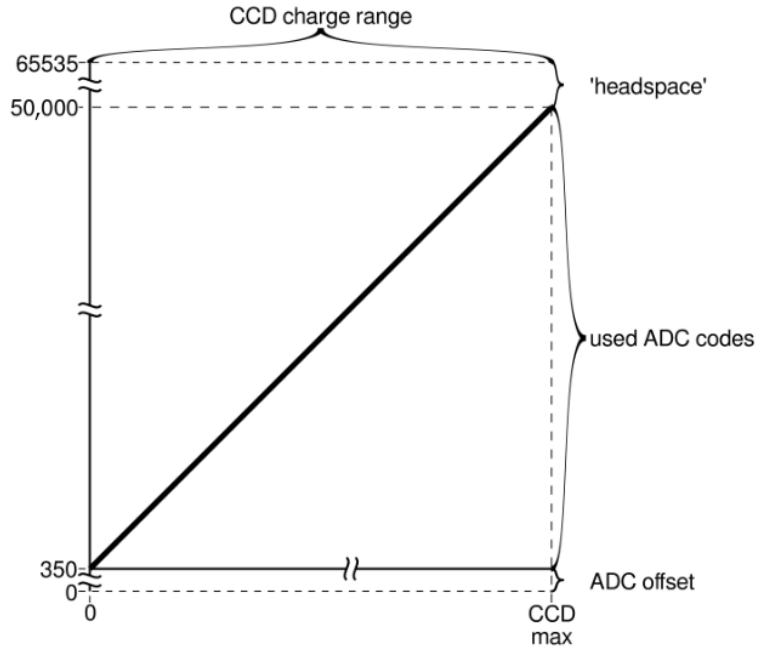

Figure 4.3: Diagram showing how all possible CCD output values (after amplification; X-axis) are mapped onto the value range of the analog-to-digital converter (ADC; Y-axis). As the zero value of the CCD (and the amplifier) may vary with time, temperature, and/or other factors, this zero value is mapped to a value that lies well inside the value range of the ADC.

Dark Current

The dark current is typically dominated by thermal generation of random holes and electrons in the photon sensitive layer of the CCD line. Space radiation and other charge carriers are among the other sources (Bardoux et al., 2012; Cherniak et al., 2016). Independent of the cause, the dark current should be the same for all pixels. In this study, the signal received from the spectrometer during 'dark' is described as follows:

$$I_{dark^*}(\lambda) = \omega_{\mathrm{ADC}} + \mathrm{NL}\big(I_{dark}(\lambda)\big) \cdot t \quad (1)$$

where w_{ADC} is the ADC offset, $I_{\mathrm{dark}}(\lambda)$ is the current that is generated by the random generation of holes and electrons, t is the integration time, and NL is the non-linearity of the detector. However, the term 'dark current' is commonly used for the actual intensities that are transmitted by the spectrometer during 'dark' measurements. This value is referred to as $I_{\mathrm{dark}*}(\lambda)$ in Equation (1).

Non-Linearity

Non-linearity describes the difference between the changes in the detector signal in comparison to the changes in the light intensity. The signal of an ideal detector would proportionally increase with an increasing light intensity. The slope between light intensity and detector counts would thus be constant. Any deviation from this behavior is called non-linearity. The error caused by non-linearity is a systematic error that can seriously diminish the quality of measurement results in some specific cases, such as high accuracy measurements or relative measurements between two or more wavelengths (Aßmann et al., 2011).

Any existing non-linearity is typically the result of the combined non-linearities of the CCD pixel, amplifier, and ADC offset (Wang et al., 2016). Since all CCD pixels of one chip are expected to have very similar properties, it can be assumed that one non-linearity correction function is valid for all pixels.

Blooming

Blooming is the effect where electrons are leaking from one CCD pixel to neighboring pixels. This charge transfer only occurs if the blooming pixel is saturated. Blooming can be prevented with the aid of an anti-blooming function of the CCD spectrometer, which, however, affects the linearity of the pixels as well as their sensitivity (Fellers and Davidson, 2019).

The Hamamatsu sensor used in this study (C10082CA, CCD line: S10420-1106-01) has an anti-blooming function.

Stray Light

Stray light, $I_{stray}(\lambda)$, is unintended light within the detector that may reduce the signal to noise ratio. The stray light may have the following sources: i) scattered light from internal CCD walls and input optics of the spectrometer, ii) scattered light from the dispersive element, usually a diffraction grating, iii) inter-reflections, and iv) light coupling (Salim et al., 2011). Salim et al. (2011) and Zong et al. (2006) suggested the use of a spectrally tunable laser or a lamp with a high spectral emission in the UV region combined with a monochromator to gain data that can then be used to correct for stray light. Both light sources can be used to generate a narrow-band monochromatic light, which is then used as a light source for a spectrometer. The stray light is determined as the intensities measured at neighboring as well as all wavelengths, after taking the spectral resolution of the slit and grating into consideration. The impact of the error depends on the intensity of the light source, the extent of absorbance, and on the specific spectrometer used. Preliminary estimates based on experiments involving spectrophotometric pH measurements in seawater as described in Aßmann et al. (Aßmann et al., 2011) indicated a stray light error of approximately −0.0004 pH units. More detailed information can be found in the studies mentioned above (Zong et al., 2006; Aßmann et al., 2011; Salim et al., 2011).

Uncertainty of the Integration Time

The linearity of the integration time compared to the value that is termed integration time by the software is a critical factor in the method proposed in this work. Inside the spectrometer, the integration time is managed by the microcontroller that uses an internal timer to close the shutter. This timing is therefore only dependent on the quality of the firmware implementation. The expected effects would be a constant offset that accounts for the processing time of the interrupt handling (in the order of $<10^{-6}$ s) and a drift in the clocking frequency of the oscillator used to drive this timer. The first cannot be distinguished from the ADC offset and is therefore part of this value. The second should only play a significant role if the spectrometer is exposed to a strong temperature drift, which can be ruled out in our study.

Wavelength Calibration

It is required to conduct a wavelength calibration when using a CCD spectrometer to determine the corresponding pixel location of each wavelength prior to use (Sun et al., 2017). We used a high-end desktop spectrometer (Perkin Elmer Lambda 950) as a secondary standard to determine the wavelength accuracy of our CCD spectrometer. The accuracy of the wavelength calibration of the compact CCD spectrometer was better than any deviation we could determine ($<\pm 0.2$ nm).

Overall Signal Composition

In summary, the raw signal ($I_{raw}(\lambda)$ in counts) has the following function:

$$I_{raw}(\lambda) = \omega_{\mathrm{ADC}} + \mathrm{NL}\left(I_{dark}(\lambda) + I_{stray}(\lambda) + I(\lambda)\right) \cdot t \quad (2)$$

where $I(\lambda)$ is the current caused by the generation of holes and electrons by photons. It is produced by the light-sensitive area of a highly doped silicon (Si) semiconductor. If a photon hits an electron in the light-sensitive area, the electron is lifted into the conductive band and instantly drawn to the cathode by the internal electrical field, which is generated by the doped Si areas. The electrons are accumulated in a charge well and measured after amplification with the ADC. The investigation of stray light is beyond the scope of this study. In our applications, w_{ADC} is subtracted from each signal. This leads to the following equation:

$$I_{raw}(\lambda) = \mathrm{NL}\left(I_{dark}(\lambda) + I(\lambda)\right) \cdot t \quad (3)$$

4.3. Materials and Methods

4.3.1. Experimental Setup

Quantification of the measurement errors of the mini-spectrometer used in this study was performed with the following setup. A white Futurlec Star-LED (spectrum shown in **Figure 4.4**) combined with a simple, custom-made precision current source were used as a light source to produce broadband spectra; the spectral range covered 364–893 nm. A Hamamatsu C10082CA spectrometer with a Hamamatsu S10420-1106-01 CCD line were used to record the intensity counts at each pixel (**Table 4.1**). A combination of light fibers was used to reduce the light intensity of the LED to a degree where the minimal integration time of 10 ms yielded a maximum light intensity of about 1200 counts (445 nm) in comparison to a wavelength where the LED had no intensity (380 nm).

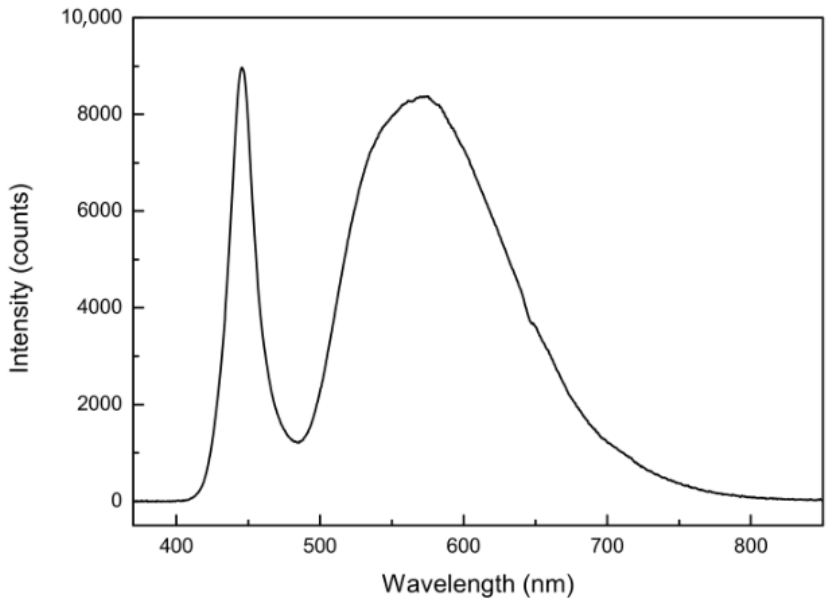

Figure 4.4: Light intensity spectrum of the white LED used in this study.

Table 4.1: Characteristics of the spectrometer used, as provided by the manufacturer (Hamamatsu Photonics K. K., 2017; Hamamatsu Photonics K.K., 2018).

Parameter	Hamamatsu C10082CA, S10420-1106-01 series
Built-in sensor	Back-thinned CCD image sensor
Spectral range	200–800 nm
Number of pixels	2048
A/D conversion	16-bits
Integration time	10 to 10,000 ms
Operating temperature	+5 to +40 °C
Cooling	Non-cooled CCD
Blooming	Anti-blooming function applied

The LED with its current source, the optical fiber, and the spectrometer were mounted in a modified 48 L cool box (Mobicool W48). The lid of the cool box was removed and replaced with a homemade device with more cooling power and space for cables (**Figure 4.5**). Care was taken to isolate the experiment inside the box from ambient light. The experiment was conducted at different temperatures (20 °C, 25 °C, and 30 °C ± 0.1 °C).

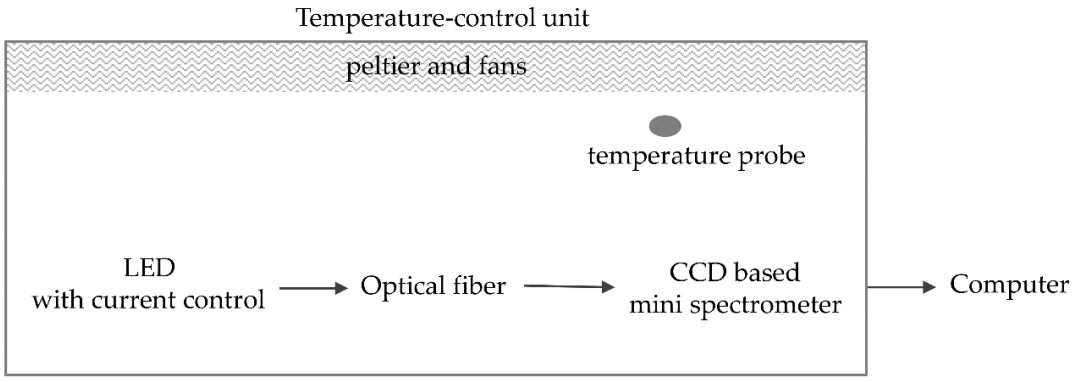

Figure 4.5: Experimental setup with instrumentation in the cool box for the quantification of the non-linearity of the miniature spectrometer.

All the measurements were controlled using routines written in the Python programming language, version 3.7.1, (Python Software Foundation. Python Language Reference, version 3.7.1 Available at http://www.python.org) on a Linux operating system using custom-made device drivers. The specific device drivers ensured that the data from the spectrometer was not modified by the manufacturer's device driver. All data analysis was undertaken using the R (2018) language for statistical computing (R-Core-Team, 2018).

4.3.2. Independent Linearity Test

To assess the non-linearity of the spectrometer a simple experiment can be performed. The results of this experiment are independent of the integration time. It is assumed that an increase in the integration time leads to a proportional increase in the signal at each pixel. A model for this behavior of uncorrected intensities I_i obtained at different integration times (t_i) is described in Equation (4), which leads via rearrangement (Equation (5)) to the ratio f (Equation (6)):

$$\frac{I_1(\lambda)}{t_1} = \frac{I_2(\lambda)}{t_2} \tag{4}$$

$$\frac{I_1(\lambda)}{I_2(\lambda)} = \frac{t_1}{t_2} \tag{5}$$

$$f = \frac{I_1(\lambda)}{I_2(\lambda)} \tag{6}$$

Figure 4.6 shows *f* ratios plotted against wavelength. The *f* ratios are calculated from spectra taken from the same light source (see **Figure 4.4**) with different integration times. Since the only difference between each single spectrum is the change in the integration time, the intensities should scale accordingly, resulting in a constant value of *f* for all pixels.

The quality of the result of the determination of *f* strongly depends on the accuracy of the determination of the ADC offset. Any deviation in that value may result in inconclusive results as Equations (4)–(6) rely on a linear relationship (through zero) between the intensities and integration times. A second approach could be to subtract the intensities of the so called 'dark pixels' (pixels that do not receive any light) from all pixels prior to their use in this linearity test. This approach was also tested and yielded comparable results, however, it should only be used for the linearity tests as the intensities of the dark pixels varied with intensity, which led to a reduced accuracy during the linearity calibration.

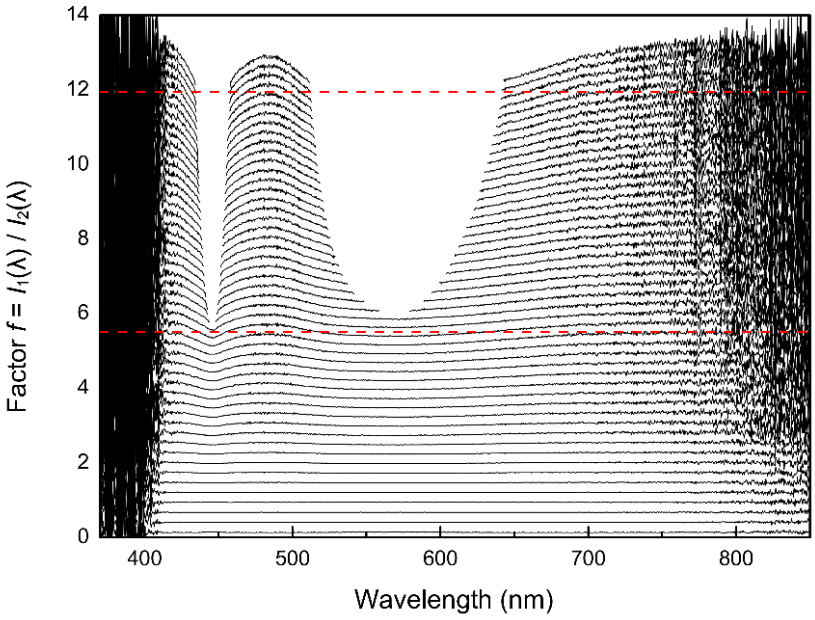

Figure 4.6: Qualitative illustration of the non-linearities of the CCD detector. The ratios *f* of $I_1(\lambda)$ to $I_i(\lambda)$ are plotted versus the wavelengths (nm) for several integration times. In theory, the f ratios should be constant for all wavelengths of a spectrum. The dashed red lines are the expected characteristics for two arbitrarily chosen integration times, the black lines are the observed characteristics for several integration times (compare also with **Figure 4.11**).

All the points above 50,000 counts were omitted due to strong increases of the non-linearity above 50,000 counts (**Figure 4.7**). Despite the qualitative nature of this way to display the data, it becomes evident that a significant non-linearity exists.

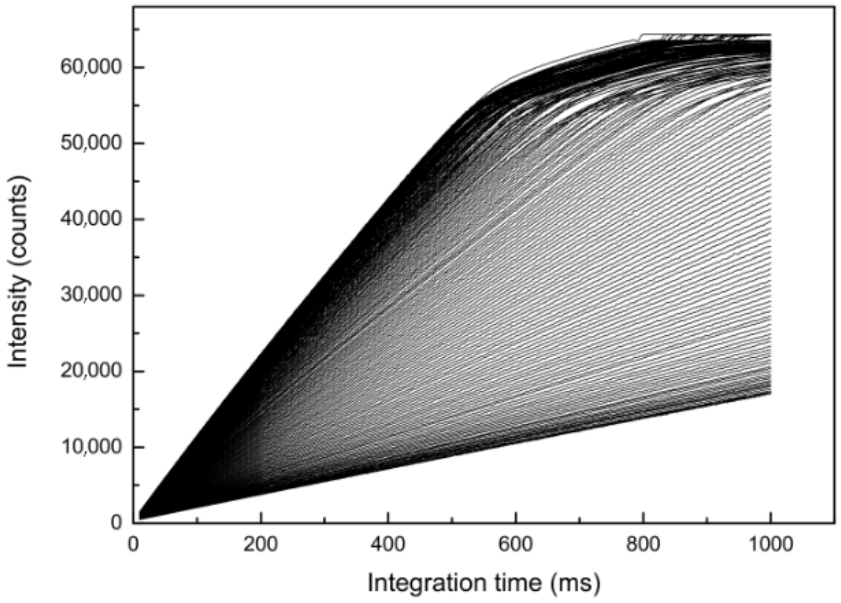

Figure 4.7: Pixel intensities (counts) versus integration time (ms). A single line represents data from one pixel. Data from 200 representative pixels (equally spaced between 400–800 nm) are shown. All data lines appear to be linear up to 50,000 counts and then deviate strongly from the ideal line.

4.4. Results and Discussion

4.4.1. ADC Offset

The ADC offset is the signal which represents the number of counts that are read at a theoretical integration time of zero (**Figure 4.3**). This value reflects the signal of the CCD line and a signal that was more or less randomly selected by the circuit designer (see **Figure 4.3**).

The ADC offset value is important for the determination of the non-linearity correction function, as the ADC offset has to be subtracted from all values prior to further operations. The subtraction of the ADC offset allows the forcing of the linear regression through zero at a zero integration time. Forcing the linear regression through zero using dark measurements is superior as it prevents inaccuracies caused by thermal noise associated with a regression using low light intensities.

The estimation of the ADC offset relies on the assumption that the non-linearity between the signal of the CCD line and ADC is not too large when only a small part of the dynamic range of the CCD is used. To obtain the ADC offset, the LED was switched off and spectra were collected at different integration times leading to intensities ranging between 350 and 1200 counts. These spectra were then used to determine the intensity (in counts) at zero integration time using a linear regression for each pixel (red dots in **Figure 4.8**). Alternatively, the ADC offset can be obtained by determining the lowest possible signal, when the LED is switched on, at wavelengths without light intensity (e.g., 380 nm, black dots in **Figure 4.8**). Both ways should theoretically yield the same result. While we found a difference of one count and a smaller drift over the whole range of pixels, this deviation lies well within the theoretical precision of the ADC (±0.5 counts) and thus can be neglected. In this study, the ADC offset amounted to 350 counts at 20 °C.

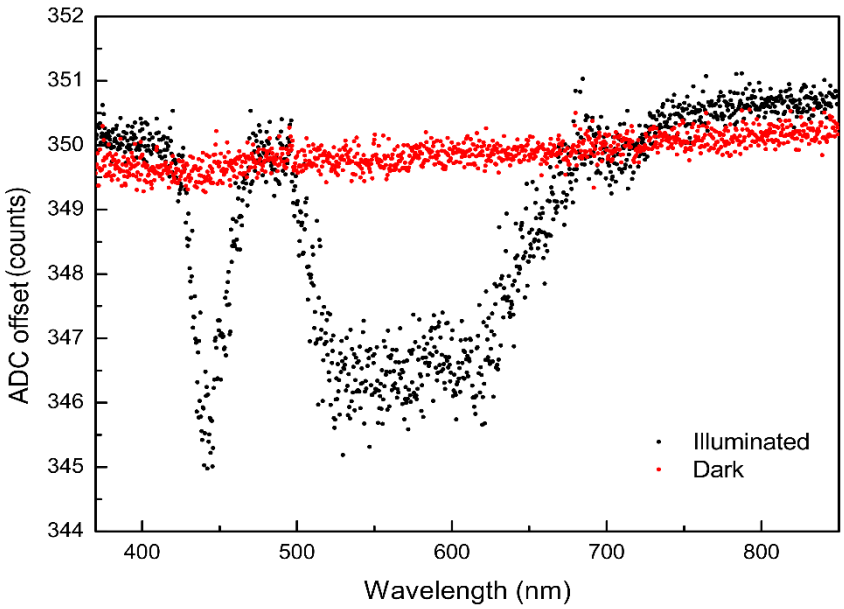

Figure 4.8: ADC offset in counts for all pixels of the CCD line. The black dots were for an enabled light source (illuminated) and the red dots were determined for a disabled light source (dark).

4.4.2. Correction of the Non-Linearity

The non-linearity correction is based on the assumption that the integration time is highly reproducible and determined by the time that was actually selected. First, the data were collected by measuring spectra at about 1800 different integration times. The variation in integration times ranged from 10 to 1000 ms, with at least 30% of the illuminated pixels being saturated at 1000 ms. Blooming was prevented by the anti-blooming function of the CCD detector. At least 25 spectra were obtained using each integration time and the pixel-specific data were averaged.

Figure 4.7 shows a selection of pixels for which intensity values were plotted against integration time. As a linear relationship between the intensity and the integration time did not exist for intensity values above 50,000 counts, this threshold was defined as an upper limit of the usable data range. Of the remaining data, the intensities of pixels obtained at the longest integration times

were averaged for the intensity range between 47,000 and 50,000 counts in order to construct a referential raw intensity (I_{raw}) versus integration time (t) curve.

A linearization was undertaken using two points, with the first point being the origin of coordinates and the second point being more or less freely chosen. A linear regression was used to determine the slope.

The resulting regression function was used to calculate a corrected intensity (I_{corr}) for each integration time, independent of wavelength. I_{corr} represents the expected result (a linear relationship between intensity and integration time) while I_{raw} represents the measured values a_0 to a_8, which represent values of regression coefficients; both datasets (one pair of I_{corr} and I_{raw} for all integration times) can be used to find a suitable correction function. The models tested for the correction functions were simple polynomial functions up to the ninth degree:

$$I_{\mathrm{corr}} = a_0.I_{\mathrm{raw}} + a_1.I_{\mathrm{raw}}^2 + a_2.I_{\mathrm{raw}}^3 + \cdots + a_8.I_{\mathrm{raw}}^9 \qquad (7)$$

The linear model function ('lm') in the R programming language (R-Core-Team, 2018) was used to fit the data to the model. The differences between the corrected data and the theoretical optimum are given in **Figure 4.9**.

It is evident that with an increasing degree of the polynomial function, the estimation error decreases. However, degrees above nine did not yield significantly better results, and even the difference between the third and the ninth degrees was quite small (**Figure 4.9**).

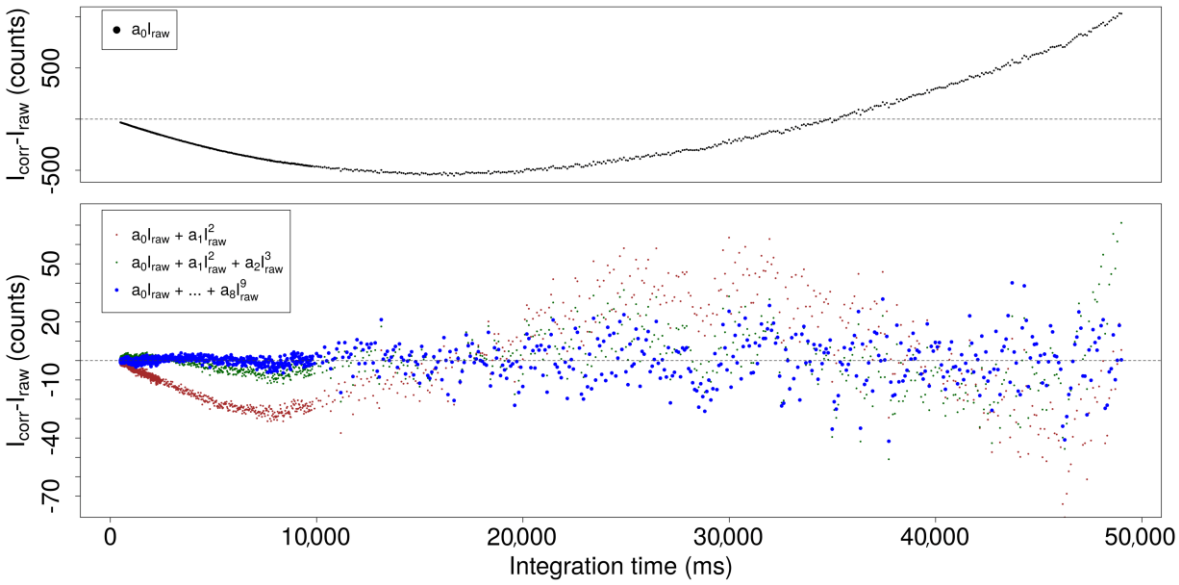

Figure 4.9: Differences between corrected and referential intensities for selected polynomials (I_{corr} - I_{raw}; Y-axis) versus integration time (ms). The panel above shows a wider range of intensity counts for the first-degree polynomial function, while the panel below shows a narrower range for the second-,

third-, and ninth-degree functions.

The optimum is a horizontal line, as the ratio $I_1(\lambda)$ / $I_2(\lambda)$ should be constant for all pixels of each spectrum since only the integration time is changed (**Figure 4.6**). Differences between corrected (I_{corr}) and theoretical optimum (I_{raw}) intensities showed a systematic deviation, for example, the absorbance error at an intensity of 50,000 counts amounts to 0.04 absorbance units (**Figure 4.10**). After the correction, the deviation of the corrected intensities from the ideal linear line amounts to a maximum of 40 counts at higher intensities. These 40 counts are well below the noise of the detector (200 counts), and do not show a systematic pattern (**Figure 4.9**).

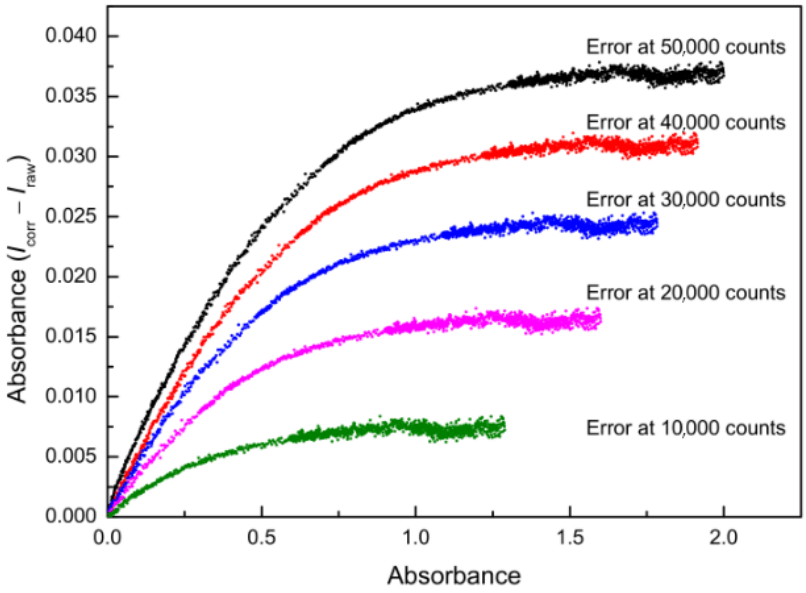

Figure 4.10: Differences between corrected and referential raw intensities in terms of absorbance error values (Y-axis) at different absorbance levels (X-axis).

4.4.3. Uncertainty in the Integration Time

The correction function was applied to raw data collected during the experiment mentioned in section 4.4.2. The results in **Figure 4.11** show a significant improvement compared to the data prior to the non-linearity correction (see **Figure 4.6**).

The overall improvement compared to the initial state also shows that the initial assumptions about the linearity of the integration time were correct. Any deviation in the reproducibility and scalability of the integration time would produce artifacts in **Figure 4.11**, as data of different integration times and intensity ranges are compared with each other in this plot.

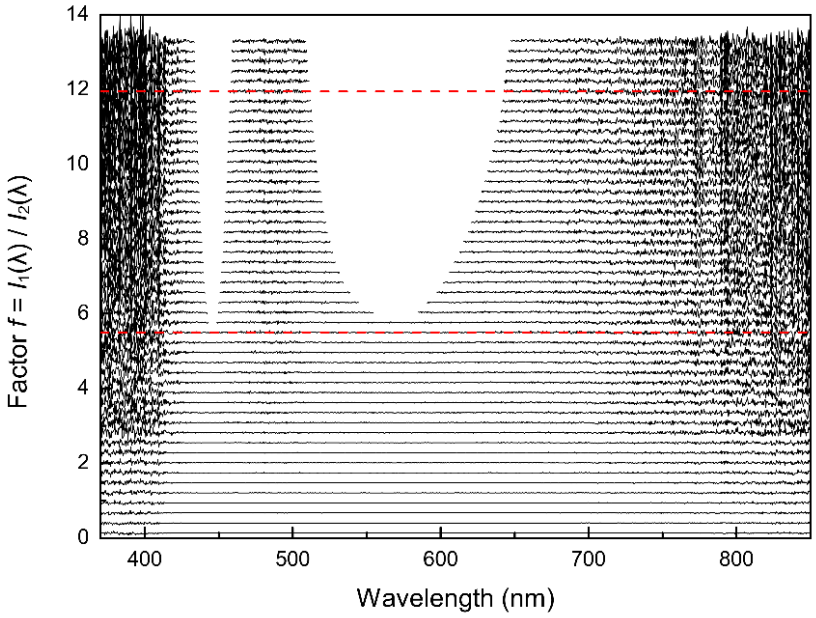

Figure 4.11: Illustration of the linear dependence of the corrected intensities on the integration time. The ratios f of $I_1(\lambda)$ to $I_i(\lambda)$ are plotted versus the wavelengths (nm) for several integration times. The correction is valid for different intensities at different integration times and wavelengths and thus verifies the applicability of the correction function. The dashed red lines are expected characteristics for two arbitrarily chosen integration times, the black lines are the corrected observed characteristics for several integration times (compare also with **Figure 4.6**).

4.4.4. Detector Noise

Figure 4.12 shows example data of the relative standard deviation of repeated intensity measurements (N = 10) as a function of intensity. On a relative basis, the error at intensities of around 500 counts is about 30 counts higher (more than 1%) than for intensities of around 20,000 counts, where the error of the intensity lies at around 200 counts (less than 0.25%).

Therefore, the noise-free resolution, which refers to the number of stable ADC bits at a constant input signal, is around 2^{11} counts at low intensities and 2^8 at medium intensities. While the resolution can be improved by averaging the signal, it would be necessary to average 2^5 spectra at low intensities and 2^8 spectra at medium intensities to obtain a true 16-bit resolution.

The full dataset (not shown here) indicates that this behavior is independent of the integration time and only depends on the intensity.

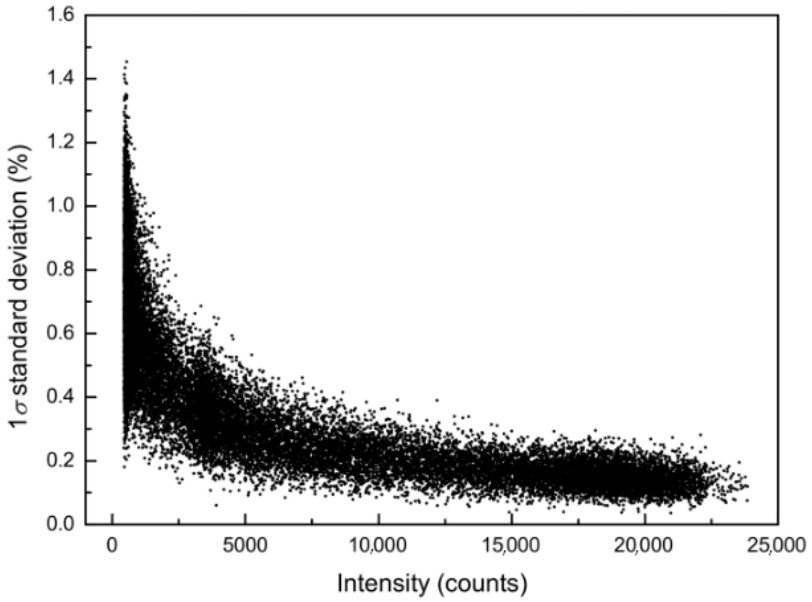

Figure 4.12: Relative detector noise as a function of intensity (counts) of the CCD detector given as 1 σ standard deviation (%).

4.4.5. Using Curve Fitting to Reduce the Noise of the Detector

The detector noise can also be reduced by using standard curve fitting procedures (e.g., R's loess function or polynomials). This curve fitting uses the neighboring pixels (usually 10 pixels or more) of the wavelength of interest to reduce the noise of the target pixel. This procedure also allows for the calculation of wavelengths between two contiguous pixels. However, this method can only be applied under certain conditions (no spikes in the spectrum of the lamp) and only gains a two- or three-fold noise reduction.

4.4.6. Temperature Dependency

The spectrometer used in this study (Hamamatsu C10082CA) has a small temperature dependency (in this study in the range of 2 counts per °C), but the resulting offset is usually constant as it is independent of the integration time and wavelength. With our spectrometer, the temperature affected the ADC offset, which changed from 350 counts at 20 °C to 338 counts at 25 °C and to 326 counts at 30 °C. The non-linearity correction function remained constant.

4.4.7. Methodological Summary

The method to compensate for the non-linearity effects of CCD spectrometers can be performed using a very simple setup in a temperature-controlled environment. Minimum requirements are a stable temperature (±1 °C) and a stable light source (e.g., a white LED with a highly stable constant current source). Furthermore, the integration times programmed into the spectrometer should be linear and stable with time (see section 4.2.2).

The following dataset has to be acquired: Light (LED on) and dark (LED off) spectra at a wide range of integration times; these depend on the capabilities of the spectrometer. In this case, we used 1800 integration times between 10 ms (lowest) and 1000 ms and took at least 25 spectra at each integration time for averaging. One of the integration times was selected and repeated at regular intervals during the measurement to ensure the stability of the system.

Suggested procedure according to **Figure 4.3**:

- Determination of the ADC offset: calculate a linear regression of the dark spectra vs. integration time and calculate the dark current (in counts) at an integration time of zero. The result is the ADC offset (see Equation (1)) for the used spectrometer.

- Plot the intensity of a range of pixels versus the integration time to determine the level at which the signal response of the spectrometer becomes obviously non-linear (see **Figure 4.7**) and exclude all data above that threshold (e.g., 50,000 counts in the case of the Hamamatsu C10082CA) during all consecutive steps.

- Select a number of the pixels at high integration times where the intensities are close to the threshold and average these pixels to form the reference graph ($I_{raw}(t)$). Subtract w_{ADC} from all intensities of this intensity data curve and perform a linear regression (forced through zero). Calculate a corrected intensity (I_{corr}) for all integration times of the reference graph.

- There is now a value-pair of I_{raw} and I_{corr} for all integration times that can be used to formulate a relationship. In the R programming language, Equation (7) ($I_{\mathrm{corr}} = a_0 \cdot I_{\mathrm{raw}} + a_1 \cdot I_{\mathrm{raw}}^2 + a_2 \cdot I_{\mathrm{raw}}^3 + \cdots + a_8 \cdot I_{\mathrm{raw}}^9$) would look like: "lm(yNew ~ 0 + y + I(y^2) + I(y^3) + I(y^4) + I(y^5) + I(y^6) + I(y^7) + I(y^8) + I(y^9))" with y = I_{raw} and yNew = I_{corr} (see section 4.4.2).

- Use this function to calculate a linear corrected intensity (I_{corr}) for each raw intensity (I_{raw}) independent of the integration time.

The method described here can be applied to all CCD-based spectrometers that fulfill the requirements described above. The experimental setup as well as the mathematics behind the method are simple. While the data acquisition and processing requires some time and processing power, the resulting correction function computes efficiently. Restrictions apply to applications where the spectrometer is subject to changing temperatures, which can be resolved using a temperature-correction function for the ADC offset.

To the best of our knowledge, only Ocean Optics provides a non-linearity compensation algorithm for its CCD units. The non-linearity correction feature of this software is based on the polynomial regression between the amount of light the detector receives and integration time. When comparing our approach

with that provided by the proprietary OOINLCorrect Software (OceanOptics), there are similarities concerning the key approach of using a change in integration time and subsequent data linearization. However, our approach is universally applicable to all CCD units, openly accessible, and has the following additional differences:

- We determined the ADC offset first, which seems to be a key way of achieving better accuracy at low light conditions. This is done by forcing the linear regression through zero at zero integration time, using dark measurements, which is superior as it prevents inaccuracies caused by thermal noise.

- We excluded data where we knew that the response of the instrument was highly nonlinear (>50,000 counts) (see **Figure 4.7**). While this may not be an issue with the Ocean Optics spectrometers, this certainly is an issue for the CCD-based Hamamatsu units. It is possible to use the full range of minimum and maximum counts of the spectrometer. However, it should be considered during data analysis that the error behavior is different for different ranges of counts.

- We provided criteria as to which pixels to select for averaging to give a better performance for the correction (see section 4.4.2.). These criteria are not provided by the OOINLCorrect Software (OceanOptics) description.

- We used absorption units instead of percentage for the evaluation of the changes in the results (see **Figure 4.10**). The example data show the benefits of our approach.

4.5. Conclusion

As the use of compact charge-coupled device (CCD) spectrometers becomes more widespread and the applications become more demanding, the non-linearity correction method presented in this study will play an important role in improving the signal-to-noise ratio of these detectors. We described a simple experimental approach, without the need for special sophisticated components, for compensating for the error related to non-linearity. The data to derive the non-linearity correction function was collected by varying the integration time at a stable light emission. According to the experimental data, a one-degree change in temperature of the spectrometer resulted in a change in the ADC offset of about 2.4 counts. Therefore, the experiment was conducted at a constant temperature. Following statistical analysis, an intensity correction function was obtained that only depends on the intensity of the signal and is independent of integration time and wavelength. The whole method can optionally be performed without removing the spectrometer from an existing experimental setup.

We proposed a simple non-linearity correction method for CCD spectrometers to improve the signal-to-noise ratio of the readings. The error due to the non-linearity of a Hamamatsu C10082CA CCD spectrometer can be reduced from a systematic error of several hundred counts to a statistical error of about 40 counts at higher intensities with the correction function applied in this study and thus can increase the accuracy of the measurements significantly. This increase in accuracy is especially useful for applications that use extinction coefficients from the literature or rely on the absorption ratio of two or more components in a mixture. In those cases, a change in the intensity of the light source or a change in the integration time may yield different results.

Author Contributions

Carsten Frank and Steffen Aßmann developed the concept of this study. **Münevver Nehir**, Carsten Frank, Steffen Aßmann and Eric P. Achterberg contributed to the implementation of the research, to the analysis of the results, and the preparation of the manuscript.

Funding

This study was supported by funding to Eric P. Achterberg from the European Union's Horizon 2020 Research and Innovation Program under the AtlantOS program, grant agreement No. 633211. Eric P. Achterberg also acknowledges funding for the OCEANSensor project by the German Federal Ministry of Economic Affairs and Energy (BMWi; Funding Agreement 03SX459A) and co-funding by the European Union 2020 Research and Innovation Program, as part of the MarTERA Program.

5. Conclusions and Future Perspectives

5.1. General Conclusions

The here presented Ph.D. thesis covers multiple commercial sensors for autonomous, high-resolution and in situ measurements of various chemical parameters in marine waters. It was motivated by the necessity of improving the data quality of autonomous submersible optical sensors and broadening their utility. To achieve this, sensor deployments in various aquatic environments were conducted. Furthermore, the data obtained via sensors based on the same analytical principle was compared with each other, and with benchtop laboratory devices to assess the accuracy of the measurements.

Undersampling, complicated sample storage and handling, and contamination and changes of samples are common issues with traditional discrete water collection and subsequent laboratory analysis methods. Autonomous sensors on the other hand provide cost and labor efficient, in situ, real-time and high-resolution data, which are required to capture dynamic changes in the marine water column. The aspect of cost efficiency is particularly significant, since the costs of newer sensor models are many times lower than of traditional approaches (Wang et al., 2019).

To date, the ocean observation community utilized a range of commercial sensors for various biogeochemical and physical parameters. Although the implementation of various sensors differs, the challenges often remain similar, i.e., limited usability due to technical or operational limitations.

This thesis is attempting to address those challenges and to expand the utility of chemical sensors, evaluate their performance in dynamic aquatic environments and assess the output data quality, in order to promote more efficient sensor usage in the ocean observer and regulatory communities. A common methodological denominator of the autonomous devices covered in this thesis is that they are all based on spectrophotometry. Spectrophotometric methods rely on correlating the concentration of a chemical parameter with the intensity of light passing through the water medium using Beer-Lambert's Law.

The findings of this thesis have been split into three chapters; Chapter 2, 3, and 4.

In Chapter 2, the performance of a LOC pH sensor (ClearWater Sensors, Southampton, UK) was evaluated in highly dynamic estuarine and coastal waters. To achieve this, field deployments of the sensor were carried out in 2018 between August 1 to August 13 (summer) and October 20 to November 19 (autumn), in Kiel Fjord, southwestern Baltic Sea. Regarding both deployments in summer and autumn, the LOC sensor autonomously performed 978 measurements in six weeks, during which time we were only able to collect 65 discrete water samples.

The presented work encompassed diurnal variations of pH obtained from the LOC sensor and discretely sampled waters, in addition ancillary hydrographic and chemical parameters. In situ pH values obtained from the LOC sensor along with the ancillary data were used to understand the carbonate chemistry system of the dynamic fjord waters. The correlation analysis showed reasonable relationships (p-value>0.5 by a majority) between pH, carbon dioxide, oxygen, temperature, salinity and nutrients. The pH_T values obtained in situ using the LOC sensor were in good agreement with those from discrete samples determined via benchtop spectrophotometric analyzer, CONTROS HydroFIA pH analyzer (4H-Jena engineering GmbH) ($y=0.998x+0.004$, $R^2=0.99$, $n=65$).

Given that the sensor has already been used in ocean environments (Rérolle et al., 2018; Yin et al., 2021), the novelty of this study was the utilization in coastal and estuarine systems. Despite the potential challenges of operating a sensor in dynamic estuarine and coastal waters (such as blockage of the sensor's in-line filter due to high loads of suspended particulate matter), the results were promising for expanding the utility of the sensors to natural waters of S<20. During the deployment periods, sudden (<24 h) changes in water characteristics were evidenced by in situ temperature and salinity data obtained from co-located sensors. The LOC sensor had an advantage over the HydroFIA benchtop analyzer for resolving the pH dynamics in fine-scale and real-time.

Besides the aforementioned advantages of autonomous sensors, the LOC sensor offers the specific advantages of being highly portable, robust, stable, calibration-free, and with no drift over several weeks.

In Chapter 3, a series of laboratory and field deployments of the TriOS OPUS UV sensor were conducted to improve the nitrate data output quality and increase its comparability with current approaches in the literature based on a similar analytical principle (i.e., SUNA sensor, Sakamoto et al., 2009). Nitrate is a routinely measured parameter in various environmental studies and its unique importance in oceanography is related to the fact that it is the principal nutrient used for photosynthesis and primary production, therefore providing information on the health status of marine environments. Conventionally, nitrate is analyzed using laboratory benchtop analyzers based on wet-chemical methods, which requires discrete sample collection, preservation, transportation, and storage of samples, besides chemical reagents, Griess assay with a copperized cadmium column, and frequent calibrations. In contrast to that, optical UV nitrate sensors are particularly beneficial of being chemical reagent and waste free, and having fast sampling intervals, in the order of seconds. However, it was identified that matrix interferences in seawater, due to bromide and CDOM, are the main disadvantage that limits their performance (Sakamoto et al., 2009; Zielinski et al., 2011; Frank et al., 2014).

Significant advancements in the intercomparability of seawater nitrate measurements can be provided if a standardized computational strategy is established. To date, several data processing algorithms have provided successful compensation of matrix interferences and computation of nitrate concentrations from raw spectral data, through a temperature correction and salinity subtraction mathematical equation, particularly tested on the ISUS and SUNA sensors (Johnson et al., 2018).

We have identified some differences between the nitrate data output when those algorithms were directly adapted on the OPUS sensor. For example, results obtained from the sensor during the vertical profiling deployments in the tropical Atlantic Ocean, down to 4,000 m, presented a deviation of ca. 6 µM in nitrate concentration compared to the discrete water analysis. This was attributed to different optical settings of sensors, i.e., the light sources; the OPUS sensor utilizes a xenon and the SUNA sensor has a deuterium lamp. Each lamp has a unique intensity at a particular wavelength and lifetime expectancy. The expected lifetime of a xenon lamp is more than 10 years at 20°C with a 1-min sampling interval, whereas this is about 2 years for a deuterium lamp.

To take the optical differences among sensors into account, a new algorithm was proposed for the OPUS, which resulted in reducing the bias in nitrate from 6 to ca. 2 µM. The new algorithm is based on the derivation of molar extinction coefficient values of bromide and nitrate at each wavelength of the sensor and at known temperature, termed as calibration coefficients. The laboratory intercomparison of five OPUS devices resulted in no significant difference among the sensors. Alongside the data processing algorithm optimization and sensor intercomparison, the sampling interval of the OPUS in a continuous mode has been reduced from a firmware setting of 30 seconds to 3 seconds by the custom-built controller, translating to a vertical resolution of 2-3 m, improving the sensor's use in vertical profiling deployments.

Results from the field deployments of the OPUS indicated that the sensor determined nitrate values were in excellent agreement with discrete samples

analyzed in the laboratory. A linear regression yielded i) y=0.99x+0.65 (R^2=0.99, n=24) for the deployment in coastal surface waters of the southeastern North Sea on April 16-17, 2019 onboard the *RV Littorina*, and ii) y=0.95x+0.26 (R^2=0.99, n=13) for the deployment in deep waters of the Atlantic Ocean on 15 October 2019 onboard the *RV Meteor*.

In summary, high-resolution sampling, long lifetime, therefore low cost, and high accuracy through the application of the newly proposed algorithm make the OPUS UV nitrate sensor a promising tool for future studies.

Chapter 4 covers the outcomes of performance improvement strategies for a compact charge-coupled device (CCD) spectrometer to reduce the potential error in measurements, particularly the non-linearity error, and obtain noise compensated signal readings, which is required for more demanding applications. CCDs have a wide range of uses from space to ocean to imaging applications and are integrated into various wet chemical analyzers and submersible autonomous sensors.

In contrast to the traditional benchtop spectrophotometers, compact CCDs are beneficial due to their small size, lightweight, high-speed data assimilation, hence low cost. Nevertheless, they are subject to a range of internal error sources related to ADC offset, dark current, non-linearity, blooming, stray light, the uncertainty of the integration time, and wavelength calibration, which are also present in monochromator-based benchtop devices.

In theory, the signal of an ideal detector increases proportionally with increasing light intensity, so there is a constant slope between them. Yet, in reality, a deviation from this linear behaviour occurs, which is referred to as non-linearity. Errors associated with dark currents, temperature changes, and bloom errors were readily corrected. Most devices, however, were lacking a compensation for detector non-linearity, which can distort the signal by up to 5% for some measurements.

Here, we aimed to assess and overcome issues related to the non-linearity error in compact CCD devices. For this, we conducted a series of laboratory experiments using the Hamamatsu C10082CA, S10420-1106-01 series miniature CCD spectrometers by setting up a simple temperature-controlled environment and obtained the light (LED on) and dark (LED off) spectra over a wide range of approximately 1800 different integration times at constant light emission and stable temperature. After looking at the acquired data and resulting statistical analysis, we proposed a mathematical equation that is universally applicable and openly accessible for simply correcting the non-linearity error on compact CCDs.

The application of this correction function reduced the dimensions of the error significantly, due to the non-linearity of a Hamamatsu C10082CA CCD spectrometer, from several hundred counts to 40 counts at higher intensities. The increase in measurement accuracy or improvement in the signal-to-noise ratio of a CCD is particularly beneficial for applications like spectrophotometric pH measurements that use absorbance ratio at two wavelengths ($R=A_{578}/A_{434}$). Thus, this study plays a significant role in extending the reliability and utility of these detectors.

5.2. Future Perspectives

The contribution of this thesis can be seen in a broader frame of Ocean Best Practices, (oceanbestpractices.org), which is moving the scientific and regulatory communities towards a more data driven and standardized approach of ocean observation. Further steps in that regard are crucial, since the vastness of the oceans challenges researchers around the globe through its complexity. As mentioned throughout this thesis, autonomous chemical sensors play a vital role in furthering our understanding of those complexities. Specifically, the data collected by those sensors accumulates in the ocean observer community.

While conducting the contributing research of this thesis, it became obvious that access to high quality and standardized data from other researchers played an important role in evaluating the own findings. As extensively discussed in Chapter 1, a range of online data platforms provide a way forward in that regard. Accessibility to this data though, remains a challenge and should be further improved to make comparisons easier to conduct and broader in scope. While autonomous sensor technologies considered as the future of marine sciences, its users should be aware of the requirements and challenges of handling big data. There is a need to develop solutions to key challenges as discussed by Guidi et al. (2020) in data acquisition, handling, management and accessibility, interoperability and computing infrastructures, by taking advantage of advances in digitalization. Future works should focus on training sensor users, networks and collaborations to expand the scope of concepts, methods and tools being developed today.

To gather high-resolution, in situ, time series pH data in dynamic coastal and estuarine environments, the LOC sensor was deployed in the Kiel Fjord. As mentioned above, such data is very scarce to date, which highlights the need for undertaking longer deployments of this sort and their comparison. Only with a better coverage of still undersampled water systems like these, a better understanding of coastal acidification and other mechanisms can be achieved.

A common and often impactful issue for submersible chemical sensors like the LOC is biofouling, which was experienced during our study as well, as the inline filter of the LOC sensor was prone to an accumulation of resuspended particulate matter after storm events (Chapter 2). Biofouling is detailed in the literature and defined as "the single biggest factor affecting the operation, maintenance and data quality" of the deployed autonomous sensors (Delgado et al., 2021). If no pre-deployment anti-fouling measures are taken, frequent manual cleaning of the sensor is necessary. For many researchers it is not clear at which specific point a cleaning is required though. This is due to lacking guidelines and different time frames of biofouling, depending on the specific conditions of the deployment site. For the LOC, the layout of the sensor chip should be re-designed (Yin, 2017), to facilitate the addition and flushing of an anti-biofouling reagent through the chip and inline filter. A directly implementable approach to curb the impact of biofouling could be the establishment of guidelines for frequent manual cleaning, which could link essential water parameters yielding biomass production like nutrients to a timeframe (including the sampling site specifications and weather, season conditions) and establish a best practice cleaning frequency for the LOC pH sensor.

Given the current state of UV optical nitrate sensor technology, platforms like FerryBox systems, profiling floats and deep-sea gliders that are suitable to perform and extend the laboratory and field intercomparison exercises with multiple sensor units are yet to be utilised to their full capability, as well as prescribed procedures to conduct such exercises and handle data in a coherent way.

It would be a great advantage and convenience for its users to add the new algorithm introduced in this study to the OPUS sensor software to calculate nitrate directly after in situ spectral measurements. The spectral nitrate measurements are prone to seasalt interference, which is a factor of in situ temperature, salinity, and pressure conditions.

Although the OPUS sensor has an internal temperature probe, we realized that it is about 5 to 6 °C higher than the in situ water temperature, attributed to the heating of the internal components. The co-located deployment of a CTD sensor is therefore essential to undertake accurate nitrate measurements using the OPUS sensor. As mentioned in Chapter 3, users of the OPUS sensor should be aware of the time drift issue of up to 60 seconds per day and regularly synchronize it to match its time of the CTD sensor. To permanently overcome this issue, we have introduced a custom-made controller, which also is advantageous to reduce the sampling frequency of the OPUS from 30 seconds to 3 seconds in continuous mode. Future works should focus on reducing the sampling rate to 1 second, which is especially required for vertical CTD profiling applications. Like for the LOC sensor, inconsistent voltages threaten continuous data gathering for the OPUS sensor. The associated risk of data loss could be reduced by our custom-made controller as well, since it provides backup power in the order of a few seconds until the sensor completes its measurements. Therefore it could prove useful to integrate the functions of the controller in the sensor itself, which could improve applicability for the ocean observer community.

Another aspect is that further investigations of the effect of CDOM on spectral nitrate measurements would provide the necessary information on whether the algorithms are straightforwardly applicable particularly in CDOM-rich waters. It should be mentioned that long term deployments in CDOM-rich waters remain especially challenging due to the effects of biofouling. Unlike for various other autonomous sensors, biofouling on the OPUS sensor has not been studied specifically. Like with the LOC sensor, biofouling likely impacts data quality on the OPUS as well. Biofouling was observed during our deployment exercises in near shore waters, requiring several manual cleanings of the optical path. To address this problem, a more repellent surface material structure or coating could slow biofouling in general and therefore reduce its impact on data quality (Delgado et al., 2021).

As an alternative to that, the measurement settings of the OPUS sensor could be adjusted to conduct consecutive measurements with a longer spectrophotometric exposure time, when deployed in optically dense waters. Furthermore, if the OPUS sensor has a built-in function to adjust this in its operating system, like the SUNA V2 (Satlantic, 2013), it could be used more efficiently in such challenging environments where the sensors performance is compromised due to less light transmission.

Overall, to date, the OPUS is mainly deployed in groundwater systems characterised by high nitrate concentrations. We showed that its applicability can be extended to marine research if the previously mentioned issues are addressed. Further field deployments and studies would be beneficial to evaluate its performance in a range of different water environments and autonomous marine platforms.

The potentials of the non-linearity error compensation introduced during this thesis do show potentials to improve the accuracy of compact spectrometer measurements. Further stray light related error mitigation remains to be undertaken. Frank et al. (2014) reported that wavelength-dependent stray light might have a significant effect at lower UV wavelengths, where bromide interference predominates in nitrate measurements. Future work regarding the suppression of stray light could lead to reducing noise in measurements, thus improving signal and accuracy levels for UV nitrate sensors.

As aforementioned, the goal of this work is not only to enhance the applicability of autonomous sensors in ocean research in general. Broader sensor usage resulting from the improved applicability and a better understanding of the efficacy of autonomous sensors in ocean research could in itself increase cost efficiency.

Lowering the costs is crucial, since it allows the research community in general to utilize saved financial assets for investing into a broader deployment of sensors, which addresses the previously mentioned issue of widespread undersampling of global water systems. As Wang et al. (2019) describes, the needed large scale sensor deployment is relying on cost-reduction of the sensors itself.

Sensor developers should react to the surging demand of the ocean observer community in high quality autonomous sensors, providing it with more affordable and improved sensor models. Additional breakthroughs in the evolution of electronics and material research could be supportive in that regard.

6. References

Arnold and Mabel Beckman Foundation Spectrophotometer. Available at: https://www.beckman-foundation.org/about-foundation/inventions/spectrophotometer/.

Aßmann, S., Frank, C., and Körtzinger, A. (2011). Spectrophotometric high-precision seawater pH determination for use in underway measuring systems. *Ocean Sci.* 7, 597–607. doi:10.5194/os-7-597-2011.

Atamanchuk, D., Tengberg, A., Thomas, P. J., Hovdenes, J., Apostolidis, A., and Hall, P. O. J. (2014). Performance of a lifetime-based optode for measuring partial pressure of carbon dioxide in natural waters. *Limnol. Oceanogr. Methods* 12, 63–73. doi:10.4319/lom.2014.12.63.

Bagshaw, E. A., Wadham, J. L., Tranter, M., Beaton, A. D., Hawkings, J. R., Lamarche-Gagnon, G., et al. (2021). Measuring pH in low ionic strength glacial meltwaters using ion selective field effect transistor (ISFET) technology. *Limnol. Oceanogr. Methods* 19, 222–233. doi:10.1002/lom3.10416.

Bardoux, A., Penquer, A., Gilard, O., Ecoffet, R., and Auvergne, M. (2012). International Conference on Space Optics; Radiation effects on image sensors. in *Proceedings of SPIE* doi:10.1117/12.2309026.

Bauer, J. E., Cai, W. J., Raymond, P. A., Bianchi, T. S., Hopkinson, C. S., and Regnier, P. A. G. (2013). The changing carbon cycle of the coastal ocean. *Nature* 504, 61–70. doi:10.1038/nature12857.

Beaton, A. D., Cardwell, C. L., Thomas, R. S., Sieben, V. J., Legiret, F. E., Waugh, E. M., et al. (2012). Lab-on-chip measurement of nitrate and nitrite for in situ analysis of natural waters. *Environ. Sci. Technol.* 46, 9548–9556. doi:10.1021/es300419u.

Beaton, A. D., Sieben, V. J., Floquet, C. F. A. A., Waugh, E. M., Abi, S., Bey, K., et al. (2011). An automated microfluidic colourimetric sensor applied in situ to determine nitrite concentration. *Sensors Actuators, B Chem.* 156, 1009–1014. doi:10.1016/j.snb.2011.02.042.

Beaton, A. D., Wadham, J. L., Hawkings, J., Bagshaw, E. A., Lamarche-Gagnon, G., Mowlem, M. C., et al. (2017). High-Resolution in Situ Measurement of Nitrate in Runoff from the Greenland Ice Sheet. *Environ. Sci. Technol.* 51, 12518–12527. doi:10.1021/acs.est.7b03121.

Becker, S., Aoyama, M., Woodward, E. M. S., Bakker, K., Coverly, S., Mahaffey, C., et al. (2019). GO-SHIP repeat hydrography nutrient manual: the precise and accurate determination of dissolved inorganic nutrients in seawater, using continuous flow analysis methods. doi:10.25607/OBP-555.

Bellerby, R. G. J., Olsen, A., Johannessen, T., and Croot, P. (2002). A high precision spectrophotometric method for on-line shipboard seawater pH measurements: the automated marine pH sensor (AMpS). *Talanta* 56, 61–69. doi:10.1016/S0039-9140(01)00541-0.

Beusekom, J. E. E. Van (2018). "Eutrophication," in *In M. Salomon, T. Markus, eds., Handbook on Marine Environment Protection, Springer*, 429–445. Available at: https://doi.org/10.1007/978-3-319-60156-4_22.

Bittig, H. C., Körtzinger, A., Neill, C., van Ooijen, E., Plant, J. N., Hahn, J., et al. (2018). Oxygen optode sensors: Principle, characterization, calibration, and application in the ocean. *Front. Mar. Sci.* 4. doi:10.3389/fmars.2017.00429.

Bittig, H. C., Maurer, T. L., Plant, J. N., Schmechtig, C., Wong, A. P. S., Claustre, H., et al. (2019). A BGC-Argo Guide: Planning , Deployment , Data Handling and Usage. *Front. Mar. Sci.* 6. doi:10.3389/fmars.2019.00502.

Blaisdell, J., Thalmann, H. L., Klajbor, W., Zhang, Y., Miller, J. A., Laurel, B. J., et al. (2021). A Dynamic Stress-Scape Framework to Evaluate Potential Effects of Multiple Environmental Stressors on Gulf of Alaska Juvenile Pacific Cod. *Front. Mar. Sci.* 8. doi:10.3389/fmars.2021.656088.

Braga, J., Balampanis, F., Pedro Aguiar, A., Sousa, J., Maza, I., and Ollero, A. (2017). Coordinated Efficient Buoys Data Collection in Large Complex Coastal Environments using UAVs. *Proc. Ocean. 2017 - Anchorage, Anchorage*, 1–9.

Bresnahan, P. J., Martz, T. R., Takeshita, Y., Johnson, K. S., and LaShomb, M. (2014). Best practices for autonomous measurement of seawater pH with the Honeywell Durafet. *Methods Oceanogr.* 9, 44–60. doi:10.1016/j.mio.2014.08.003.

Bresnahan, P. J., Takeshita, Y., Wirth, T., Martz, T. R., Cyronak, T., Albright, R., et al. (2021). Autonomous in situ calibration of ion-sensitive field effect transistor pH sensors. *Limnol. Oceanogr. Methods* 19, 132–144. doi:10.1002/lom3.10410.

Brown, N. (1991). The history of salinometers and CTD sensor systems. *Oceanus* 34, 61–66.

Burster Präzisionsmesstechnik GmbH Precision Thermometer KELVIMAT Model 4323.

Bushinsky, S. M., Takeshita, Y., and Williams, N. L. (2019). Observing Changes in Ocean Carbonate Chemistry: Our Autonomous Future. *Curr. Clim. Chang. Reports* 5, 207–220. doi:10.1007/s40641-019-00129-8.

Byrne, R. H. (2014). Measuring Ocean Acidification: New Technology for a New Era of Ocean Chemistry. *Environ. Sci. Technol.* 48, 5352–5360. doi:10.1021/es405819p.

Byrne, R. H., and Breland, J. A. (1989). High precision muitiwavelength pH determinations in seawater using cresol red. *Deep. Res. Res.* 36, 803–810.

C. Wyville-Thomson, and J. Murray (1885). *The Voyage of H.M.S. Challenger 1873-1876. Narrative Vol. I. First Part. Chapter III. In H.M.S. Challenger*. Johnson Reprint Corporation Available at: https://archimer.ifremer.fr/doc/00000/4751/.

Caldeira, K., and Wickett, M. (2005). Ocean model predictions of chemistry changes from carbon dioxide emissions to the atmosphere and ocean. *J. Geophys. Res. C Ocean.* 110. doi:10.1029/2004JC002671.

Caldeira, K., and Wickett, M. E. (2003). Anthropogenic carbon and ocean pH. *Nature* 425, 365.

Canet-Ferrer, J., Garcia-Calzada, R., Martínez-Pastor, J. P., and Muñoz-Matutano, G. (2019). Stroboscopic Space Tag for Optical Time Resolved measurements with Charge Coupled Device detector. *ACS Photonics*, 181–188. doi:10.1021/acsphotonics.8b01376.

Carstensen, J., Chierici, M., Gustafsson, B. G., and Gustafsson, E. (2018). Long-Term and Seasonal Trends in Estuarine and Coastal Carbonate Systems. *Global Biogeochem. Cycles* 32, 497–513. doi:10.1002/2017GB005781.

Castelao, R., Glenn, S., and Schofield, O. (2010). Temperature, salinity, and density variability in the central Middle Atlantic Bight. *J. Geophys. Res. Ocean.* 115, 1–14. doi:10.1029/2009JC006082.

CCD, PDA Detector Definitions *HORIBA Sci.* Available at: http://www.horiba.com/us/en/scientific/products/oem-mini-ccd-spectrometers/ccds-photodiode-arrays/ccd-pda-detector-definitions/ [Accessed January 11, 2019].

Chai, F., Johnson, K. S., Claustre, H., Xing, X., Wang, Y., Boss, E., et al. (2020). Monitoring ocean biogeochemistry with autonomous platforms. *Nat. Rev. Earth Environ.* 1, 315–326. doi:10.1038/s43017-020-0053-y.

Chegini, F., Holtermann, P., Kerimoglu, O., Becker, M., Kreus, M., Klingbeil, K., et al. (2020). Processes of Stratification and Destratification During An Extreme River Discharge Event in the German Bight ROFI. *J. Geophys. Res. Ocean.* 125. doi:10.1029/2019JC015987.

Cherniak, M. E., Ulanova, A. V., and Nikiforov, A. Y. (2016). Analysis of the effect of the interline CCD-sensor dark signal increasing during gamma-irradiation. in *Journal of Physics: Conference Series* doi:10.1088/1742-6596/737/1/012043.

Clarke, J. S., Achterberg, E. P., Rérolle, V. M. C., Abi Kaed Bey, S., Floquet, C. F. A., and Mowlem, M. C. (2015). Characterisation and deployment of an immobilised pH sensor spot towards surface ocean pH measurements. *Anal. Chim. Acta* 897, 69–80. doi:10.1016/j.aca.2015.09.026.

Claustre, H., and Johnson, K. S. (2019). 8th BGC-Argo Meeting Report.

Clayton, T. D., and Byrne, R. H. (1993). Spectrophotometric seawater pH measurements: total hydrogen ion concentration scale calibration of m-cresol purple and at-sea results. *Deep. Res.* 40, 2115–2129. doi:10.1016/0967-0637(93)90048-8.

Cullison Gray, S. E., DeGrandpre, M. D., Moore, T. S., Martz, T. R., Friederich, G. E., and Johnson, K. S. (2011). Applications of in situ pH measurements for inorganic carbon calculations. *Mar. Chem.* 125, 82–90. doi:10.1016/j.marchem.2011.02.005.

Daniel, A., Laës-Huon, A., Barus, C., Beaton, A. D., Blandfort, D., Guigues, N., et al. (2020). Toward a Harmonization for Using in situ Nutrient Sensors in the Marine Environment. *Front. Mar. Sci.* 6, 1–22. doi:10.3389/fmars.2019.00773.

Darlington, R. C. (2017). A miniaturized spectrophotometric in situ pH sensor for seawater. Available at: https://scholarworks.umt.edu/etd/11028/.

Davenport, J. J., Hodgkinson, J., Saffell, J. R., and Tatam, R. P. (2015). Noise analysis for CCD-based ultraviolet and visible spectrophotometry. *Appl. Opt.* 54, 8135–8144. doi:10.1364/AO.54.008135.

DeGrandpre, M. D., Hammar, T. R., Smith, S. P., and Sayles, F. L. (1995). In situ measurements of seawater pCO2. *Limnol. Oceanogr.* 40, 969–975.

DeGrandpre, M. D., Spaulding, R. S., Newton, J. O., Jaqueth, E. J., Hamblock, S. E., Umansky, A. A., et al. (2014). Considerations for the measurement of spectrophotometric pH for ocean acidification and other studies. *Limnol. Oceanogr. Methods* 12, 830–839. doi:10.4319/lom.2014.12.830.

Delgado, A., Briciu-Burghina, C., and Regan, F. (2021). Antifouling Strategies for Sensors Used in Water Monitoring: Review and Future Perspectives. *Sensors* 21, 1–25. doi:10.3390/s21020389.

Deumlich, D., and Gericke, A. (2020). Frequency Trend Analysis of Heavy Rainfall Days for Germany. *Water* 12, 1–29. doi:10.3390/w12071950.

Dickson, A. G. (1993). The measurement of sea water pH. *Mar. Chem.* 44, 131–142.

Dickson, A. G., Sabine, C. L., and Christian, J. R. (2007). *Guide to Best Practices for Ocean CO2 Measurements*. Available at: http://aquacomm.fcla.edu/1443/.

Doney, S. C., Busch, D. S., Cooley, S. R., and Kroeker, K. J. (2020). The Impacts of Ocean Acidification on Marine Ecosystems and Reliant Human Communities. *Annu. Rev. Environ. Resour.* 45, 83–112. doi:10.1146/annurev-environ-012320-083019.

Doney, S. C., Fabry, V. J., Feely, R. A., and Kleypas, J. A. (2009). Ocean Acidification: The Other CO2 Problem. *Ann. Rev. Mar. Sci.* 1, 169–192.

doi:10.1146/annurev.marine.010908.163834.

Doney, S. C., Ruckelshaus, M., Emmett Duffy, J., Barry, J. P., Chan, F., English, C. A., et al. (2012). Climate Change Impacts on Marine Ecosystems. *Ann. Rev. Mar. Sci.* 4, 11–37. doi:10.1146/annurev-marine-041911-111611.

Dore, J. E., Lukas, R., Sadler, D. W., Church, M. J., and Karl, D. M. (2009). Physical and biogeochemical modulation of ocean acidification in the central North Pacific. *Proc. Natl. Acad. Sci. U.S.A.* 106, 12235–12240. doi:10.1073/pnas.0906044106.

Douglas, N. K., and Byrne, R. H. (2017). Spectrophotometric pH measurements from river to sea: Calibration of mCP for $0 \leq S \leq 40$ and $278.15 \leq T \leq 308.15$ K. *Mar. Chem.* 197, 64–69. doi:10.1016/j.marchem.2017.10.001.

EOVs Available at: http://www.goosocean.org/eov [Accessed February 4, 2020].

Ey, S., Sm, K., Boersma, M., and Kh, W. (2017). Variations of Annual Turnover Cycles for Nutrients in the North Sea, German Bight Nutrients Turnover Cycles in The North Sea. *Oceanogr. Fish. Open access J.* 2. doi:10.19080/OFOAJ.2017.02.555600.

Fassbender, A., Orr, J., and Dickson, A. (2021). Technical note: Interpreting pH changes. *Biogeosciences* 18, 1407–1415. doi:10.5194/bg-18-1407-2021.

Feely, R. A., Alin, S. R., Newton, J., Sabine, C. L., Warner, M., Devol, A., et al. (2010). The combined effects of ocean acidification, mixing, and respiration on pH and carbonate saturation in an urbanized estuary. *Estuar. Coast. Shelf Sci.* 88, 442–449. doi:10.1016/j.ecss.2010.05.004.

Feely, R. A., Doney, S. C., and Cooley, S. R. (2009). Ocean acidification: Present conditions and future changes in a high-CO2 world. *Oceanography* 22, 36–47. doi:10.5670/oceanog.2009.95.

Fellers, T. J., and Davidson, M. W. (2019). Concepts in Digital Imaging Technology: CCD Saturation and Blooming. Available at: https://micro.magnet.fsu.edu/primer/digitalimaging/concepts/ccdsatandblooming.html [Accessed January 11, 2019].

Fietzek, P., Fiedler, B., Steinhoff, T., and Körtzinger, A. (2014). In situ quality assessment of a novel underwater pCO2 sensor based on membrane equilibration and NDIR spectrometry. *J. Atmos. Ocean. Technol.* 31, 181–196. doi:10.1175/JTECH-D-13-00083.1.

Finch, M. S., Hydes, D. J., Clayson, C. H., Weigl, B., Dakin, J., and Gwilliam, P. (1998). A low power ultra violet spectrophotometer for measurement of nitrate in seawater: Introduction, calibration and initial sea trials. *Anal. Chim. Acta* 377, 167–177. doi:10.1016/S0003-2670(98)00616-3.

Floquet, C. F. A., Sieben, V. J., Milani, A., Joly, E. P., Ogilvie, I. R. G., Morgan, H., et al. (2011). Nanomolar detection with high sensitivity microfluidic absorption cells manufactured in tinted PMMA for chemical analysis. *Talanta* 84, 235–239. doi:10.1016/j.talanta.2010.12.026.

Fox, L., Stukins, S., Hill, T., and Miller, C. G. (2020). Quantifying the Effect of Anthropogenic Climate Change on Calcifying Plankton. *Sci. Rep.* 10, 1–9. doi:10.1038/s41598-020-58501-w.

Frank, C., Meier, D., Voß, D., and Zielinski, O. (2014). Computation of nitrate concentrations in coastal waters using an in situ ultraviolet spectrophotometer: Behavior of different computation methods in a case study a steep salinity gradient in the southern North Sea. *Methods Oceanogr.* 9, 34–43. doi:10.1016/j.mio.2014.09.002.

Friedlingstein, P., O'Sullivan, M., Jones, M. W., Andrew, R. M., Hauck, J., Olsen, A., et al. (2020). Global Carbon Budget 2020. *Earth Syst. Sci. Data* 12, 3269–3340. doi:10.5194/essd-12-3269-2020.

Garg, S., Jiang, C., and Waite, T. D. (2018). Impact of pH on Iron Redox Transformations in Simulated Freshwaters Containing Natural Organic Matter. *Environ. Sci. Technol.* 52, 13184–13194. doi:10.1021/acs.est.8b03855.

Gazeau, F., Borges, A. V., Barrón, C., Duarte, C. M., Iversen, N., Middelburg, J. J., et al. (2005). Net ecosystem metabolism in a micro-tidal estuary (Randers Fjord, Denmark): Evaluation of methods. *Mar. Ecol. Prog. Ser.* 301, 23–41. doi:10.3354/meps301023.

Geißler, F., Achterberg, E. P., Beaton, A. D., Hopwood, M. J., Esposito, M., Mowlem, M. C., et al. (2021). Lab-on-chip analyser for the in situ determination of dissolved manganese in seawater. *Sci. Rep.* 11, 1–13. doi:10.1038/s41598-021-81779-3.

Gentemann, C. L., Scott, J. P., Mazzini, P. L. F., Pianca, C., Akella, S., Minnett, P. J., et al. (2020). Saildrone: Adaptively sampling the marine environment. *Bull. Am. Meteorol. Soc.*, E744–E762. doi:10.1175/BAMS-D-19-0015.1.

Germer;, T. A., Zwinkels;, J. C., and Tsai, B. K. (2014). *Spectrophotometry: Accurate Measurement of Optical Properties of Materials*. Amsterdam: Elsevier Science.

Gonski, S. F., Cai, W., Ullman, W. J., Joesoef, A., Christopher, R., Pettay, D. T., et al. (2018). Assessment of the suitability of Durafet-based sensors for pH measurement in dynamic estuarine environments. *Estuar. Coast. Shelf Sci.* 200, 152–168. doi:10.1016/j.ecss.2017.10.020.

Gordon, H. R., Clark, D. K., Mueller, J. L., and Hovis, W. A. (1980). Phytoplankton pigments from the Nimbus-7 Coastal Zone Color Scanner: comparisons with surface measurements. *Science (80-.).* 210, 63–66.

Grand, M. M., Clinton-Bailey, G. S., Beaton, A. D., Schaap, A. M., Johengen, T. H., Tamburri, M. N., et al. (2017). A Lab-On-Chip Phosphate Analyzer for Long-term In Situ Monitoring at Fixed Observatories: Optimization and Performance Evaluation in Estuarine and Oligotrophic Coastal Waters. *Front. Mar. Sci.* 4. doi:10.3389/fmars.2017.00255.

Grasshoff, K. M., Erhardt, K. M., and Kremling, K. (1983). Methods of Seawater Analysis. *Verlag Chemie, Weinheim*.

Gregg, W. W., and Casey, N. W. (2007). Sampling biases in MODIS and SeaWiFS ocean chlorophyll data. *Remote Sens. Environ.* 111, 25–35. doi:10.1016/j.rse.2007.03.008.

Gruber, N. (2008). "The Marine Nitrogen Cycle: Overview and Challenges," in *Nitrogen in the Marine Environment* (Elsevier Inc.), 1–50. doi:10.1016/B978-0-12-372522-6.00001-3.

Guenther, E. A., Johnson, K. S., and Coale, K. H. (2001). Direct Ultraviolet Spectrophotometric Determination of Total Sulfide and Iodide in Natural Waters. *Anal. Chem.* 73, 3481–3487. doi:10.1021/ac0013812.

Guidi, L., Fernandez Guerra, A., Canchaya, C., Curry, E., Foglini, F., Irisson, J.-O., et al. (2020). Big Data in Marine Science. , eds. B. Alexander, J. J. Heymans, A. Muñiz Piniella, P. Kellett, and J. Coopman Ostend, Belgium: Future Science Brief 6 of the European Marine Board doi:10.5281/zenodo.3755793.

Guinotte, J. M., and Fabry, V. J. (2008). Ocean acidification and its potential effects on marine ecosystems. *Ann. N. Y. Acad. Sci.* 1134, 320–342. doi:10.1196/annals.1439.013.

Gundersen, P., and Steinnes, E. (2003). Influence of pH and TOC concentration on Cu, Zn, Cd, and Al speciation in rivers. *Water Res.* 37, 307–318. doi:10.1016/S0043-1354(02)00284-1.

Hall, E. R., Wickes, L., Burnett, L. E., Scott, G. I., Hernandez, D., Yates, K. K., et al. (2020). Acidification in the U.S. Southeast: Causes, Potential Consequences and the Role of the Southeast Ocean and Coastal Acidification Network. *Front. Mar. Sci.* 7. doi:10.3389/fmars.2020.00548.

Hall, R. A., Berx, B., and Damerell, G. M. (2019). Internal tide energy flux over a ridge measured by a co-located ocean glider and moored acoustic Doppler current profiler. *Ocean Sci.* 15, 1439–1453. doi:10.5194/os-15-1439-2019.

Hamamatsu Photonics K. K. (2017). Mini Spectrometer Data Sheet, C10082CA/C10083CA Series. Available at: https://www.hamamatsu.com/eu/en/product/type/C10083CA/index.html.

Hamamatsu Photonics K.K. (2005). Xenon Flash Lamps. Available at: http://educypedia.karadimov.info/library/Xe-F_TLSX9001E05.pdf.

Hamamatsu Photonics K.K. (2018). CCD image sensors S11071/S10420-01 series.

Hammer, K., Schneider, B., Kuli, K., Kuliński, K., and Schulz-Bull, D. E. (2014). Precision and accuracy of spectrophotometric pH measurements at environmental conditions in the Baltic Sea. *Estuar. Coast. Shelf Sci.* 146, 24–32. doi:10.1016/j.ecss.2014.05.003.

Hansen, H. P. P., and Koroleff, F. (1999). *Methods of Seawater Analysis*. , ed. and M. E. K. Grasshoff, K. Kremling Weinheim, Germany, Germany: Wiley-VCH Verlag GmbH doi:10.1002/9783527613984.

Héder, M. (2017). From NASA to EU: the evolution of the TRL scale in Public Sector Innovation. *Innov. J. 22*.

Hine, R., Willcox, S., Hine, G., and Richardson, T. (2009). The Wave Glider: A Wave-Powered Autonomous Marine Vehicle. *Ocean. 2009*, 1–6. doi:10.23919/OCEANS.2009.5422129.

Hoffmann, L. J., Breitbarth, E., Boyd, P. W., and Hunter, K. A. (2012). Influence of ocean warming and acidification on trace metal biogeochemistry. *Mar. Ecol. Prog. Ser.* 470, 191–205. doi:10.3354/meps10082.

Hörstmann, C., Buttigieg, P. L., Simpson, P., Pearlman, J., and Waite, A. M. (2020). Towards a Best Practice for Developing Best Practices in Ocean Observation (BP4BP): Supporting Methodological Evolution through Actionable Documentation. IOC Manuals Guides, 84. Paris: UNESCO doi:10.25607/OBP-781.

Hörstmann, C., Buttigieg, P. L., Simpson, P., Pearlman, J., and Waite, A. M. (2021). Perspectives on Documenting Methods to Create Ocean Best Practices. *Front. Mar. Sci.* 7. doi:10.3389/fmars.2020.556234.

Hu, X., Pollack, J. B., McCutcheon, M. R., Montagna, P. A., and Ouyang, Z. (2015). Long-term alkalinity decrease and acidification of estuaries in northwestern gulf of Mexico. *Environ. Sci. Technol.* 49, 3401–3409. doi:10.1021/es505945p.

Huang, C., Xia, G., Jin, S., Hu, M., Wu, S., and Xing, J. (2018). Denoising analysis of compact CCD-based spectrometer. *Optik (Stuttg).* 157, 693–706. doi:10.1016/j.ijleo.2017.11.170.

Huang, W. J., Cai, W. J., and Hu, X. (2021). Seasonal Mixing and Biological Controls of the Carbonate System in a River-Dominated Continental Shelf Subject to Eutrophication and Hypoxia in the Northern Gulf of Mexico. *Front. Mar. Sci.* 8. doi:10.3389/fmars.2021.621243.

Hudson-Heck, E., Liu, X., and Byrne, R. H. (2021). Purification and Physical-Chemical Characterization of Bromocresol Purple for Carbon System Measurements in Freshwaters, Estuaries, and Oceans. *ACS Omega* 6, 17941–17951. doi:10.1021/acsomega.1c01579.

Ishida, H., Isono, R. S., Kita, J., and Watanabe, Y. W. (2021). Long-term ocean acidification trends in coastal waters around Japan. *Sci. Rep.* 11, 1–7. doi:10.1038/s41598-021-84657-0.

Jayne, S. R., Roemmich, D., Zilberman, N., Riser, S. C., Johnson, K. S., Johnson, G. C., et al. (2017). The Argo Program: Present and future. *Oceanography* 30, 18–28. doi:10.1109/ISAPM.1999.757315.

Jiang, L., Carter, B. R., Feely, R. A., Lauvset, S. K., and Olsen, A. (2019). Surface ocean pH and buffer capacity: past, present and future. *Sci. Rep.* 9, 1–11. doi:10.1038/s41598-019-55039-4.

Jiang, Z., Hydes, D. J., Hartman, S. E., Hartman, M. C., Campbell, J. M., Johnson, B. D., et al. (2014). Application and assessment of a membrane-based pCO2 under field and laboratory conditions sensor. *Limnol. Oceanogr. Methods* 12, 264–280. doi:10.4319/lom.2014.12.264.

Johnson, K. S. (2010). Simultaneous measurements of nitrate, oxygen, and carbon dioxide on oceanographic moorings: Observing the Redfield ratio in real time. *Limnol. Oceanogr.* 55, 615–627. doi:10.4319/lo.2009.55.2.0615.

Johnson, K. S., and Coletti, L. J. (2002). In situ ultraviolet spectrophotometry for high resolution and long-term monitoring of nitrate, bromide and bisulfide in the ocean. *Deep. Res. Part I* 49, 1291–1305. doi:10.1016/S0967-0637(02)00020-1.

Johnson, K. S., Coletti, L. J., Jannasch, H. W., Sakamoto, C. M., Swift, D. D., and Riser, S. C. (2013). Long-Term Nitrate Measurements in the Ocean Using the in situ Ultraviolet Spectrophotometer: Sensor Integration into the APEX Profiling Float. *J. Atmos. Ocean. Technol.* 30, 1854–1866. doi:10.1175/JTECH-D-12-00221.1.

Johnson, K. S., Jannasch, H. W., Coletti, L. J., Elrod, V. A., Martz, T. R., Takeshita, Y., et al. (2016a). Deep-Sea DuraFET: A Pressure Tolerant pH Sensor Designed for Global Sensor Networks. *Anal. Chem.* 88, 3249–3256. doi:10.1021/acs.analchem.5b04653.

Johnson, K. S., and Needoba, J. A. (2008). Mapping the spatial variability of plankton metabolism using nitrate and oxygen sensors on an autonomous underwater vehicle. *Limnol. Oceanogr.* 53, 2237–2250. doi:10.4319/lo.2008.53.5_part_2.2237.

Johnson, K. S., Pasqueron de Fommervault, O., Serra, R., D'Ortenzio, F., Schmechtig, C., Claustre, H., et al. (2016b). Processing Bio-Argo nitrate concentration at the DAC Level. *Argo Data Manag.*, 1–22. doi:10.1103/PhysRevB.78.035305.

Johnson, K. S., Plant, J. N., Coletti, L. J., Jannasch, H. W., Sakamoto, C. M., Riser, S. C., et al. (2017). Biogeochemical sensor performance in the SOCCOM profiling float array. *J. Geophys. Res. Ocean.* 122, 6416–6436. doi:10.1002/2017JC012838.

Jortner, J., Ottolenghi, M., and Stein, G. (1964). On the Photochemistry of Aqueous Solutions of Chloride, Bromide, and Iodide Ions. *J. Phys. Chem.* 68, 247–255.

Kristiansen, S., Farbrot, T., and Naustvoll, L.-J. (2001). Spring bloom nutrient dynamics in the Oslofjord. *Mar. Ecol. Prog. Ser.* 219, 41–49. doi:10.3354/meps219041.

Kroeker, K. J., Kordas, R. L., Crim, R., Hendriks, I. E., Ramajo, L., Singh, G. S., et al. (2013). Impacts of ocean acidification on marine organisms: Quantifying sensitivities and interaction with warming. *Glob. Chang. Biol.* 19, 1884–1896. doi:10.1111/gcb.12179.

Kwiatkowski, L., Torres, O., Bopp, L., Aumont, O., Chamberlain, M., R. Christian, J., et al. (2020). Twenty-first century ocean warming, acidification, deoxygenation, and upper-ocean nutrient and primary production decline from CMIP6 model projections. *Biogeosciences* 17, 3439–3470. doi:10.5194/bg-17-3439-2020.

Lai, C., Degrandpre, M. D., Wasser, B. D., Brandon, T. A., Clucas, D. S., Jaqueth, E. J., et al. (2016). Spectrophotometric measurement of freshwater pH with purified meta-cresol purple and phenol red. *Limnol. Oceanogr. Methods* 14, 864–873. doi:10.1002/lom3.10137.

Lai, C., Degrandpre, M. D., Wasser, B. D., Brandon, T. A., Clucas, D. S., Jaqueth, E. J., et al. (2017). Corrigendum Spectrophotometric measurement of freshwater pH with purified meta-cresol purple and phenol red. *Limnol. Oceanogr. Methods* 15, 903. doi:10.1002/lom3.10210.

Le Quéré, C., Takahashi, T., Buitenhuis, E. T., Rödenbeck, C., and Sutherland, S. C. (2010). Impact of climate change and variability on the global oceanic sink of CO2. *Global Biogeochem. Cycles* 24. doi:10.1029/2009GB003599.

Lee, K., Tong, L. T., Millero, F. J., Sabine, C. L., Dickson, A. G., Goyet, C., et al. (2006). Global relationships of total alkalinity with salinity and temperature in surface waters of the world's oceans. *Geophys. Res. Lett.* 33, 1–5. doi:10.1029/2006GL027207.

Lenton, T. M., and Watson, A. J. (2000). Redfield revisited 1. Regulation of nitrate, phosphate, and oxygen in the ocean. *Global Biogeochem. Cycles* 14, 225–248. doi:10.1029/1999GB900065.

Lewis, E., and Wallace, D. W. R. (1998). Program developed for CO2 system calculations. Oak Ridge National Laboratory ORNL/ CDIAC-105.

Li, L., Dai, C., Wu, Z., and Wang, Y. (2017). Temperature and nonlinearity correction methods for commercial CCD array spectrometers used in field. in *Proceedings of SPIE* doi:10.1088/1742-6596/972/1/012020.

Li, M., Li, R., Cai, W. J., Testa, J. M., and Shen, C. (2020). Effects of Wind-Driven Lateral Upwelling on Estuarine Carbonate Chemistry. *Front. Mar. Sci.* 7. doi:10.3389/fmars.2020.588465.

Liu, X., Patsavas, M. C., and Byrne, R. H. (2011). Purification and Characterization of meta-Cresol Purple for Spectrophotometric Seawater pH Measurements. *Environ. Sci. Technol.* 45, 4862–4868. doi:10.1021/es200665d.

Loucaides, S., Rèrolle, V. M. C., Papadimitriou, S., Kennedy, H., Mowlem, M. C., Dickson, A. G., et al. (2017). Characterization of meta-Cresol Purple for spectrophotometric pH measurements in saline and hypersaline media at sub-zero temperatures. *Sci. Rep.* 7, 1–11. doi:10.1038/s41598-017-02624-0.

Mack, J., and Bolton, J. R. (1999). Photochemistry of nitrite and nitrate in aqueous solution: a review. *J. Photochem. Photobiol. A Chem.* 128, 1–13.

Marrec, P., Cariou, T., Latimier, M., Macé, E., Morin, P., Vernet, M., et al. (2014). Spatio-temporal dynamics of biogeochemical processes and air–sea CO2 fluxes in the Western English Channel based on two years of FerryBox deployment. *J. Mar. Syst.* doi:10.1016/j.jmarsys.2014.05.010.

Martz, T., Mclaughlin, K., and Weisberg, S. B. (2015a). Best Practices for autonomous measurement of seawater pH with the Honeywell Durafet pH sensor.

Martz, T. R., Carr, J. J., French, C. R., and Degrandpre, M. D. (2003). A Submersible Autonomous Sensor for Spectrophotometric pH Measurements of Natural Waters. *Anal. Chem.* 75, 1844–1850. doi:10.1021/ac020568l.

Martz, T. R., Connery, J. G., and Johnson, K. S. (2010). Testing the Honeywell Durafet for seawater pH applications. *Limnol. Oceanogr. Methods* 8, 172–184. doi:10.4319/lom.2010.8.172.

Martz, T. R., Daly, K. L., Byrne, R. . H., Stillman, J. H., and Turk., D. (2015b). Technology for ocean acidification research: Needs and availability. *Oceanography* 28, 40–47. doi:10.5670/oceanog.2015.30.

Mclaughlin, K., Dickson, A., Weisberg, S. B., Coale, K., Elrod, V., Hunter, C., et al. (2017). An evaluation of ISFET sensors for coastal pH monitoring applications. *Reg. Stud. Mar. Sci.* 12, 11–18. doi:10.1016/j.rsma.2017.02.008.

Meyer, D., Prien, R. D., Rautmann, L., Pallentin, M., Waniek, J. J., and Schulz-Bull, D. E. (2018). In situ Determination of Nitrate and Hydrogen Sulfide in the Baltic Sea Using an Ultraviolet Spectrophotometer. *Front. Mar. Sci.* 5, 1–10. doi:10.3389/fmars.2018.00431.

Midorikawa, T., Ishii, M., Saito, S., Sasano, D., Kosugi, N., Motoi, T., et al. (2010). Decreasing pH trend estimated from 25-yr time series of carbonate parameters in the western North Pacific. *Tellus, Ser. B Chem. Phys. Meteorol.* 62, 649–659. doi:10.1111/j.1600-0889.2010.00474.x.

Miller, C. A., Pocock, K., Evans, W., and Kelley, A. L. (2018). An evaluation of the performance of Sea-Bird Scientific's SeaFET^{TM} autonomous pH sensor: considerations for the broader oceanographic community. *Ocean Sci.* 14, 751–768. doi:10.5194/os-14-751-2018.

Millero, F. J. (2007). The marine inorganic carbon cycle. *Chem. Rev.* 107, 308–341. doi:10.1021/cr0503557.

Millero, F. J., Woosley, R., Ditrolio, B., and Waters, J. (2009). Effect of ocean acidification on the speciation of metals in seawater. *Oceanography* 22, 72–85. doi:10.5670/oceanog.2009.98.

Monk, S. A., Schaap, A., Hanz, R., Borisov, S. M., Loucaides, S., Arundell, M., et al. (2021). Detecting and mapping a CO2 plume with novel autonomous pH sensors on an underwater vehicle. *Int. J. Greenh. Gas Control* 112, 1–13. doi:10.1016/j.ijggc.2021.103477.

Moore, T. S., Mullaugh, K. M., Holyoke, R. R., Madison, A. S., Yucel, M., and Luther, G. W. (2009). Marine Chemical Technology and Sensors for Marine Waters: Potentials and Limits. *Ann. Rev. Mar. Sci.* 1, 91–115. doi:10.1146/annurev.marine.010908.163817.

Morris, A. W., and Riley, J. P. (1966). The bromide/chlorinity and sulphate/chlorinity ratio in sea water. *Deep. Res.* 13, 699–705.

Mosley, L. M., Husheer, S. L. G., and Hunter, K. A. (2004). Spectrophotometric pH measurement in estuaries using thymol blue and m-cresol purple. *Mar. Chem.* 91, 175–186. doi:10.1016/j.marchem.2004.06.008.

Müller, J. D. J. D., Schneider, B., Aßmann, S., and Rehder, G. (2018). Spectrophotometric pH measurements in the presence of dissolved organic matter and hydrogen sulfide. *Limnol. Oceanogr. Methods* 16, 68–82. doi:10.1002/lom3.10227.

Müller, J. D., and Rehder, G. (2018). Metrology of pH Measurements in Brackish Waters — Part 2: Experimental Characterization of Purified meta-Cresol Purple for Spectrophotometric pHT Measurements. *Front. Mar. Sci.* 5. doi:10.3389/fmars.2018.00177.

Müller, J. D., Schneider, B., and Rehder, G. (2016). Long-term alkalinity trends in the Baltic Sea and their implications for CO2-induced acidification. *Limnol. Oceanogr.* 61, 1984–2002. doi:10.1002/lno.10349.

Nehir, M., Frank, C., Aßmann, S., and Achterberg, E. P. (2019). Improving Optical Measurements : Non-Linearity Compensation of Compact Charge-Coupled Device (CCD) Spectrometers. *Sensors* 19, 2833. doi:10.3390/s19122833.

Neves, M. S. A. C., Souto, M. R. S., Tóth, I. V., Victal, S. M. A., Drumond, M. C., and Rangel, A. O. S. S. (2008). Spectrophotometric flow system using vanadomolybdophosphate detection chemistry and a liquid waveguide capillary cell for the determination of phosphate with improved sensitivity in surface and ground water samples. *Talanta* 77, 527–532. doi:10.1016/j.talanta.2008.03.014.

Nikulina, A., Polovodova, I., and Schönfeld, J. (2008). Foraminiferal response to environmental changes in Kiel Fjord, SW Baltic Sea. *eEarth* 3, 37–49. doi:10.5194/ee-3-37-2008.

NOAA-NODC National Centers for Environmental Information, World Ocean Atlas 2018 (WOA18). Available at: https://www.nodc.noaa.gov/cgi-bin/OC5/woa18f/woa18oxnuf.pl?parameter=n [Accessed December 7, 2020].

OceanOptics Ocean Optics Inc.; OOINLCorrect Loading Non-Linearity Correction Coefficients Instructions. Available at: https://oceanoptics.com/wp-content/uploads/OOINLCorrect-Linearity-Coeff-Proc.pdf.

Oda, E., Ishihara, Y., and Teranishi, N. (1983). Blooming suppression mechanism for an interline CCD image sensor with a vertical overflow drain. *Int. Electron Devices Meet.*, 501–504. doi:10.1109/IEDM.1983.190553.

Ogura, N., and Hanya, T. (1966). Nature of Ultra-violet Absorption of Sea Water. *Nature* 212, 758. doi:10.1038/212758a0.

Okazaki, R. R., Sutton, A. J., Feely, R. A., Dickson, A. G., Alin, S. R., Sabine, C. L., et al. (2017). Evaluation of marine pH sensors under controlled and natural conditions for the Wendy Schmidt Ocean Health XPRIZE. *Limnol. Oceanogr. Methods* 15, 586–600. doi:10.1002/lom3.10189.

Olechowski, A., Eppinger, S. D., and Joglekar, N. (2015). Technology readiness levels at 40: a study of state-of-the-art use, challenges, and opportunities. *Portl. Int. Conf. Manag. Eng. Technol.* doi:10.1109/PICMET.2015.7273196.

Orr, J. C., Fabry, V. J., Aumont, O., Bopp, L., Doney, S. C., Feely, R. A., et al. (2005). Anthropogenic ocean acidification over the twenty-first century and its impact on calcifying organisms. *Nature* 437, 681–686. doi:10.1038/nature04095.

Pasqueron de Fommervault, O., D'Ortenzio, F., Mangin, A., Serra, R., Migon, C., Claustre, H., et al. (2015). Seasonal variability of nutrient concentrations in the Mediterranean Sea: Contribution of Bio-Argo floats. *J. Geophys. Res. Ocean.* 120, 8528–8550. doi:10.1002/2015JC011103.

Pearlman, J., Bushnell, M., Coppola, L., Karstensen, J., Buttigieg, P. L., Pearlman, F., et al. (2019). Evolving and Sustaining Ocean Best Practices and Standards for the Next Decade. *Front. Mar. Sci.* 6, 1–19. doi:10.3389/fmars.2019.00277.

Pellerin, B. A., Bergamaschi, B. A., Downing, B. D., Saraceno, J. F., Garrett, J. D., and Olsen, L. D. (2013). Optical techniques for the determination of nitrate in environmental waters: Guidelines for instrument selection, operation, deployment, maintenance, quality assurance, and data reporting. *U.S. Geol. Surv. Tech. Methods 1-D5*, 37.

Pellerin, B. A., Saraceno, J. F., Shanley, J. B., Sebestyen, S. D., Aiken, G. R., Wollheim, W. M., et al. (2012). Taking the pulse of snowmelt: In situ sensors reveal seasonal, event and diurnal patterns of nitrate and dissolved organic matter variability in an upland forest stream. *Biogeochemistry* 108, 183–198. doi:10.1007/s10533-011-9589-8.

Pereyra, A., Zevallos, M. I., Ricra, J., and Tello, J. C. (2016). Characterizing a CCD detector for astronomical purposes: OAUNI Project. *Rev. Tec.* 26, 20–25. doi:10.21754/tecnia-26022016.03.

Perez, I. M., Sansalvador, D. V., Fay, C. D., Cleary, J., Nightingale, A. M., Mowlem, M. C., et al. (2016). Autonomous reagent-based microfluidic pH sensor platform. *Sensors Actuators B. Chem.* 225, 369–376. doi:10.1016/j.snb.2015.11.057.

Pidcock, R., Srokosz, M., Allen, J., Hartman, M., Painter, S., Mowlem, M., et al. (2010). A novel integration of an ultraviolet nitrate sensor on board a towed vehicle for mapping open-ocean submesoscale nitrate variability. *J. Atmos. Ocean. Technol.* 27, 1410–1416. doi:10.1175/2010JTECHO780.1.

Pierrot, D., Lewis, E., and Wallace, D. W. R. (2006). MS Excel program developed for CO2 system calculations. Carbon Dioxide Information Analysis Center, Oak Ridge National Laboratory, US. doi:10.3334/CDIAC/ otg.CO2SYS XLS CD.

Possenti, L., Humphreys, M. P., Bakker, D. C. E., Cobas-García, M., Fernand, L., Lee, G. A., et al. (2021). Air-Sea Gas Fluxes and Remineralization From a Novel Combination of pH and O2 Sensors on a Glider. *Front. Mar. Sci.* 8. doi:10.3389/fmars.2021.696772.

Prien, R. (2007). Technologies for new in situ chemical sensors. *Ocean. 2007 - Eur.*, 1–6. doi:10.1109/OCEANSE.2007.4302222.

Pulli, T., Nevas, S., El Gawhary, O., van den Berg, S., Askola, J., Kärhä, P., et al. (2017). Nonlinearity characterization of array spectroradiometers for the solar UV measurements. *Appl. Opt.* 56, 3077–3086. doi:10.1364/ao.56.003077.

Python Software Foundation. Python Language Reference, version 3.7.1 Available at http://www.python.org.

R-Core-Team (2018). R: A language and environment for statistical computing. Vienna, Austria Available at: http://www.r-project.org.

Redfield, A. C. (1958). The biological control of chemical factors in the environment. *Am. Sci.* 46.

Redfield, A. C., Ketchum, B. H., and Richards, F. A. (1963). The Influence of Organisms on the Composition of the Sea Water. *Hill, M.N. Ed., Sea, New York, London, Intersci. Publ.* 2, 26–77.

Rérolle, V. M. C., Achterberg, E. P., Ribas-Ribas, M., Kitidis, V., Brown, I., Bakker, D. C. E., et al. (2018). High Resolution pH Measurements Using a Lab-on-Chip Sensor in Surface Waters of Northwest European Shelf Seas. *Sensors* 18, 1–23. doi:10.3390/s18082622.

Rérolle, V. M. C., Floquet, C. F. A., Harris, A. J. K., Mowlem, M. C., Bellerby, R. R. G. J., and Achterberg, E. P. (2013). Development of a colorimetric microfluidic pH sensor for autonomous seawater measurements. *Anal. Chim. Acta* 786, 124–131. doi:10.1016/j.aca.2013.05.008.

Rérolle, V. M. C., Floquet, C. F. A., Mowlem, M. C., Bellerby, R. R. G. J., Connelly, D. P., and Achterberg, E. P. (2012). Seawater-pH measurements for ocean-acidification observations. *Trends Anal. Chem.* 40, 146–157. doi:10.1016/j.trac.2012.07.016.

Rérolle, V., Ruiz-Pino, D., Rafizadeh, M., Loucaides, S., Papadimitriou, S., Mowlem, M., et al. (2016). Measuring pH in the Arctic Ocean: Colorimetric method or SeaFET? *Methods Oceanogr.* 17, 32–49. doi:10.1016/j.mio.2016.05.006.

Riebesell, U., Fabry, V., Hansson, L., and Gattuso, J.-P. (2010). Guide to best practices for ocean acidification research and data reporting. Brussels, Belgium.

Rieger, L., Langergraber, G., Kaelin, D., Siegrist, H., and Vanrolleghem, P. A. (2008). Long-term evaluation of a spectral sensor for nitrite and nitrate. *Water Sci. Technol.*, 1563–1569. doi:10.2166/wst.2008.146.

Robert-Baldo, G. L., Morris, M. J., and Byme, R. H. (1985). Spectrophotometric Determination of Seawater pH Using Phenol Red. *Anal. Chem.* 57, 2564–2567. doi:10.1021/ac00290a030.

Roemmich, D., Alford, M. H., Claustre, H., Johnson, K. S., King, B., Moum, J., et al. (2019). On the Future of Argo: A Global, Full-Depth, Multi-Disciplinary Array. *Front. Mar. Sci.* 6. doi:10.3389/fmars.2019.00439.

Royal Society (2005). Ocean acidification due to increasing atmospheric carbon dioxide. Available at: https://royalsociety.org/topics-policy/publications/2005/ocean-acidification/.

Sabine, C. L., Feely, R. A., Gruber, N., Key, R. M., Lee, K., Bullister, J. L., et al. (2004). The Oceanic Sink for Anthropogenic CO2. *Science (80-.).* 305, 367–371. doi:10.1126/science.1097403.

Saderne, V., Fietzek, P., and Herman, P. M. J. (2013). Extreme Variations of pCO2 and pH in a Macrophyte Meadow of the Baltic Sea in Summer: Evidence of the Effect of Photosynthesis and Local Upwelling. *PLoS One* 8, 1–8. doi:10.1371/journal.pone.0062689.

Sakamoto, C. M., Johnson, K. S., Coletti, L. J., and Jannasch, H. W. (2009). Improved algorithm for the computation of nitrate concentrations in seawater using an in situ ultraviolet spectrophotometer. *Limnol. Oceanogr. Methods* 7, 132–143. doi:10.1002/lom3.10209.

Sakamoto, C. M., Johnson, K. S., Coletti, L. J., Maurer, T. L., Massion, G., Pennington, J. T., et al. (2017). Hourly in situ nitrate on a coastal mooring: A 15-year record and insights into new production. *Oceanography* 30, 114–127. doi:https://doi.org/10.5670/oceanog.2017.428.

Salim, S. G. R., Fox, N. P., Hartree, W. S., Woolliams, E. R., Sun, T., and Grattan, K. T. V. (2011). Stray light correction for diode-array-based spectrometers using a monochromator. *Appl. Opt.* 50, 5130–5138. doi:10.1002/jlac.18651360106.

Sanders, T., Schöl, A., and Dähnke, K. (2018). Hot Spots of Nitrification in the Elbe Estuary and Their Impact on Nitrate Regeneration. *Estuaries and Coasts* 41, 128–138. doi:10.1007/s12237-017-0264-8.

Sastri, A. R., Christian, J. R., Achterberg, E. P., Atamanchuk, D., Buck, J. J. H., Bresnahan, P., et al. (2019). Perspectives on in situ Sensors for Ocean Acidification Research. *Front. Mar. Sci.* 6. doi:10.3389/fmars.2019.00653.

Satlantic (2013). Sea-Bird Coastal SUNA V2 Manual. For SUNA running firmware version 2.3 or later.

Schofield, O., Glenn, S., Orcutt, J., Arrott, M., Meisinger, M., Gangopadhyay, A., et al. (2010). Automated Sensor Networks to Advance Ocean Science. *Trans. Am. Geophys. Union* 91, 345–346. doi:10.1029/2010EO390001.

Schories, D. ., Selig, U., Schubert, H., Jegzentis, K., Mertens, M., Schubert, M., et al. (2006). Küstengewässer-Klassifizierung deutsche Ostsee nach EU-WRRL. *Tl. A Äußere Küstengewässer. Forschungsbericht*.

Sea-Bird Coastal SUNA (2015). Submersible Ultraviolet Nitrate Analyzer (SUNA) User Manual Edition 1.

Sea-Bird Electronics Inc. Sea-Bird Scientific, USA. SeaFET™ V2 and SeapHOx™ V2 User manual. *Sea-Bird Electron. Inc.* Available at: http://satlantic.com/seafet [Accessed January 11, 2021].

Seckmeyer, G., Bais, A., Bernhard, G., Blumthaler, M., Booth, C., Disterhoft, P., et al. (2001). Instruments to measure solar ultraviolet radiation: Part 1: Spectral Instruments.

Seckmeyer, G., Bais, A., Bernhard, G., Blumthaler, M., Drüke, S., Kiedron, P., et al. (2010). Instruments to measure solar ultraviolet radiation: Part 4: Array Spectroradiometers.

Seelmann, K., Steinhoff, T., Aßmann, S., and Körtzinger, A. (2020). Enhance Ocean Carbon Observations: Successful Implementation of a Novel Autonomous Total Alkalinity Analyzer on a Ship of Opportunity. *Front. Mar. Sci.* 7. doi:10.3389/fmars.2020.571301.

Seidel, M. P., Degrandpre, M. D., and Dickson, A. G. (2008). A sensor for in situ indicator-based measurements of seawater pH. *Mar. Chem.* 109, 18–28. doi:10.1016/j.marchem.2007.11.013.

Smalley, D., Poon, T. C., Gao, H., Kvavle, J., and Qaderi, K. (2018). Volumetric Displays Turning 3-D Inside-Out. *Opt. Photonics News*, 26–33.

Snazelle, T. T. (2016). The Effect of Suspended Sediment and Color on Ultraviolet Spectrophotometric Nitrate Sensors. *U.S. Geol. Surv. Open-File Rep.* doi:10.3133/ofr20161014.

Sørensen, S. P. L., and Palitzsch, S. (1910). Uber die Messung der Wasserstoffionenkonzentration des Meerwassers. *Biochem.* Z. 24. Available at: https://doi.org/10.1093/icesjms/s1.60.3.

Spaulding, R. S., Degrandpre, M. D., Beck, J. C., Hart, R. D., Peterson, B., Carlo, E. H. De, et al. (2014). Autonomous in Situ Measurements of Seawater Alkalinity. *Environ. Sci. Technol.* 48, 9573–9581.

Staudinger, C., Strobl, M., Fischer, J. P., Thar, R., Mayr, T., Aigner, D., et al. (2018). A versatile optode system for oxygen, carbon dioxide, and pH measurements in seawater with integrated battery and logger. *Limnol. Oceanogr. Methods* 16, 459–473. doi:10.1002/lom3.10260.

Stedmon, C. A., and Nelson, N. B. (2015). "The Optical Properties of DOM in the Ocean," in *Biogeochemistry of Marine Dissolved Organic Matter* (Elsevier Inc.), 481–508. doi:10.1016/B978-0-12-405940-5.00010-8.

Stokowski, M., Schneider, B., Rehder, G., and Kuliński, K. (2020). The characteristics of the CO2 system of the Oder River estuary (Baltic Sea). *J. Mar. Syst.* 211, 1–11. doi:10.1016/j.jmarsys.2020.103418.

Sun, Y. C., Huang, C., Xia, G., Jin, S. Q., and Lu, H. B. (2017). Accurate wavelength calibration method for compact CCD spectrometer. *J. Opt. Soc. Am. A* 34, 498–505. doi:10.1364/JOSAA.34.000498.

Takeshita, Y., Warren, J. K., Liu, X., Spaulding, R. S., Byrne, R. H., Carter, B. R., et al. (2021). Consistency and stability of purified meta-cresol purple for spectrophotometric pH measurements in seawater. *Mar. Chem.* 236, 1–10. doi:10.1016/j.marchem.2021.104018.

Tanhua, T., Pouliquen, S., Hausman, J., O'Brien, K. M., Bricher, P., Bruin, T. de, et al. (2019). Ocean FAIR Data Services. *Front. Mar. Sci.* 6. doi:10.3389/fmars.2019.00440.

Thomas, A., Ramkumar, A., and Shanmugam, A. (2022). CO2 acidification and its differential responses on aquatic biota-a review. *Environ. Adv.* 8, 1–6. doi:10.1016/j.envadv.2022.100219.

Thurnherr, A. M., Symonds, D., and St. Laurent, L. (2015). Processing Explorer ADCP Data Collected on Slocum Gliders using the LADCP Shear Method. *Proc. 2015 IEEE/OES Elev. Curr. Waves Turbul. Meas.*, 1–7. doi:10.1109/CWTM.2015.7098134.

Tilbrook, B., Jewett, E. B., DeGrandpre, M. D., Hernandez-Ayon, J. M., Feely, R. A., Gledhill, D. K., et al. (2019). An Enhanced Ocean Acidification Observing Network: From People to Technology to Data Synthesis and Information Exchange. *Front. Mar. Sci.* 6. doi:10.3389/fmars.2019.00337.

Tintoré, J., Casas, B., Heslop, E., Vizoso, G., Pascual, A., Orfila, A., et al. (2013). *The Impact of New Multi-platform Observing Systems in Science, Technology Development and Response to Society Needs; from Small to Large Scales...* , ed. and A. Q.-A. R. Moreno-Díaz, F. Pichler Springer, Berlin, Heidelberg. doi:10.1007/978-3-642-53862-9_44.

TriOS GmbH (2017). OPUS Operating Instructions.

Van Dam, B. R., and Wang, H. (2019). Decadal-scale acidification trends in adjacent North Carolina estuaries: Competing role of anthropogenic CO2 and riverine alkalinity loads. *Front. Mar. Sci.* 6. doi:10.3389/fmars.2019.00136.

Vazquez-Cuervo, J., Gomez-Valdes, J., Bouali, M., Miranda, L. E., Van der Stocken, T., Tang, W., et al. (2019). Using Saildrones to Validate Satellite-Derived Sea Surface Salinity and Sea Surface Temperature along the California/Baja Coast. *Remote Sens.* 11. doi:10.3390/rs11171964.

Visbeck, M. (2018). Ocean science research is key for a sustainable future. *Nat. Commun.* 9. doi:10.1038/s41467-018-03158-3.

Voss, M., Bange, H. W., Dippner, J. W., Middelburg, J. J., Montoya, J. P., Ward, B., et al. (2013). The marine nitrogen cycle: recent discoveries, uncertainties and the potential relevance of climate change. *Philos. Trans. R. Soc. B* 368. doi:10.1098/rstb.2013.0121.

Voynova, Y. G., Brix, H., Petersen, W., Weigelt-Krenz, S., and Scharfe, M. (2017). Extreme flood impact on estuarine and coastal biogeochemistry: The 2013 Elbe flood. *Biogeosciences* 14, 541–557. doi:10.5194/bg-14-541-2017.

Vuillemin, R., and Sanfilippo, L. (2010). A Compact, Low-Power In-Situ Flow Analyzer for Marine Applications. *Sea Technol.* 51, 29–32.

Wallace, R. B., Baumann, H., Grear, J. S., Aller, R. C., and Gobler, C. J. (2014). Coastal ocean acidification: The other eutrophication problem. *Estuar. Coast. Shelf Sci.* 148, 1–13. doi:10.1016/j.ecss.2014.05.027.

Wang, S., Carpenter, D. A., DeJager, A., DiBella, J. A., Doran, J. E., Fabinski, R. P., et al. (2016). A 47 million pixel high-performance interline CCD image sensor. *IEEE Trans. Electron Devices* 63, 174–181. doi:10.1109/TED.2015.2447214.

Wang, Z. A., Moustahfid, H., Mueller, A. V., Michel, A. P. M., Mowlem, M., Glazer, B. T., et al. (2019). Advancing Observation of Ocean Biogeochemistry, Biology, and Ecosystems With Cost-Effective in situ Sensing Technologies. *Front. Mar. Sci.* 6:519. doi:10.3389/fmars.2019.00519.

Whitt, C., Pearlman, J., Polagye, B., Caimi, F., Muller-Karger, F., Copping, A., et al. (2020). Future Vision for Autonomous Ocean Observations. *Front. Mar. Sci.* 7. doi:10.3389/fmars.2020.00697.

Wilkinson, M. D., Dumontier, M., Aalbersberg, Ij. J., Appleton, G., Axton, M., Baak, A., et al. (2016). Comment: The FAIR Guiding Principles for scientific data management and stewardship. *Sci. Data* 3. doi:10.1038/sdata.2016.18.

Willcox, S., Meinig, C., Sabine, C. L., Lawrence-Slavas, N., Richardson, T., Hine, R., et al. (2009). An Autonomous Mobile Platform for Underway Surface Carbon Measurements in Open-Ocean and Coastal Waters. *Proc. MTS/IEEE Ocean. 2009 Conf.* doi:10.23919/oceans.2009.5422067.

Williams, N. L., Juranek, L. W., Feely, R. A., Johnson, K. S., Sarmiento, J. L., Talley, L. D., et al. (2017). Calculating surface ocean pCO2 from biogeochemical Argo floats equipped with pH: An uncertainty analysis. *Global Biogeochem. Cycles* 31, 591–604. doi:10.1002/2016GB005541.

Wilson, T. J. B., Cooley, S. R., Tai, T. C., Cheung, W. W. L., and Tyedmers, P. H. (2020). Potential socioeconomic impacts from ocean acidification and climate change effects on Atlantic Canadian fisheries. *PLoS One* 15, 1–29. doi:10.1371/journal.pone.0226544.

Wong, A. P. S., Wijffels, S. E., Riser, S. C., Pouliquen, S., Hosoda, S., Roemmich, D., et al. (2020). Argo Data 1999–2019: Two Million Temperature-Salinity Profiles and Subsurface Velocity Observations From a Global Array of Profiling Floats. *Front. Mar. Sci.* 7. doi:10.3389/fmars.2020.00700.

Wong, C. S., Waser, N. A. D., Nojiri, Y., Whitney, F. A., Page, J. S., and Zeng, J. (2002). Seasonal cycles of nutrients and dissolved inorganic carbon at high and mid latitudes in the North Pacific Ocean during the Skaugran cruises: Determination of new production and nutrient uptake ratios. *Deep. Res. Part II Top. Stud. Oceanogr.* 49, 5317–5338. doi:10.1016/S0967-0645(02)00193-5.

Wright-Fairbanks, E. K., Miles, T. N., Cai, W. J., Chen, B., and Saba, G. K. (2020). Autonomous Observation of Seasonal Carbonate Chemistry Dynamics in the Mid-Atlantic Bight. *J. Geophys. Res. Ocean.* 125, 1–20. doi:10.1029/2020JC016505.

Xia, G., Liu, Q., Zhou, H., and Yu, F. (2015). A non-linearity correction method of charge-coupled device array spectrometer. *SPIE - Int. Soc. Opt. Eng.* 9677, 1–6. doi:10.1117/12.2197725.

Xu, Y.-Y., Chen, B., Cai, W.-J., Gao, Y., Wanninkhof, R., Salisbury, J., et al. (2017). Short-term variability of aragonite saturation state in the central Mid-Atlantic Bight. *J. Geophys. Res. Ocean.* 122, 4274–4290. doi:10.1002/2017JC012901.Received.

Yang, B., Patsavas, M. C., Byrne, R. H., and Ma, J. (2014). Seawater pH measurements in the field: A DIY photometer with 0.01 unit pH accuracy. *Mar. Chem.* 160, 75–81. doi:10.1016/j.marchem.2014.01.005.

Yin, T. (2017). A Lab-on-Chip Sensor for In Situ Spectrophotometric Measurement of Seawater pH, PhD Thesis, Ocean and Earth Sciences, University of Southampton.

Yin, T., Papadimitriou, S., Rérolle, V. M. C., Arundell, M., Cardwell, C. L., Walk, J., et al. (2021). A Novel Lab-on-Chip Spectrophotometric pH Sensor for Autonomous In Situ Seawater Measurements to 6000 m Depth on Stationary and Moving Observing Platforms. *Environ. Sci. Technol.* 55, 14968−14978. doi:10.1021/acs.est.1c03517.

Yuanqian, L., Jingmei, H., Jingguo, Y., Bo, Z., and Yuanqing, H. (2002). Multi-component analysis by flow injection-diode array detection-spectrophotometry using partial least squares calibration model for simultaneous determination of zinc, cadmium and lead. *Anal. Chim. Acta* 461, 181–188. Available at: isi:000176385500002.

Zeebe, R. E., and Wolf-Gladrow, D. A. (2001). *CO2 in seawater: equilibrium, kinetics, isotopes*. Amsterdam: Elsevier doi:10.1016/s0924-7963(02)00179-3.

Zehr, J. P., and Kudela, R. M. (2011). Nitrogen Cycle of the Open Ocean: From Genes to Ecosystems. *Ann. Rev. Mar. Sci.* 3, 197–225. doi:10.1146/annurev-marine-120709-142819.

Zhang, J. Z. (2000). The use of pH and buffer intensity to quantify the carbon cycle in the ocean. *Mar. Chem.* 70, 121–131. doi:10.1016/S0304-4203(00)00024-4.

Zhao, Y., Liu, J., Uthaipan, K., Song, X., Xu, Y., He, B., et al. (2020). Dynamics of inorganic carbon and pH in a large subtropical continental shelf system: Interaction between eutrophication, hypoxia, and ocean acidification. *Limnol. Oceanogr.* 65, 1359–1379. doi:10.1002/lno.11393.

Zielinski, O., Fiedler, B., Heuermann, R., Kortzinger, A., Kopiske, E., Meinecke, G., et al. (2007). A new nitrate continuous observation sensor for autonomous sub-surface applications: Technical design and first results. *Ocean. 2007-Europe* June, 1–4. doi:10.1109/OCEANSE.2007.4302300.

Zielinski, O., Voß, D., Saworski, B., Fiedler, B., and Körtzinger, A. (2011). Computation of nitrate concentrations in turbid coastal waters using an in situ ultraviolet spectrophotometer. *J. Sea Res.* 65, 456–460. doi:10.1016/j.seares.2011.04.002.

Zong, Y., Brown, S. W., Johnson, B. C., Lykke, K. R., and Ohno, Y. (2006). Simple spectral stray light correction method for array spectroradiometers. *Appl. Opt.* 45, 1111–1119. doi:10.1364/AO.45.001111.

7. Statement of Declaration

I, Münevver Nehir, born on 15th December 1990 in Mersin, hereby declare that I have written this Ph.D. thesis independently, under compliance of the rules for good scientific practice of the German Research Foundation. I declare that I used only the sources, the data and the support that I have clearly mentioned. Moreover, I assure that this Ph.D. thesis has not been submitted for the conferral of a degree elsewhere, neither in part or as a whole, and that none of my academic degrees has ever been withdrawn. Published or submitted for publication manuscripts are identified at the relevant places.

Münevver Nehir Kiel, April 2022